RICE UNIVERSITY

# Role of Anomalous Nanoscale Heat Transfer in Gating Magnetogenetic Proteins

by

**Sruthi Polali**

A Thesis Submitted
in Partial Fulfillment of the
Requirements for the Degree

**Doctor of Philosophy**

Approved, Thesis Committee:

Jacob T. Robinson, Chair
Assistant Professor of Electrical and
Computer Engineering and
Bioengineering

Jason Hafner
Professor of Physics and Astronomy and
Chemistry

Caleb Kemere
Assistant Professor of Electrical and
Computer Engineering and
Bioengineering

Houston, Texas

December, 2018

ABSTRACT

Role of Anomalous Nanoscale Heat Transfer in Gating Magnetogenetic Proteins

by

Sruthi Polali

Genetically encoded ion channels that respond to magnetic fields Magnetogenetics would enable wireless stimulation of specific neurons deep in the brain and thus provide a powerful tool for studying neural correlates of behavior in freely moving animals. A recently engineered magnetogenetic protein consisting of ferritin and TRPV4, dubbed *Magneto2.0*, was shown to elicit action potentials in neurons when exposed to a magnetic field. The iron-sequestering protein, ferritin serves as the magnetically sensitive domain, while TRPV4 is a cation selective channel that responds to temperature stimuli. However, the mechanism of how the protein senses magnetic field was not understood. Here, we propose a novel mechanism based on the magnetocaloric effect to explain the working of *Magneto2.0*: A magnetic field reduces the entropy of the ferritin nanoparticles when its magnetic spins align, resulting in an increase in temperature that in turn gates the heat-sensitive TRPV4 channel. This theory is supported by our calculations and experimental data showing that the observed responses are indeed thermally mediated.

In exploring this theory, I delve into aspects of nanoscale heat transfer, which deviate significantly from bulk thermal properties. Classical laws predict that there is no significant temperature gradient between a magnetically heated nanoparticle and the surrounding medium and that a single nanoparticle cannot generate enough heat

to gate a channel. We measured the temperature and thermal conductance at the vicinity of heated nanoparticles using a novel thermosensor based on silicon microring resonator. A change in temperature shifts the resonant wavelength of the resonator. Temperature near the surface of heated nanoparticles attached directly to these resonators is measured based on the wavelength shift. We show that temperature near surface of the nanoparticles is much higher than that of the surrounding medium and that the thermal conductance at the nanoparticle-water interface is 13 orders of magnitude lower than expected from classical laws. This lowered conductance would enable a single ferritin to gate a nearby TRPV4 channel. In addition to reconciling biological observations with physical properties of magnetic nanoparticles, understanding this mechanism is essential for the design of future magnetogenetic tools with improved magnetic sensitivity.

# Acknowledgments

First of all, I would like to thank my advisor, Dr. Jacob Robinson for giving me the opportunity to work on this exciting project and for all the support and mentorship he provided over the last years. I can never stop admiring his unlimited motivation, out-of-the-box thinking and extreme optimism. I also thank Dr. Jason Hafner and Dr. Caleb Kemere for their valuable comments while being part of my committee. This work was done in collaboration with Fan Ye, Dr. Guillaume Duret, Erin Anderson, Martin Bell, Constantine Tzounas and Ben Avants in the Robinson Lab. It was great working with them and my special thanks to all of them. I would also like to thank the rest of the Robinson Lab for always being ready to help me.

I thank Dr. Douglas Natelson, Dr. Cecilia Clementi, Dr. Amina Qutub, Dr. Arun Mahadevan, Dr. Mikhail Shapiro, Hunter David and Dr. Markus Meister for their technical assistance or constructive discussions related to this research. I also thank the Rice Shared Equipment Authority, University of Houston Nanofabrication Facility and University of Texas Austin Microelectronics Research Center where the devices were fabricated. This work was supported by the National Science Foundation (NeuroNex Innovation Award 1707562) and by the Welch Foundation (Award C-1963-20180324). I would also like to thank Dr. Kevin Kelly, Carol Lively from the Applied Physics program and the International Students Office at Rice for making my graduate school journey smoother.

Also thanks to my friends for being there with me through good and bad times - Raj, Jitin, Manasi, Rishika, Deb, Arko, Souptik, Aswathy, Amanda, Deepak, Santhoshi and many others. Thanks to my violin teacher, Erika Lawson for the fun lessons and encouraging a hobby that kept me going through those years.

Special thanks to my parents whose sacrifices are the reason I came this far. Finally, it wouldn't be an exaggeration if I said all this would not have been possible without the constant support of my uncle, Nagendra Polali and my husband, Sai Deep Tetali. I can never thank them enough for all the support they provided through my PhD journey.

# Contents

# Illustrations

# Chapter 1

# Introduction

This thesis proposes and builds on new mechanisms for magnetogenetic neuromodulation. Magnetogenetic tools allow us to control the activity of neurons in a non-invasive manner, a capability that helps us understand the correlation between neural activity and behavior in animals. This technique is based on genes that encode magnetic sensitivity in specific neuronal populations, which allows for rapid neuronal stimulation in freely moving untethered animals. Recent reports of magnetogenetic proteins have been viewed with a critical eye owing to a lack of understanding of the mechanism by which they sense magnetic fields. A fundamental understanding of how they work is important not only to validate the experimental results but also for the rational design of improved magnetogenetic tools.

In this chapter, I will first explain the importance of neuromodulation. Then I will talk about the various neuromodulation techniques that already exist and explain the need for magnetogenetic techniques. I will then outline recent advances in the area of magnetogenetics before introducing the new mechanisms.

## 1.1 Importance of neuromodulation

Neurons in the brain maintain a potential difference across their membranes that serves in transmitting electrical signals between different parts of the cell and between one cell and another in the body. These electrical signals, often in the form of

action potentials not only help propagate signals but also activate other intracellular processes necessary for bodily functions. For example, in muscle cells, an action potential is the first step that sets off a chain of reactions ultimately resulting in contraction. Neuronal electrical activity is what brings about changes in an animal's behavior, and hence any technique that can modulate this activity is useful for understanding how the brain works and for treating diseases resulting from neuronal damage.

### 1.1.1 Approaches for neuromodulation

**Electrical stimulation**: One of the earliest techniques developed for manipulating and studying neural activity was the voltage clamp [3]. In this method, a micropipette electrode is used to clamp the cell at a desired voltage enabling the study of voltage-current relations in the cell. Hodgkin and Huxley made extensive use of this technique in their study of the mechanisms of neuronal excitability and action potential generation, and built models that are still in wide use [4]. They received the 1963 Nobel Prize in Physiology and Medicine for this work. Neher and Sakmann refined the voltage clamp and built the patch clamp technique, for which they won the Nobel Prize in 1991. Using patch clamp electrophysiology, it is possible to record currents even of single ion channels, the pore-forming membrane proteins that are responsible for maintaining membrane potential and the passage of ions that leads to electric signals and currents [5].

While micropipettes enable low-noise, temporally precise, high-resolution electrical stimulation and recording, they cannot be easily multiplexed. In order to study networks of neurons, microelectrode arrays have been developed for both in-vitro and in-vivo studies [6]. Electrical stimulation of the brain in-vivo using microelectrodes is

now being used in clinics to treat patients with Parkinson's, depression and other neurological disorders in a treatment method called Deep Brain Stimulation (DBS) ([7]). However, microelectrode insertion is highly invasive carrying the risk of infection, tissue inflammation and damage [8].

**Transcranial Magnetic Stimulation**: Use of magnetic fields to stimulate neurons is a much safer option because magnetic fields penetrate the body and hence require no implants. They interact weakly with body tissue and are hence harmless [9]. Progress in this direction has been made by Transcranial Magnetic Stimulation (TMS). In this non-invasive technique, a coil is used to generate magnetic field pulses near the skull. These pulses induce electrical activity in the brain [10]. Although the exact mechanism of its action is still not completely understood, this method has been in use for the past 30 years to treat symptoms of depression. But this technique lacks cell-type specificity in its action.

**Optogenetics**: The advent of optogenetics has been able to successfully achieve the ability to target and manipulate the activity of a single specific cell-type while leaving all others untouched. In 2003, Nagel et al. [11] cloned the protein Chanelrhodopsin (ChR2) from the green algae Chlamydomonas reinhardtii and expressed it in mammalian cells. Channelrhodopsin (ChR2) is a light-gated ion channel and its expression renders cells optically excitable. Action potentials were successfully elicited in ChR-2 expressing neurons with high temporal precision upon excitation with blue light [12]. Halorhodopsin (NpHR) is another such optogenetic protein, which was used successfully to inhibit neuronal activity by shining yellow light on the neurons expressing that protein [13]. Therefore, by co-expressing ChR-2 and NpHR, one can preferentially excite or inhibit specific neuronal cell-types by using blue light or yellow light. Optogenetic activation and inhibition of neuronal activity has been

used since then in mice brains to study the mechanisms of various neural circuits and their correlation to behavior. While this technique has been used extensively over the past decade for neuroscience research, it falls short in one aspect: Light cannot reach deep areas of the brain due to scattering effects. Therefore, this method could be used only for stimulating neurons in the surface of the brain. Magnetic fields again can overcome this problem because animal tissue is essentially transparent to them, hence giving access to deeper regions. Moreover, optogenetic neuromodulation requires the implanting of an invasive probe in order to create a transparent light path through the animal's body, while magnetic fields pass unimpeded and harmlessly through the body.

Magnetogenetics hence provides a technique that integrates the advantages from all the above techniques. It includes the deep-brain accessibility achieved by DBS, the non-invasiveness achieved by TMS, the cell-type specificity and high temporal resolution achieved by optogenetics.

## 1.2 Magnetogenetic Neuromodulation

Magnetogenetics, similar to optogenetics, is a technique in which neuronal stimulation is achieved through genetically encoded ion channels that respond to magnetic fields. Magnetic fields can penetrate the body and hence can be used to stimulate neurons in any part of the brain. Magnetic fields also offer the ability to rapidly turn stimulation on and off in synchronization with behavior or environmental cues. Unlike optogenetics, there are no known ion channels that exist in nature that switch on or off in response to a magnetic field. A magnetically sensitive ion channel needs to be engineered. The design of a magnetogenetic protein consists of 3 aspects:

1. A known ion channel that responds to temperature or mechanical stimulus;

Examples include: Members of the Transient Receptor Potential Vanilloid (TRPV) family of proteins such as TRPV1, TRPV4; Piezo1; Potassium channel subfamily K member 2, also known as TREK-1.

2. A magnetic nanoparticle attached to the ion channel: Superparamagnetic or paramagnetic nanoparticles are best suited for the application because they are magnetized only in the presence of a field. Hence they make ideal switches responding to a magnetic field; and

3. A mechanism to couple the effect of the magnetic field on the magnetic particle towards opening the ion channel. Mainly, there are two biophysical mechanisms through which magnetic fields can be coupled to neuronal function: a. Magneto-thermal approach, in which an alternating magnetic field rapidly flips the magnetic moment of superparamagnetic nanoparticles that are present in the vicinity of thermoreceptors, causing them to heat up and gate the channels. 2. Magneto-mechanical approach in which a gradient magnetic field or dipole-dipole interaction causes a magnetic nanoparticle to force open a mechano-receptor it is attached to. Here, I will review literature on both of the above mechanisms and finally, I will propose new mechanisms for achieving magnetogenetic neuromodulation.

**Magneto-thermal approach:** In this approach, single domain magnetic nanoparticles are heated using radio frequency alternating magnetic fields, thereby increasing temperature and gating thermally-sensitive ion channels. In the presence of an alternating field, the magnetic spin in a single domain nanoparticle rapidly flips resulting in heat due to relaxation losses. Huang et al. first demonstrated this technique by attaching nanoparticles to the ion channel TRPV1 [14]. This technique was later successfully employed in vivo to stimulate neurons deep in mouse brain [15]. In this study, Chen et al. used high concentration magnetic ferrofluids injected into the

brain. More recently, heating of superparamagnetic particles tethered to neuronal membrane was successfully used to achieve deep brain stimulation [16]. Stanley et al. demonstrated ability to control the levels of insulin through calcium signaling pathways triggered by the opening of TRPV1 channels in response to RF magnetic heating of nanoparticles attached to them [17]. While this technique provides a promising approach, it requires the injection of synthetic nanoparticles. Nanoparticles only last in the injected region for a limited period of time before they get internalized. The particles are localized to the injected area, hence making it difficult to activate cells that are dispersed [18]. The use of genetically encoded magnetic nanoparticles greatly simplifies the implementation of magnetigenetics.

One of the leading candidates for a genetically encoded magnetic nanoparticle is ferritin. Ferritin is an iron-binding protein involved in iron storage and homeostasis that can be found in nearly all living organisms [19]. It is composed of 24 subunits organized to form a hollow spherical cavity that can enclose up to 4500 Fe atoms [20]. The external diameter of the ferritin cage is 12 nm and the internal cavity is about 8nm. Iron is stored within the ferritin cage in the form of hydrous ferric oxide, with structure similar to that of mineral ferrihydrite.

Stanley et al. demonstrated increased plasma insulin and decreased blood glucose levels in the mice genetically encoded with ferritin and TRPV1 after 1 hour of treatment with radio frequency alternating magnetic field [18]. Because of its small magnetic moment and the small size, the power generated by ferritin is very low. Fantechi et al. showed that the temperature rise in a solution containing ferritin nanoparticles subjected to an alternating magnetic field is insignificant and leads to near-zero increase in bulk solution temperature [19]. It has been argued that the low amount of power generated in ferritin in an RF field could not have been suffi-

cient to gate TRPV1 as shown by Stanley et al. [21]. However, possible existence of giant thermal resistances at the nanoscale and the steep temperature gradients (as discussed in Section 2.3) might enable the activation of channels in the vicinity of ferritin.

**Magneto-mechanical approach:** Generating alternating fields of sufficient magnitude and frequency for animal stimulation is challenging and cost-ineffective. Therefore, a mechanism that depends on steady or low frequency magnetic fields will also greatly simplify the implementation of magnetogenetics. One approach is to use mechanical force generated by magnetic nanoparticles in the presence of a gradient field or another dipole to gate mechanically sensitive ion channels. This was achieved using a gradient field generated by an electromagnetic needle to pull on zinc-doped iron oxide nanoparticles attached to force-sensitive channels on inner ear hair cells of a bullfrog [22]. While this approach was a good first demonstration, one cannot use electromagnetic needles to achieve strong enough gradient forces in deep regions of a brain. A technique that can use a *uniform* steady magnetic field would be more suitable for in vivo experiments. Hughes et al used magnetic particles tethered to mechanically sensitive channel TREK-1 to induce whole-cell currents. However, the currents elicited were not sufficient in magnitude to bring about a significant physiological change, such as eliciting an action potential [23]. Furthermore, a fully genetically encoded magnetically sensitive ion channel is more desirable as mentioned above. Recently, steady-field magneto-mechanical stimulation using biogenic ferritin were reported by Stanley et al. [18] and Wheeler et al [1]

Wheeler et al. genetically engineered a protein chimera consisting of TRPV4 and ferritin dubbed **Magneto2.0** (represented in Figure 1.1). When expressed in HEK cells, *Magneto2.0* produced magnetic field dependent calcium transients as de-

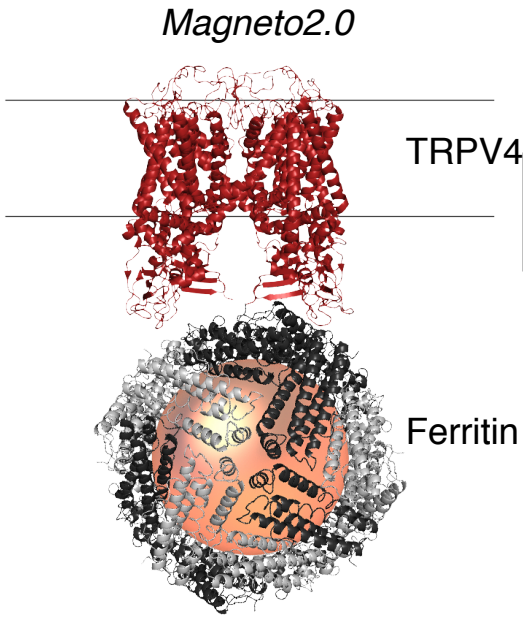


Figure 1.1 : Structure of *Magneto2.0* protein chimera consisting of the mechanical and temperature dependent ion channel TRPV4 and iron sequestering protein, ferritin

tected using calcium sensitive dye Fluo-4. Their stimulus consisted of three pulses of 40-50 mT magnetic field generated by a permanent magnet at 0.1 Hz, 90% duty cycle. Their results are shown in Figure 1.2. Their controls consisted of cells expressing unfused TRPV4 and ferritin moieties, unstimulated *Magneto2.0*-expressing cells, *Magneto2.0*-expressing cells exposed to the TRP pore blocker ruthenium red (RR), and *Magneto2.0*-expressing cells in $Ca^{2+}$-free extracellular medium.They were also able to successfully elicit action potentials in neurons upon application of 50 mT steady field. The authors suggested that the mechanism of action in this case is mechanical stimulation of TRPV4 due to dipole-dipole interactions between two ferritin molecules attached to the channel. Stanley et al. also demonstrated an increase in intracellular calcium levels in HEK cells expressing a TRPV1-ferritin complex in response to a steady magnetic field. In this case also, it was hypothesized that the

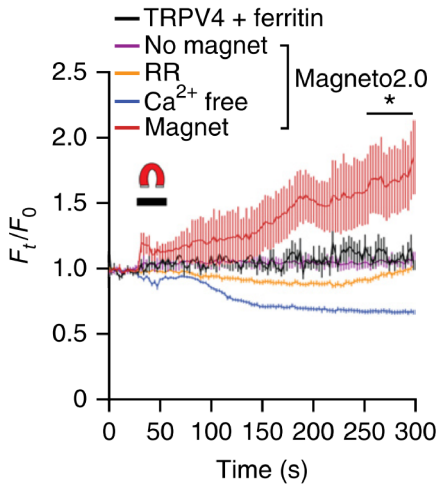


Figure 1.2 : Figure adapted from [1] shows average fluorescence under different conditions from cells expressing *Magneto2.0* or unfused TRPV+ferritin under the application of 50mT magnetic field (represented by horizontal bar with horseshoe).

mechanism of action was mechanical stimulation.

While the experimental results of the two papers are exciting and promising, concerns exist about whether the proposed mechanisms explain the results they observed. Unlike synthetic iron oxide nanoparticles, ferritin has a very low value of susceptibility. Therefore, the forces generated by ferritin are not sufficient to gate ion channels. Calculations show that the force produced by ferritin is 4 to 9 log units weaker than those required for channel gating [21]. Furthermore, RF heating of ferritin does not produce enough heat to bring about the necessary temperature change to cause opening of thermoreceptors, contrary to the observations made by Stanley et al. Understanding the actual mechanism behind the success of a magnetogenetic tool is important in order to design improved future tools and for multiplexing them.

### 1.2.1 Magnetocaloric gating mechanism for Magnetogenetic proteins

In my work, I propose an alternate mechanism for the working of the TRPV4 ferritin chimera. This explanation takes into consideration the fact that TRPV4 is not only mechanically sensitive but also temperature sensitive, thereby making it possible for the process to be thermally mediated. The approach is based on the heating of magnetic materials upon reduction of their entropy in the presence of a magnetic field. More precisely, the ordering of magnetic moments within the ferritin nanoparticle in the presence of a field reduces its magnetic entropy, thereby producing heat [24]. This heat is then taken up by the channel to change its conformation to an open state, causing an influx of current. This concept is known as the magnetocaloric effect in the magnetic refrigeration community [25]. In this thesis, I will develop a theoretical framework for the magnetocaloric mechanism. I will also describe the results of the experiments performed on HEK cells expressing the chimeric construct which show that the responses are indeed thermally mediated. I will develop a theoretical framework for a second possible mechanism to explain *Magneto2.0* which links the channel's mechanical stress dependence to its temperature dependence using a simple thermodynamic model for its gating. I will show that even though the force due to ferritin is not enough to independently pull a channel open, it is still capable of doing work on the channel, that results in a slight shift in the channel open probability and in turn leads to influx of current over time. However, experimental evidence does not support this mechanism as will be outlined in this thesis.

The magnetocaloric mechanism provides a rationale for developing newer and better magnetogenetic proteins. As a demonstration of this capability, we designed a novel magnetogenetic protein dubbed **MagM8**, consisting of fusion of the *cold* sensitive channel TRPM8 and ferritin. The magnetocaloric effect predicts that the

*demagnetization* of the ferritin nanoparticle should lead to a decrease in temperature and thus be able to gate the cold-activated ion channel, TRPM8. In this thesis, I will calculate the effect of magnetic field on gating of *MagM8* and also experimentally show that *MagM8* is indeed magnetically sensitive.

### 1.2.2 Role of anomalous nanoscale heat transfer in gating Magnetogenetic proteins

In exploring the Magnetocaloric theory, I delve into aspects of nanoscale heat transfer in the vicinity of magnetic nanoparticles, which deviate significantly from classical laws. Nanoscale heating effects are important not only for magnetigenetics but for several other applications. Synthetic iron oxide nanoparticles heated in the presence of radio frequency alternating magnetic fields due to relaxation losses are widely used for hyperthermia treatment for cancer cells, remote neural stimulation and drug release. The most common application to treat cancer cells typically uses a large volume of highly concentrated nanoparticles to target a large area of cancer cells. Several other applications require targeted local heating of nanoparticles such as for killing small tumors or single cells without affecting healthy cells in the vicinity; for cell-type specific neuronal stimulation by attaching synthetic or genetically encoded nanoparticles to temperature sensitive ion channels; for localized release of drugs. These applications require temperature change in the immediate vicinity of the nanoparticles without a global temperature change. Classical laws, however, predict that a single nanoparticle, owing to its small size, dissipates heat quickly and efficiently to the surrounding medium and therefore, its surface temperature is not expected to be significantly more than that of its surrounding [26]. A significant temperature change is expected only in a bulk concentrated solution of nanoparticles. A single nanoparticle (such as

ferritin) is not expected to generate enough heat to gate a thermo-sensitive channel. In other words, there is no local temperature change at the nanoscale.

However, a growing body of experimental evidence has emerged over the past decade that indicates that the heat transfer at the vicinity of heated magnetic nanoparticles deviates significantly from that expected from classical laws of physics. Several studies measured a significant temperature gradient at the surface of heated nanoparticles in solution [14], [27], [28], [16], [29], [30], [31]. In addition, these studies showed that nanoparticles dissipate heat at a rate several orders of magnitude slower than predicted by classical laws [14], [27], [28], [16]. In fact, several studies have used local heating in the close vicinity of the nanoparticles to trigger cellular response [32] or the release of a drug [33], even though there is no global increase in temperature in the targeted area. Studying the thermal transport properties in the vicinity of these nanoparticles is therefore important for better understanding of fundamental science as well as for providing a rationale for building better bio- and nano-technology tools.

I will discuss our novel method for probing temperature close to the surface of heated iron oxide nanoparticles using silicon photonic thermosensors. This method relies on the temperature dependent optical properties of silicon. A change in temperature changes the resonant wavelength condition of a silicon micro-resonator. Nanoparticles are attached to the resonator and the the thermal conductances and temperature changes near their surface are measured based on this optical readout. The results from this study show significant deviations from classical laws and will be discussed in detail. Using this approach, we show that temperature near the surface of nanoparticles is indeed higher than that of the surrounding medium. Most importantly, we use this method to determine the value for the thermal conductance at the nanoscale, which in turn is used to calculate the effect of ferritin heating towards

gating TRPV4. By modeling our system, we show that thermal conductance between the nanoparticles and the medium is 13 orders of magnitude lower than expected from classical laws.

# Chapter 2

# Mechanism based on Magnetocaloric Heating of Ferritin

In this chapter, I will develop the theory for magnetocaloric gating of Magneto. The magnetic spins in ferritin align in the presence of a field which induces a change in the entropy of the nanoparticle. This in turn results in a change in temperature that gates the thermoreceptor TRPV4. A schematic representation of how magnetocaloric effect in ferritin can activate the nearby TRPV4 is shown in Figure 2.1. In the following sections, I will first calculate the amount of heat produced due to magnetocaloric effect in ferritin. Then I will calculate the temperature change that results from this heat in the channel. Finally, I will use a thermodynamic model for the channel to calculate the effect of the temperature change.

## 2.1 Magnetocaloric Effect

The reversible change in temperature of a magnetic material upon the application or removal of a magnetic field is called the Magnetocaloric effect [25]. The change in temperature is a result of the change in entropy of the system due to the alignment of magnetic spins. We could think of the material as consisting of magnetic moments and the lattice. In the absence of magnetic field, the magnetic moments are randomly oriented. When a magnetic field is applied, the moments orient along the direction of the field, decreasing the magnetic contribution to the entropy. If the magnetization occurs adiabatically, then the total entropy remains constant. The decrease in

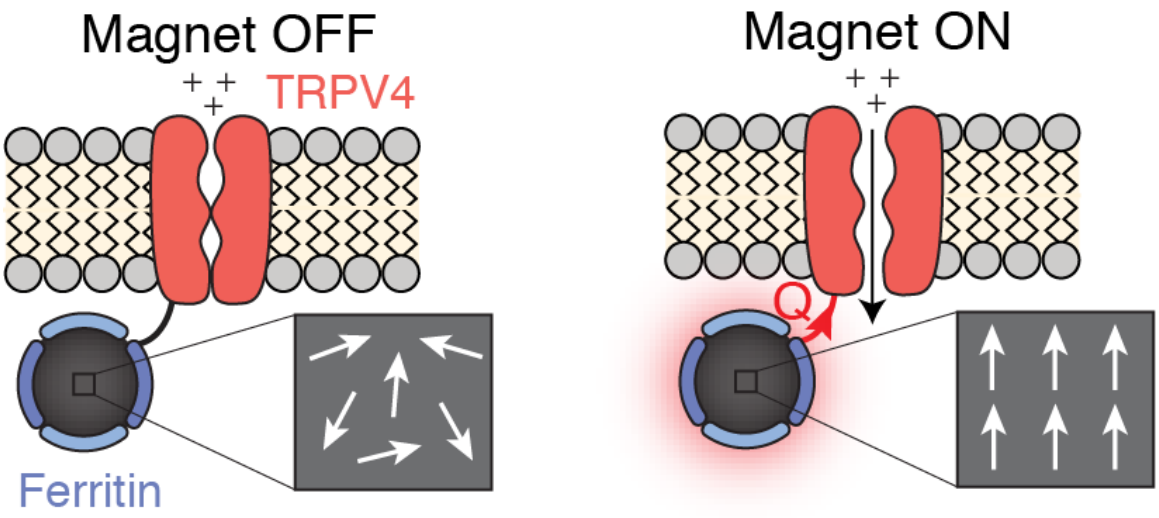


Figure 2.1 : Schematic shows how magnetocaloric effect in ferritin can activate nearby temperature sensitive ion channel such as TRPV4: An applied magnetic field will align the magnetic moments within paramagnetic ferritin nanoparticles, which will reduce the magnetic entropy. The reduced magnetic entropy generates heat (Q) via the magnetocaloric effect that can activate a nearby temperature-sensitive ion channel.

magnetic entropy is compensated by an increase in the lattice entropy, that results in the increase in temperature of the material. The heat due to increased temperature is then dissipated to the surroundings. Similarly, an adiabatic demagnetization gives rise to increased magnetic entropy and decreased temperature in the material. The adiabatic temperature change due to the magnetocaloric effect is given by:

$$\Delta T_{ad} = -\int_0^{B_{max}} \frac{T}{C_p}\left(\frac{\partial M}{\partial T}\right)_B dB \tag{2.1}$$

where $B_{max}$ is the maximum value of applied field. $C_p$ is the heat capacity of the magnetic material. M is the magnetization. T is the initial temperature of the system.

## 2.2 Heat generated by the magnetocaloric effect in ferritin

In the absence of a magnetic field, the magnetic moments within a paramagnetic material are randomly oriented, yielding no net magnetic moment (Fig. 2.1). However, ferritin is often modeled as a superparamagnetic nanoparticle [34], [35], [36]. In superparamagnetic materials a single magnetic domain rapidly reorients such that the particle displays no net magnetic moment when measured over periods of time longer than the relaxation time [37]. For small particles like ferritin this relaxation time is expected to be on the order of nanoseconds [34]. In either case of paramagnetic or superparamagnetic materials, when a magnetic field is applied, the moments align, thereby reducing the magnetic entropy (Fig. 2.1). This decrease in magnetic entropy is compensated by an increase in molecular vibrations which produces heat ($Q_f$) in ferritin: $Q_f = C_{p,ferritin}\Delta T_{ad}$, giving,

$$Q_f = \int_0^B T \left(\frac{\partial M}{\partial T}\right)_B dB, \tag{2.2}$$

The magnetization of ferritin is modeled using a Langevin function along with a linear field component to describe the predominant antiferromagnetically ordered phase of the ferrihydrite component; the Langevin function applies to the uncompensated spins on the surface of the ferritin and the linear contribution to the antiferromagnetic core [35]:

$$M = \mu \left[ coth(\frac{\mu_p B}{kT}) - \frac{1}{\frac{\mu_p B}{k_B T}} \right] + \chi_1 B. \tag{2.3}$$

where $\mu_p$ is the average magnetic moment for each ferrihydrite particle and is equal to 345 $\mu_B$ where $\mu_B$ is the Bohr Magneton. $M_0$ is the saturation magnetization, $\chi_1$ is the susceptibility of the antiferromagnetic core. Both $M_0$ and $\chi_1$ are temperature

dependent [35]. At 295 K, their values are $M_s \approx 0.25$ A m$^2$ kg$^{-1}$ and $\chi_1 \approx 0.08$ A m$^2$ kg$^{-1}$ T$^{-1}$.

When the magnetic energy is small compared to the thermal energy ($\mu_p B << k_B T$), we can use the small angle approximation to write the Langevin function as $M = M_0 \frac{\mu_p B}{3k_B T}$, using the first term of its Taylor series expansion. At physiological temperature and magnetic field of 275 mT, the simplified form of the magnetization is accurate within 1%. Therefore, we have:

$$M = M_0 \left[\frac{\mu_p B}{3k_B T}\right] + \chi_1 B \tag{2.4}$$

Using this small angle approximation for the Langevin function in Eq. 2.3 and considering the temperature dependence of $M_0$ and $\chi_1$, we can evaluate the integral in Eq. 2.2 to calculate the total heat generated by an applied magnetic field:

$$Q_f = \left[\left|\left(\frac{\partial M_0}{\partial T}\right)_B\right| + M_0 \frac{\mu_p}{3k_B T} + T\left|\left(\frac{\partial \chi_1}{\partial T}\right)_B\right|\right] \frac{B^2}{2}. \tag{2.5}$$

The values of $\left|\left(\frac{\partial M_0}{\partial T}\right)_B\right|$ and $\left|\left(\frac{\partial \chi_1}{\partial T}\right)_B\right|$ are obtained from the experimentally determined $M_0$ vs T and $\chi_1$ vs T curves [35] to be $1.34 \times 10^{-3}$ A m$^2$ kg$^{-1}$ K$^{-1}$ and $2.24 \times 10^{-4}$ A m$^2$ kg$^{-1}$ T$^{-1}$ K$^{-1}$ respectively.

Based on Eq. 2.5 we calculate that a 275 mT magnetic field will generate heat of 6 J mol$^{-1}$ of ferritin at room temperature (25 $^\circ$ C). There have been reports of a magnetite/maghemite component in ferritin which adds 1 J mol$^{-1}$ to the above calculation [38]. We have assumed that the temperature is constant during the magnetization process. As we will show in Section 2.3, the heat dissipates at a much slower rate than the magnetization time thus satisfying the adiabatic condition. Additionally, under the relevant experimental conditions we expect less than a 1 % change in the ferritin temperature, thus our estimate of $Q_f$ should be accurate in this isothermal

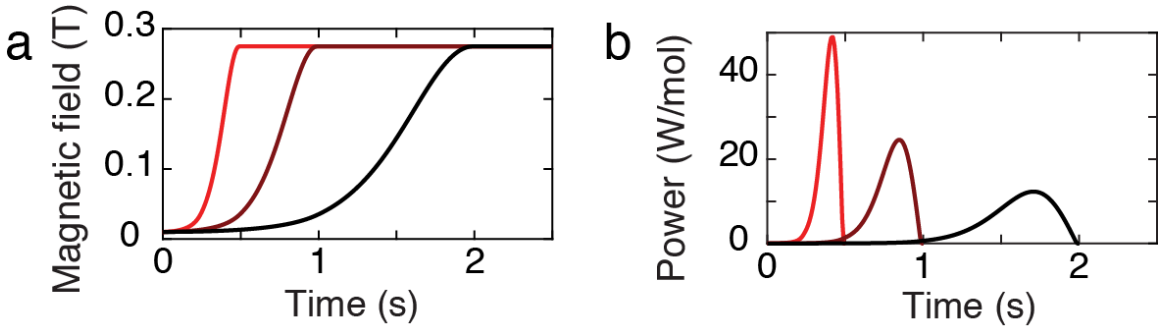


Figure 2.2 : (a) Applied magnetic field as a function of time for three different magnetization times ($t_M$ = 0.5 s, 1 s, and 1.5 s). (b) The power generated in ferritin due to magnetocaloric effect based on the magnetic field profiles in (a) for the three different magnetization times.

approximation.

The heating rate (or power) is written as the derivative of $Q_f$ with respect to time, which is often the quantity used to determine the heat transfer to the channel:

$$\frac{dQ_f}{dt} = \left[ \left| \left( \frac{\partial M_0}{\partial T} \right)_B \right| + M_0 \frac{\mu_p}{3kT} + T \left| \left( \frac{\partial \chi_1}{\partial T} \right)_B \right| \right] B(t) \frac{dB(t)}{dt}. \tag{2.6}$$

Figure 2.2 shows the waveform of the applied magnetic field (B(t)) for different values of $t_M$ and the corresponding power ($\frac{dQ_f}{dt}(t)$) generated in the ferritin as functions of time. It is important to note that magnetocaloric heating is a transient effect. Once the maximum field is reached, no more heat generated.

## 2.3 Heat transfer between ferritin and ion channel

### 2.3.1 Nanoscale heat transfer

Because thermoreceptors like TRPV4 open in response to changes in temperature, we must calculate the increase in the ion channel temperature due to the magnetocaloric heat generated in ferritin nanoparticle. Bulk heat transport equations predict that

nanoparticles show rapid and efficient heat transfer with the surrounding medium owing to their small size [26]. Consequently, it is expected that the temperature of the nanoparticle does not increase significantly above the bath temperature. We theoretically estimated the rate at which nanoparticles or proteins dissipate heat to be in the order of picoseconds using the values of their interfacial thermal conductance and heat capacities as follows:

Based on transient non-equilibrium molecular dynamics and the Fourier heat diffusion equation, the interfacial conductance ($U$) of protein-water interfaces is expected to be 200 MW m$^{-2}$ K$^{-1}$ [39]. Using transient absorption measurements, the interfacial thermal conductance at AuPd nanoparticle-water interface was determined to be 100 - 300 MW m$^{-2}$ K$^{-1}$. We thus use this value of $U$ =200 MW m$^{-2}$ K$^{-1}$ for the ferritin-water and channel-water interface. Then, based on their sizes ($\approx$ 12 nm sphere for ferritin [40] and $\approx$ 12 nm sided cube for TRPV4 [41]), we can estimate their interfacial conductance $G = UA$ to be $\approx 10^{16}$ W mol$^{-1}$ K$^{-1}$. Based on bulk ferrihydrite heat capacity of 80 J mol$^{-1}$ K$^{-1}$ [42], we estimate heat capacity of ferritin ($C_f$) to be $\approx 10^5$ J mol$^{-1}$ K$^{-1}$. Based on the size of TRPV4 and the heat capacities of proteins of similar sizes ([43]), we estimate the value of channel heat capacity ($C_c$) as $5 \times 10^5$ J mol$^{-1}$ K$^{-1}$. The heat dissipation time can then be approximately calculated as $\frac{C}{G}$ which is in the order of few picoseconds.

Even in the case of heat generated by strongly superparamagnetic iron oxide nanoparticles in the presence of a high frequency alternating magnetic field, the expected temperature gradient at the surface of the magnetic nanoparticle is negligible as calculated from classical heat transport laws. Using a value of G = 200 MW m$^{-2}$ K$^{-1}$ for interfacial thermal conductance between nanoparticle and water and $Q = 500$ W g$^{-1}$ as typically measured Specific Loss Power value for these nanoparticles, the

temperature gradient at the surface of a 10 nm nanoparticle can be calculated using the following formula from classical heat transfer laws:

$$\Delta T = \frac{Q}{4\pi R^2 G} \approx 10^{-8} K \tag{2.7}$$

where R is the radius of the particle. Additionally, the heat dissipation time ($\tau$) from the nanoparticles is estimated using the values of heat capacity for a 10 nm nanoparticle ($C_{NP} \approx 5 \times 10^{-18}$ J K$^{-1}$ based on 150 J mol$^{-1}$ K$^{-1}$ for bulk magnetite) to be:

$$\tau = \frac{C_{NP}}{4\pi R^2 G} \approx 10^{-11} K \tag{2.8}$$

However, recent experimental data indicate that the temperature in the immediate vicinity of iron oxide nanoparticles is many orders of magnitude higher than predicted by bulk heat transfer laws [30], [29], [31], [14], [27], [28]. In all these experiments, iron oxide nanoparticles were heated using alternating magnetic fields. As mentioned earlier in the context of magnetic hyperthermia in Section 1.2, the high frequency field results in the heating of the nanoparticle. There are two different types of experiments: 1. Chemical measurements: In these experiments, thermolabile molecules are attached at different distances from the nanoparticle and the temperature is obtained by quantifying the amount of dissociated molecules collected after magnetic heating [30], [29] (Table 1 a-b). 2. Optical measurements: Direct real-time measurements were done using temperature dependent fluorescent/luminescent molecules attached to surface of nanoparticle [31], [14], [27], [28] (Table 1 c-g). In all of these experiments, the temperatures at the surface of the particles was several degrees higher than the simultaneously monitored temperature of the bulk solution. It has also been shown that the nanoparticles take several seconds to cool back down

to bath temperature once the field is switched off (Table 1 c-g). Both the observations show a clear discrepancy between theoretical predictions and experiments.

Riedinger et al. [29] suggested that the reason for the discrepancy between expected and observed temperatures is because at the nanoscales, heat transfer is not accurately described by the Fourier law. At this scale, the mean free path length of heat carriers in the host medium, typically phonons, is greater than or comparable to the system dimensions. This is called the ballistic regime and in this regime, the phonon carriers travel through the system without scattering and consequently do not deliver energy. The heat transport in this regime is more accurately described by Boltzmann transport equations. However, Rabin et al. [44] calculated the mean free path of the heat carriers in water to be $\approx 0.3$ nm, which is still an order of magnitude less than the nanoparticle size. The theoretical models proposed by Rabin and Keblinski contradict these experimental findings. This mean free path length is so short that even at the nanoscale, the predictions of ballistic and Fourier heat transport law should be similar [45].

To explain the experimental data, Piñol et al. [27] proposed the existence of an additional resistance for heat transport at nanoscale interfaces. According to this model, the additional thermal resistance at the surface of the iron nanoparticle is about 10 orders of magnitude higher than expected based on bulk thermal resistance. In the absence of a mechanistic explanation for this frustrated thermal transport, we can make a model that matches the experimental data by assuming a decrease in the thermal conductance of the water surrounding the nanoparticles. Specifically, we define a water shell around the nanoparticle where the thermal conductance of the water is lowered by a factor of g* from the bulk. Therefore, g* is defined as follows:

$$g^* = \frac{G_{actual}}{G_{expected}} \tag{2.9}$$

where $G_{actual}$ is the experimentally observed thermal conductance of a shell of water. $G_{expected}$ is the thermal conductance of the shell calculated from classical laws and the known value of thermal conductivity of bulk water. We estimate a range of values for $g^*$ for the different types of experiments using the following methods:

For the distance dependent chamical measurements, we use:

$$\Delta T_{NP} = \frac{W}{g^* G_{shell}} \tag{2.10}$$

where $\Delta T_{NP}$ is the difference in temperature between the surface of the nanoparticle and the bulk. $W$ is the power generated by the nanoparticles, $G_{shell}$ is the thermal conductance due to a shell of water of radius $r$ around the particle and is calculated as:

$$G_{shell} = -\frac{K_w}{\frac{1}{r} - \frac{1}{r_{NP}}} \tag{2.11}$$

where $K_w$ is the thermal conductivity of water ( = 0.6 W m$^{-1}$ K$^{-1}$) and $r_{NP}$ is the radius of the nanoparticle. These distance dependent measurements have shown that temperature decays exponentially from the surface of the nanoparticle instead of the inverse-distance decay expected from Fourier laws. Temperature decay constants obtained from these measurements are over 1 - 2 nm. Therefore, we assume a water shell of thickness 1.5 nm for calculating $g^*$. Also note that the temperature change at the surface of the nanoparticle ($\Delta T_{NP}$) was obtained by the exponential fits to the distance dependent data. The estimated values of $g^*$ for the indirect measurements is shown in Table 1 (a-b).

The increased thermal resistance around the particles causes a slow heat dissipation, thereby leaving the particle at a higher temperature for longer. Direct real time measurements show that temperature decay times are over a few 100 seconds for magnetically heated nanoparticles in suspension, after turning off the field. A more recent experiment suggests decay times of 10 s for nanoparticles present on the surface of cell membrane (Table (h)) [16]. If $\tau_d$ is the measured decay rate, $g^*$ can then be estimated from $\tau_d$ using:

$$\tau_d = \frac{g^* G_{shell}}{C_s + C_{NP}} \tag{2.12}$$

where $G_{shell}$ is as described above and, $C_s$ is the heat capacity of the shell of water and $C_{NP}$ that of the nanoparticle. $C_s$ can be determined as:

$$C_s = C_{p,water} V_{shell} \rho_{water} \tag{2.13}$$

where $C_{p,water}$ is the heat capacity of water (= 4185 J kg$^{-1}$ K$^{-1}$), $V_{shell}$ is the volume of the water shell of outer radius $r$ and inner radius $r_{NP}$. $\rho_{water}$ is the density of water (= 1000 kg/m$^3$).

The estimated values of $g^*$ for the direct real-time measurements is shown in Table 1 (c-h). The value of $g^*$ obtained from the chemical measurements is higher and can be because the temperature data points used to estimate $\Delta T_{NP}$ are obtained outside the water shell.

Despite the number of experiments pointing toward frustrated thermal transport at the surface of these nanoparticles there remains some skepticism. For instance, Reidinger et al. report a linear dependence of the temperature increase of the nanoparticle on the amplitude of the magnetic field, which is in contradiction to the expected power law dependence on the specific loss power from superparamagnetic nanoparti-

cles [46]. Additionally, the method applied has been criticized to be too indirect and that the temperature and distance measurements near the nanoparticles need more elaborate calibration [47]. Even for more direct measurements based on fluorescence and photoluminescence, it is well known that fluorescence and photoluminescence quantum yield are affected by magnetic fields [48] and therefore the real-time temperature measurements performed as the nanoparticles are being heated in a magnetic field have been questioned. These studies lack a thorough examination of the effect of magnetic field on the fluorescent temperature probes. Additionally, clustering of magnetic nanoparticles in solution could also lead to changes in intensity of fluorescence. Thermometry based on fluorescence intensity has been further questioned because intensity is known to be concentration dependent. As alternative methods, fluorescence lifetime, maximum emission wavelength and a ratio of fluorescence intensities at two different wavelengths have been suggested for local temperature measurement [49].. However, none of these methods have been applied to the problem of measuring temperature around a magnetically heated nanoparticle.

To mitigate magnetic field effects on temperature measurement and to measure the thermal conductance at the vicinity of nanoparticle and water directly, we use silicon photonic thermometry. An optical thermosensor is immune to side effects due to high frequency alternating magnetic fields. Fiber optic thermometers are already widely used to measure temperature of nanoparticle suspensions subjected to magnetic fields because they are not affected by electromagnetic interference. However, they are not suitable for investigating thermal effects at the nanoscale near the vicinity of nanoparticles. In Chapter 4, we use a silicon ring resonator based temperature sensor to measure local temperature changes produced near nanoparticles due to an RF magnetic field. This method eliminates artifacts due to magnetic field effects on the

Table 1: Calculation of g* based on experimental measurements of temperature near the surface of magnetically heated iron oxide nanoparticles

| **Distance dependent chemical measurements** | | | |
|---|---|---|---|
| | g* | Decay constant (nm) | Reference |
| **a** | $10^{-10}$ | 2 | Dias2013 |
| **b** | $10^{-10}$ | 1 | Riedinger2013 |
| **Real time optical measurements** | | | |
| | g* | Decay rate constant ($s^{-1}$) | Reference |
| **c** | $1.5x10^{-13}$ | $2 \times 10^{-3}$ | Rinaldi2012 |
| **d** | $3.5 \times 10^{-13}$ | $1.6 \times 10^{-2}$ | Huang2010 |
| **e** | $1.3 \times 10^{-13}$ | $4 \times 10^{-3}$ | Piñol2015 |
| **f** | $1.4 \times 10^{-13}$ | $5 \times 10^{-3}$ | Dong2014 |
| **g** | $2 \times 10^{-12}$ | $10^{-1}$ | Munshi2017 |

a-f: Measurements from nanoparticles in suspension
g: Measurement from nanoparticles attached to cell membrane.

Figure 2.3 : Table listing calculated values of thermal conductance lowering factor $g^*$ based on experimental data.

nanoscale thermosensor and allows for accurate measurement of temperature in the vicinity of nanoparticles. Using the kinetics of temperature change obtained from these measurements, we determine the value of $g^*$ to be indeed close to $10^{-13}$. We assume this lowered thermal conductance that exists in the vicinity of synthetic iron oxide nanoparticles to also be present near the ferritin nanoparticle in *Magneto2.0*.

### 2.3.2 Nanoscale heat absorption

Temperature gradients across the protein that may result from heating at nanoscale distances could also increase the probability of activating the channels. For example, if critical conformational changes related to channel gating absorb energy before the channel reaches thermal equilibrium, the open probability of the channel will correspond to a higher effective temperature. Local heat absorption could occur in the case of TRPV4 by breaking a single hydrogen bond between the S5-S6 linker and TRP domain [50]. This bond has been reported to stabilize the closed state of the channel. Interestingly, this bond is located only 2.5 nm from the ferritin in *Magneto2.0* based on the recently solved structure of TRPV4 [51], raising the interesting possibility that heating this bond directly can activate the channel more effectively than uniform channel heating [24].

To estimate the effect of local heat absorption we can assume that a set of critical degrees of freedom ($f^*$) (e.g. a hydrogen bond) may absorb the energy and bias channel gating before the energy is equally distributed to all degrees of freedom ($f$) at thermal equilibrium. Thus we can define a heat capacity scaling factor $c^* = f^*/f$. Because temperature is a measure of the average kinetic energy in all degrees of freedom we can define an effective change in temperature for the critical degrees of freedom as $\Delta T^* = \frac{\Delta T}{c^*}$. Here, $c^*$ is used to set bounds on the kinetic energy (or effective temperature) of any particular degree of freedom that might preferentially influence temperature-sensitive channel gating. In this case we see that $c^*$ can vary between 1 (when heat is distributed between all degrees of freedom) and $1/f$ (when heat is absorbed by a single critial degree of freedom). Using the definition of heat capacity where $C_p = fk_B/2$ we can write the lower bound of $c^*$ as $\frac{k_B}{2C_p}$.

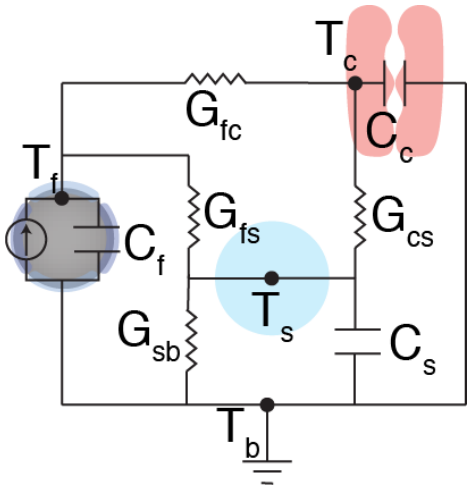


Figure 2.4 : Equivalent circuit model used to estimate heat transfer between the ferritin particle and ion channel. $T_f$, $T_c$, $T_s$, $T_b$ represent the temperature of the ferritin, channel, water shell and bath, respectively. $C_f$, $C_c$ and $C_s$ represent the heat capacities of the ferritin, channel and water shell respectively. $G_{fc}$, $G_{fs}$, $G_{cs}$ and $G_{sb}$ represent the thermal conductances between the ferritin and channel, ferritin and water shell, channel and water shell, and water shell and bath respectively.

### 2.3.3 Calculating channel temperature change

The temperature of the channel is estimated using the equivalent circuit in Fig 2.4. In this equivalent circuit model, $\frac{dQ}{dt}$, $T$, $C$, and $G$, are replaced with current, voltage, capacitance, and conductance, respectively. We also assume that the water bath remains at a constant temperature ($T_b$). Heat transfer between the ferritin (f)/channel (c) and the near water shell (s) are assumed to be due to interfacial conductance. As discussed above in Section 2.1, the interfacial conductances $G_{fs}$ and $G_{cs}$ can be found using the interfacial thermal conductance of 200 MW m$^{-2}$ K$^{-1}$ for protein-water and nanoparticle-water interfaces to be $\approx 10^{16}$ W mol$^{-1}$ K$^{-1}$, assuming a 12 nm sphere for ferritin and a cube of side 12 nm for the channel. Conductance between ferritin and channel can be calculated using protein conductivity of 0.15 W m$^{-1}$ K$^{-1}$ and assuming a linker of 5 amino acids' length to get $G_{fc} \approx 10^{15}$ W mol$^{-1}$ K$^{-1}$. $G_{sb}$ is

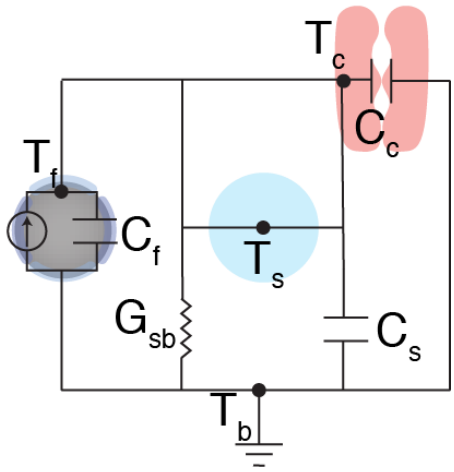


Figure 2.5 : Simplified Equivalent circuit for the case where $G_{fs}, G_{cs}, G_{fc} \ll G_{sb}$. At this limit, $G_{fs}, G_{cs}, G_{fc}$ in Fig. 2.4 can be replaced by short circuits.

the conductance of the water shell and is the same as $G_{shell}$ given in Eq. 2.11 with $r_{NP}$ given by radius of ferritn = 6 nm. In the case of lowered thermal conductances, ($G_{sb}$) will be multiplied by $g^*$ resulting in $g^*G_{sb} \approx 2 \times 10^5$ - $2 \times 10^8$ W mol$^{-1}$ K$^{-1}$ for $g^* = 10^{-13}$ - $10^{-10}$. In that case, $G_{fs}, G_{cs}, G_{fc} \ll G_{sb}$ and we can then simplify the equivalent circuit with $G_{fs}$, $G_{cs}$ and $G_{fc}$ shorted. The modified circuit is shown in Fig. 2.5. This circuit further simplifies to an RC circuit with $R = \frac{1}{g^*G_{sb}}$ and $C = C_s + C_c + C_f$.

To solve for temperature of the channel, ferritin and water shell, we write:

$$\frac{dT_c}{dt} = \frac{\frac{dQ_f}{dt} - g^*G_{sb}(T_c - T_b)}{C} \tag{2.14}$$

Because we expect heat to dissipate much slower (over few 10 seconds) compared to the magnetization time, we can assume all heat being provided at the same time and thereby replace $\frac{dQ_f}{dt}$ with $Q_f$:

$$\frac{dT_c}{dt} = \frac{Q_f\delta(0) - g^*G_{sb}(T_c - T_b)}{C} \tag{2.15}$$

The above differential equation can be solved easily to obtain:

$$\Delta T_c(t) = \frac{Q_f}{C}e^{-\frac{g^*G_{sb}}{C}t} \tag{2.16}$$

The maximum temperature change therefore is governed by the ratio of heat generated and the heat capacities and is $\approx 2\times10^{-6}$ K for all values of $g^*$.

As mentioned earlier, the effective temperature seen by the channel might be greater due to temperature gradients resulting in specific degrees of freedom absorbing heat preferentially. Effective temperature change can be written as:

$$\Delta T_c^*(t) = \frac{Q_f}{c^*(C_s + C_f + C_c)}e^{-\frac{g^*G_{shell}}{(C_s+C_f+C_c)}t} \tag{2.17}$$

Therefore, we have maximum effective channel temperature as a function of $c^*$ (given by $\frac{2\times10^{-6}}{c^*}$). $g^*$ governs the heat dissipation time in the form of $\tau_d = \frac{g^*G_{sb}}{C_s+C_f+C_c}$. The channel temperature change as a function of time is shown in Figure 2.6.

## 2.4 Modeling channel response using 2-state model

To determine how many channels would be activated by magnetocaloric heating we can model TRPV4 gating using a two-state thermodynamic model that is often used to describe the temperature response of thermoreceptors [52]. Although, TRP channels are expected to have more than two states, the following simple model with a single close and open state reproduces the functional form of the temperature sensitivity of the channel and is useful for estimating the channel open probability ($P_o$):

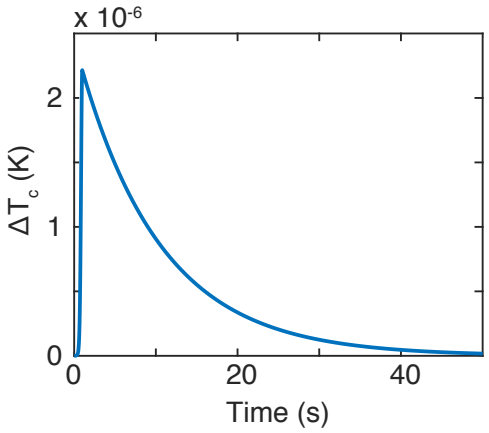


Figure 2.6 : Temperature change of channel as a function of time for $g^* = 10^{-12}$ and $c^* = 1$.

$$\mathrm{C} \underset{\beta}{\overset{\alpha}{\rightleftharpoons}} \mathrm{O} \tag{2.18}$$

In this model, the temperature sensitivity of the channel is the result of temperature dependent changes in the opening rate ($\alpha$) and the closing rate ($\beta$), which we can calculate from the Eyring equation [52]:

$$\alpha = k_0 e^{\frac{\Delta S_{a,open}}{R}} e^{\frac{-E_{a,open}}{RT}}, \tag{2.19}$$

$$\beta = k_0 e^{\frac{\Delta S_{a,close}}{R}} e^{\frac{-E_{a,close}}{RT}}, \tag{2.20}$$

where $E_{a,open}$ and $E_{a,close}$ are the activation energies for channel opening and closing, respectively. $\Delta S_{a,close}$ and $\Delta S_{a,open}$ are the activation entropies for opening and closing. $k_0$ is the frequency factor given by $\frac{k_B T e^2}{h}$ with $h$ being the Planck's constant. For a heat-gated channel, $E_{a,open} >> E_{a,close}$. Therefore, $\alpha$ is much more sensitive to a change in temperature than $\beta$. As a result, a small increase in temperature primarily

increases the number of channel openings. As a result, we can calculate the additional channel openings ($m$) due to the magnetocaloric effect as:

$$m = \int_{t_0}^{\infty} (\alpha(t)P_c(t) - \alpha(t_0)P_c(t_0))dt \tag{2.21}$$

where $t_0$ is the start of the magnetization. $P_c$ is the probability that the channel will be in the closed state. $P_c = 1 - P_o$, where $P_o$ is the probability of the channel being open. Note that we are assuming that the heat dissipation time ($\approx$ 10 seconds) is fast enough to neglect any adaptation by the cell to a change in temperature. This adaptation typically involves transcriptional regulation of calcium pumps (PMCA) and ion exchangers (NCX) on the time scale of tens of minutes [53], [54]. However, the heat dissipation time is much slower than the time it takes for the population of channels to reach the steady state value. ($t_s$). Although the population response time is not well characterized for TRPV4 we can set a limit for this time constant, based on the channel response times of similar channels (such as, TRPV1), which is in the order of a few $\mu$s to few ms [52]:

$$10^{-5}s \leq t_s \leq 10^{-1}s \tag{2.22}$$

Because the $t_s << 1/\tau_d$ we can assume that at each time point, $P_c$ is equal to the steady state value. At steady state,

$$\frac{\alpha}{\beta} = \frac{P_o}{P_c} \tag{2.23}$$

allowing us to write the equation for m (Eq. 2.21) as,

$$m = \int_{t_0}^{\infty} (\beta(t)P_o(t) - \beta(t_0)P_o(t_0))dt \tag{2.24}$$

Eq. 2.23 also gives:

$$P_o = \frac{1}{1 + e^{\frac{(\Delta H_g - T\Delta S_g)}{RT}}} \tag{2.25}$$

where $\Delta H_g = E_{a,open} - E_{a,close}$ is the gating enthalpy and $\Delta S_g = \Delta S_{a,open} - \Delta S_{a,close}$ is the gating entropy of the channel. Note that although the channel has a non-zero open probability at physiological temperatures, we expect the cell to adapt to maintain calcium homeostasis leading to no net calcium influx at steady state [55].

Because we can assume that the initial temperature of the channel is equal to the bath temperature ($T_b$) we can write $\beta(t)P_o(t)$ at any given time according to the change in effective temperature of the channel ($T_b + \Delta T_c^*(t)$).

Thus we can rewrite Eq. 2.24 as:

$$m = \int_{t_0}^{\infty} (\beta(T_b + \Delta T_c^*(t))P_o(T_b + \Delta T_c^*(t)) - \beta(T_b)P_o(T_b))dt \tag{2.26}$$

Because we expect the magnetocaloric effect to produce small changes in temperature (and accordingly small changes in $P_o$ and $\beta$), we can use the following Taylor approximations:

$$\beta(T_b + \Delta T_c^*(t)) \approx \beta(T_b) + \left.\frac{d\beta}{dT}\right|_{T_b} \Delta T_c^*(t), \tag{2.27}$$

$$P_o(T_b + \Delta T_c^*(t)) \approx P_o(T_b) + \left.\frac{dP_o}{dT}\right|_{T_b} \Delta T_c^*(t). \tag{2.28}$$

Substituting these approximations into Eq. 2.26 and neglecting terms $O(\Delta T_c^{*2})$ gives us:

$$m = \left.\frac{d(\beta P_o)}{dT}\right|_{T_b} \int_{t_0}^{\infty} \Delta T_c^*(t)dt. \tag{2.29}$$

Integrating Eq. 2.17 with respect to time gives

$$\int_{t_0}^{\infty} \Delta T_c^*(t)dt = \frac{Q_f}{g^* c^* G_{sb}} \tag{2.30}$$

Using Eq. 2.30 and Eq. 2.5 for $Q_f$ we can write the final form of $m$ in terms of the applied magnetic field:

$$m = \kappa \frac{1}{c^* g^*} \left. \frac{d(\beta P_o)}{dT} \right|_{T_b} B^2, \tag{2.31}$$

where

$$\kappa \equiv \frac{1}{G_{sb}} \left[ \left| \left( \frac{\partial M_0}{\partial T} \right)_B \right| + M_0 \frac{\mu_p}{3kT} + T \left| \left( \frac{\partial \chi_1}{\partial T} \right)_B \right| \right]. \tag{2.32}$$

## 2.5 Predictions for channel response based on Magnetocaloric effect

### 2.5.1 Magnetocaloric effect in *Magneto2.0*

To calculate $m$ from Eq. 2.31 we must evaluate the derivative $\frac{d(\beta P_o)}{dT}$, which we can approximate using experimental data and our two-state kinetic model after separating terms using the chain rule:

$$\frac{d(\beta P_o)}{dT} = \beta \frac{dP_o}{dT} + P_o \frac{d\beta}{dT}. \tag{2.33}$$

Differentiating Eq. 2.25 with respect to $T$, we obtain:

$$\frac{dP_o}{dT} = \frac{\Delta H_g}{4RT^2 cosh^2(\frac{\Delta H_g - T\Delta S_g}{2RT})} \tag{2.34}$$

Similarly, differentiating Eq. 2.20 with respect to $T$, we get:

$$\frac{d\beta}{dT} = k_0 e^{\frac{\Delta S_{a,close}}{R}} \left[ \frac{1}{T} + \frac{E_{a,close}}{RT^2} \right] e^{\frac{-E_{a,close}}{RT}} = \frac{\beta(T)}{T} \left[ 1 + \frac{E_{a,close}}{RT} \right] \tag{2.35}$$

To compute these derivatives (and thus the value of $m$) we must estimate the values of $\Delta H_g$, $\Delta S_g$, $E_{a,close}$, and $\Delta S_{a,close}$. We can estimate $\Delta H_g = 454$ kJ mol$^{-1}$ and $\Delta S_g = 1496$ J mol$^{-1}$ K$^{-1}$, by fitting published data for the $P_o$ [56] to the closed from solution for a two-state system (Eq. 2.25). Although experimentally determined values for $E_{a,close}$ and $\Delta S_{a,close}$ are unavailable for TRPV4, we can set bounds for these values based on the limits for the time constant, $t_s$ (Eq. 2.22) which depends on the rates, $\alpha$ and $\beta$ as follows:

$$t_s = \frac{1}{\alpha + \beta}. \tag{2.36}$$

Substituting for $\alpha$ and $\beta$ using Eq. 2.19 and 2.20 into this inequality (and the fact that $\Delta H_g = E_{a,open} - E_{a,close}$ and $\Delta S_g = \Delta S_{a,open} - \Delta S_{a,close}$) yields:

$$10^1 \leq k_0 e^{\frac{\Delta S_{a,close}}{R}} e^{\frac{-E_{a,close}}{RT}} \left[1 + e^{\frac{-(\Delta H_g - T\Delta S_g)}{RT}}\right] \leq 10^5. \tag{2.37}$$

For the above inequality to hold in operational temperature range of 20 - 45 °C, the range of allowable values for ($E_{a,close}$, $\Delta S_{a,close}$) should be within the triangular parameter space enclosed by the vertices (28 kJ mol$^-$1, -145 J mol$^{-1}$ K$^{-1}$), (0, -242 J mol$^{-1}$ K$^{-1}$), (0, -234 J mol$^{-1}$ K$^{-1}$). Thus we can select any point within this parameter space to compute a value of $m$. Fortunately, all points within this parameter space yield comparable values for $m$. Selecting the most extreme values within this space causes $m$ to vary by less than a factor of 4. For the purposes of estimating $m$ in this text we assume a value of $E_{a,open} = 14$ kJ mol$^{-1}$ and $\Delta S_{a,open} =$ -192 J mol$^{-1}$ K$^{-1}$ which is approximately at the center of the parameter space such that the range of allowed $m$ values are within a factor of 2.

Note that one can further simplify the expression for $m$ by making the approximation that $P_o \frac{d\beta}{dT} \ll \beta \frac{dP_o}{dT}$, and hence we can write Eq. 2.33 as:

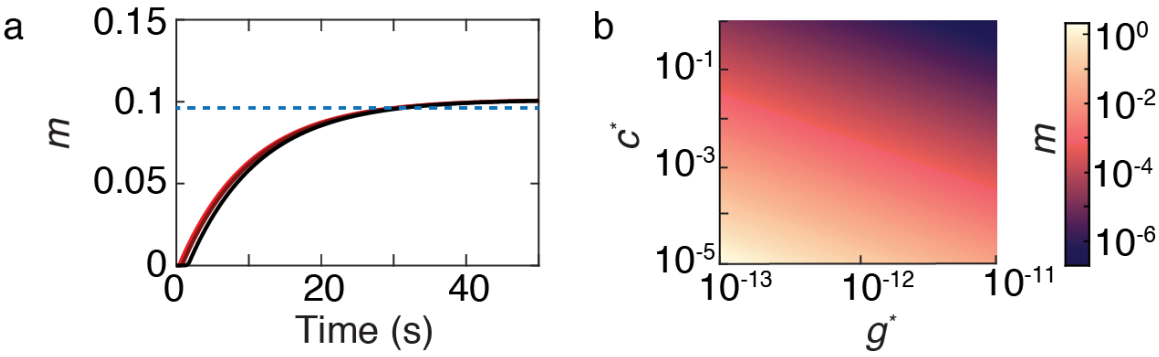


Figure 2.7 : (a) Number of additional channel openings (m) due to the magnetocaloric effect based on Eq. 2.21. The dashed blue line indicates the maximum percentage of channels that open as derived by the analytical expression for m in Eq. 2.31. Note that the total number of channels that open depends on the maximum value of the magnetic field and not the rate of magnetization. Calculations assume $T_b = 25$ °C, $c^* = 10^{-5}$ and $g^* = 10^{-12}$ (b) The fraction of channels that respond depends on the value of $c^*$ (heat capacity scaling factor) and $g^*$ (thermal conductance scaling factor), which can vary by orders of magnitude depending on the biophysical mechanism that triggers temperature-dependent channel gating. We expect that the m values near $10^{-5}$ and greater would yield a physiological response.

$$\frac{d(\beta P_o)}{dT} \approx \beta \frac{dP_o}{dT} \tag{2.38}$$

This approximation is accurate to within 9%.

Figure 2.7 (a) shows the time evolution of the number of additional openings per channel for each magnetic stimulus. Figure 2.7 (b) gives the maximum predicted values of $m$ for *Magneto2.0* over the range of expected thermal conductivity scaling factors ($g^*$) and effective heat capacity scaling factors ($c^*$).

### 2.5.2 Magnetocaloric effect in MagM8

The magnetocaloric mechanism leads to the design of new proteins that are based on the demagnetization of an associated magnetic nanoparticle, such as ferritin, gating a

cold-activated ion channel. Cold-sensitive channels have closing rate ($\beta$) much larger than the opening rate ($\alpha$). Therefore, more channels open in response to decrease in temperature. For TRPM8, the opening rate ($\alpha$) is characterized by experimentally determined values of $E_{a,open}$ of 16 kJmol$^{-1}$ and $\Delta S_{a,open}$ of -167 mol$^{-1}$ K$^{-1}$ [52]. The closing rate ($\beta$) is characterized by $E_{a,close}$ of 173 kJmol$^{-1}$ and $\Delta S_{a,close}$ of 390 J mol$^{-1}$ K$^{-1}$. Consequently, we have $\Delta H_{gating}$ = -157 kJ mol$^{-1}$ and $\Delta S_{gating}$ = -557 J mol$^{-1}$ K$^{-1}$. Because TRPM8 is also voltage sensitive, the $\alpha$, $\beta$ and $\Delta P_{open}$ and $\Delta P_{close}$ have a voltage dependent term in them, which corresponds to the electrical work done by the channel towards gating:

$$\alpha = k_0 e^{\frac{\Delta S_{a,open}}{R}} e^{\frac{-E_{a,open}}{RT}} e^{\frac{\delta z F V}{RT}}, \tag{2.39}$$

$$\beta = k_0 e^{\frac{\Delta S_{a,close}}{R}} e^{\frac{-E_{a,close}}{RT}} e^{\frac{-(1-\delta) z F V}{RT}}, \tag{2.40}$$

$$P_{open} = \frac{1}{1 + e^{\frac{(\Delta H_g - T\Delta S_g) - zFV}{RT}}} \tag{2.41}$$

Here, $z$ is the gating charge which is 0.82 for TRPM 8 [52], $\delta$ is the fraction of $z$ moved in the outward direction and is equal to 0.5, $F$ is the Faraday constant, $V$ is the transmembrane voltage. Consequently, we obtain for TRPM8:

$$\frac{dP_{open}}{dT} = \frac{\Delta H_g - zFV}{4RT^2 cosh^2(\frac{\Delta H_g - T\Delta S_g - zFV}{2RT})} \tag{2.42}$$

and,

$$\frac{d\beta}{dT} = \frac{\beta(T)}{T}\left[1 + \frac{E_{a,close} - (1-\delta)zFV}{RT}\right] \tag{2.43}$$

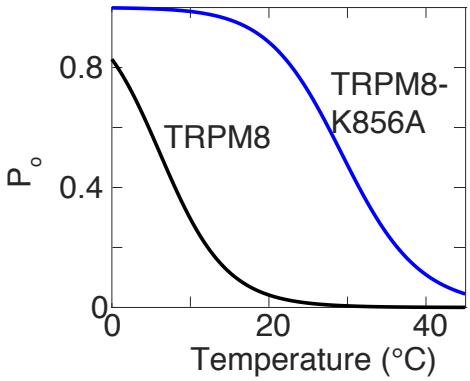


Figure 2.8 : Temperature vs $P_o$ curves for wild type TRPM8 and K856A mutant of TRPM8. Note that the mutation shifts the temperature range and is more active at room temperature.

The temperature response curve for TRPM8 is shown in Fig. 2.8. To shift the operational temperature range to higher temperatures, we use the K856A mutant which is active at room temperature [57]. The values of gating enthalpy and entropy of the K856A mutant are slightly different and given by: $\Delta H_{gating}$ = -160 kJ mol$^{-1}$; $\Delta S_{gating}$ = -520 J mol$^{-1}$ K$^{-1}$ [57]. The temperature response curve for this mutant is also shown in Fig. 2.8. Although values of opening and closing activation energies and entropies are not determined experimentally, we constrain the values of the channel response time, $t_s$ between $10^{-5}$ and $10^{-2}$ s$^{-1}$ within its operating temperature range of 10 - 40 °C ([52], [57]) and obtain a triangular parameter space enclosed by vertices ($E_{a,close}$, $\Delta S_{a,close}$) = (175 kJ mol$^{-1}$, 401 J mol$^{-1}$ K$^{-1}$), (0, -150 J mol$^{-1}$ K$^{-1}$), (0, -210 J mol$^{-1}$ K$^{-1}$). For the purpose of calculating $m$, we take the parameter values from the first vertex because they are closest to the values for TRPM8.

Fig. 2.9 shows values of $m$ for a single magnetic stimulus obtained for MagM8 using the above parameters for various values of $c^*$ and $g^*$.

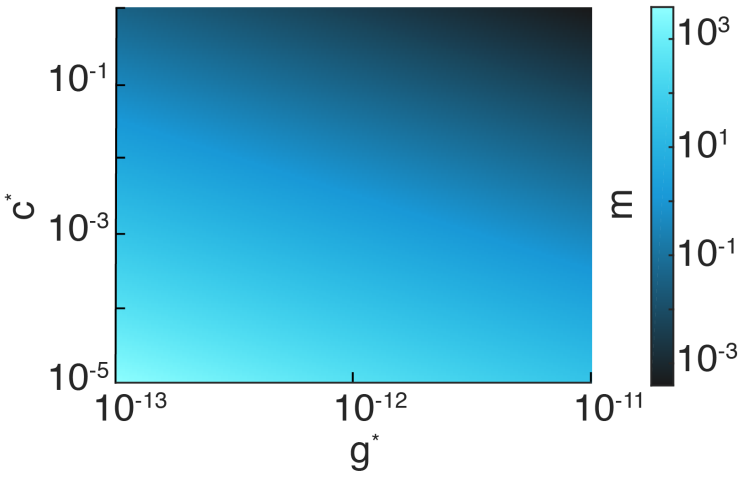


Figure 2.9 : Number of additional channel openings ($m$) due to magnetocaloric cooling of MagM8 as function of $c^*$ and $g^*$.

### 2.5.3 Magnetocaloric modulation of neural activity

From Figure 2.7 we find that at the least extreme, approximately 1 in 10,000 *Magneto2.0* channels would be activated by applying a 275 mT magnetic field. Transfected hippocampal neurons can express between 160,000 and 1,000,000 heterologous functional TRPV1 channels [58], thus we would expect magnetic responses that could be at least as large as approximately 10 to 100 additional channel openings per cell. Even if only a small number of channels might be activated by the magnetocaloric effect, these gating events could affect neuronal activity due to the large ionic conductance of TRPV4. We can calculate the current through a TRPV4 channel using the following:

$$q = (E_{Ca^{2+}} - V_{m,neuron})g_{Ca^{2+}}, \tag{2.44}$$

where $E_{Ca^{2+}}$ = 129 mV is the calcium reversal potential [59], $V_{m,neuron}$ = -70 mV is the resting membrane potential of a neuron, $g_{Ca^{2+}} \approx 60$ pS is the calcium conductance

of the channel [56]. Using these values, we obtain an average current of 10 pA per channel at physiological temperature for an average open time of $\tau_o = 5$ ms. The average open time ($\tau_o$) is given by $1/\beta$.

The magnitude of current should be above a threshold defined by the rheobase, which is the minimum current amplitude of infinite duration that gives rise to an action potential in a neuron and it ranges between 15 - 900 pA [60], [61], [62]. As the current level increases, the required pulse duration decreases. The pulse duration corresponding to twice the rheobase current is called 'chronaxie'. The minimum required additional number of channel openings for eliciting an action potential will then be given by:

$$m = \frac{2 \times Rheobase/singlechannelcurrent}{No.ofchannelspercell \times Probability(\tau_o > chronaxie)} \tag{2.45}$$

The values of chronaxies range from 1 - 10 ms [63], and our average estimated open time is well within this range. We therefore get a value of m to be between $3 \times 10^{-6}$ and $10^{-3}$. These values fall well within the range of our theoretical predictions, Fig. 2.7) and could lead to action potentials or affect firing rates in the majority of transfected neurons.

### 2.5.4 Magnetocaloric effect on calcium concentration in HEK cells

The large ionic conductance of TRPV4 could also lead to the increase in calcium observed in our experiments and reported by [1]. Based on the fact that Fluo-4 (the indicator used for our experiments) can resolve a change of at least 85 nM [64] near the intracellular calcium concentration of 100 nM [59], we estimate that we can resolve a calcium influx of roughly $1.7 \times 10^5$ ions or greater in an HEK cell with a radius of 15 $\mu$m.

We can estimate that the average increase in the number of calcium ions, $n$ per channel opening is approximately $1.5 \times 10^5$ according to:

$$n = \frac{1}{2e}(E_{Ca^{2+}} - V_{m,HEK})g_{Ca^{2+}}\tau_o, \tag{2.46}$$

where $E_{Ca^{2+}}$ = 129 mV is the calcium reversal potential [59], $V_{m,HEK}$ = -45 mV is the resting membrane potential of HEK cells [65], $g_{Ca^{2+}} \approx 60$ pS is the calcium conductance of the channel [56], $e$ is the charge of a proton and $\tau_o = 5$ ms is the average open time of an activated channel (determined by $1/\beta$). Using these values, we see that a single channel opening is near our expected limit for a detectable change in Fluo-4 fluorescence. We estimate approximately 1000 channels per HEK based on reported current densities for TRPV4 in HEKs (300 pA/pF at -100 mV, activated with agonist, 4$\alpha$PDD [66]), and a single channel total conductance value of 60 pS [56], and an average capacitance of 20 pF for HEKs (as measured in our experiments). Therefore, $m$ values on the order of $10^{-3}$ (which fall within the range of our theoretical predictions, Fig. 2.7) would lead to a detectable increase in $Ca^{2+}$ levels in each cell from a single magnetic stimulus. Near the minimum value of m, we anticipate about 1 in 10 cells responding due to a single magnetic stimulus. However, with repeated stimuli and the fact that not all cells need to respond for us to measure a magnetic response from the population, we expect that $m$ values as small as $10^{-5}$ could explain our experimental results. Note that we predict channel responses much higher than this value (Fig 2.7 and Fig. 2.9).

### 2.5.5 A note on thermal noise

Even though the temperature rise caused by the magnetocaloric effect is very small and lower than Maxwell-Boltzman thermal fluctuations of a single channel (calculated

below), the cell is not sensitive to those thermal fluctuations because its response is governed by the ensemble average of the thermal fluctuations of all of its channels. The more the number of channels, the lesser the ensemble average of these fluctuations are going to be. Or in other words, the effect on the cell of a channel's positive deviation from average temperature is offset by that of another channel's negative deviation. Hence, although the increase in temperature caused by magnetocaloric heating is low, it causes a net increase in the number of channel openings at the cellular level.

The standard deviation of thermal fluctuations in an ensemble of particles is given by [67]:

$$\overline{\Delta T} = \sqrt{\frac{kT^2}{Nc_v}} \tag{2.47}$$

where $N$ is the total number of particles and $c_v$ is the heat capacity of each particle. Using heat capacity of a single channel, we obtain $\overline{\Delta T}$ of 1.2 K for a single channel. For an ensemble of $N$ channels in a cell, the $\overline{\Delta T}$ becomes $1.2/\sqrt{N}$ K. These fluctuations are governed by atomic collisions that occur over a timescale of $10^{-14}$ s [59]. However, channel response times are in the order of a few milliseconds. If we look at the sample average of these fluctuations over that timescale, we get:

$$\Delta T_{s.e.m} = \frac{\overline{\Delta T}}{\sqrt{t_{sam}/10^{-14}}} \tag{2.48}$$

where $t_{sam}$ is the sampling time and sampling rate is $10^{-14}$ s. If we sample over 1 ms, we obtain 0.01 $\mu$K for $\Delta T_{s.e.m}$ of the ensemble of channels in a neuron (with 160,000 channels), which is much less than the minimum temperature change obtained from magnetocaloric effect ($\approx 1$ $\mu$K). Therefore, it is reasonable to expect the small changes in temperature caused by magnetocaloric effect to have a significant physiological effect on the cell.

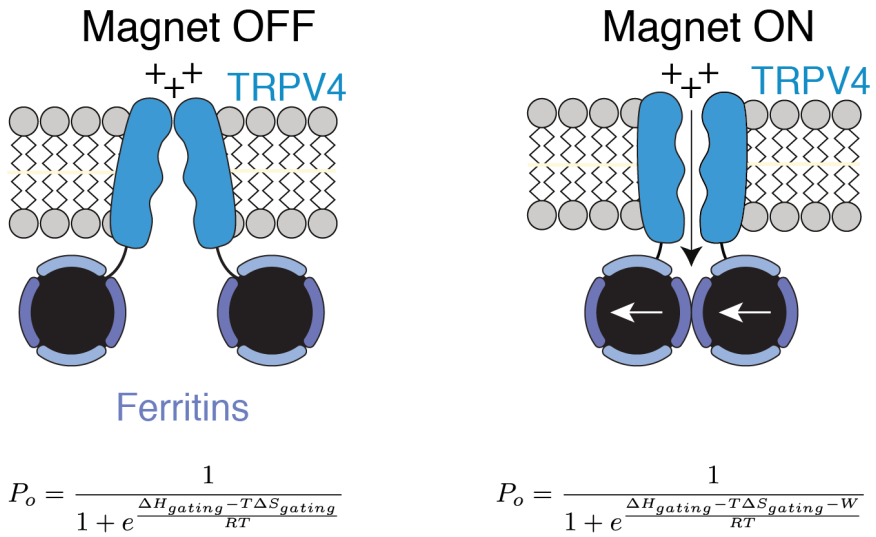


Figure 2.10 : Schematic representation of effect of mechanical work done by ferritin on the channel that leads to change in the open probability of the channel ($P_o$) at a given temperature T.

## 2.6 Alternate mechanisms

### 2.6.1 Mechanism based on temperature dependent mechanical response

In this section, I will discuss an alternate approach towards explaining how *Magneto2.0* works. This approach is based on a temperature-dependent mechanical response of the channel.

Recall that electrical work contributes to channel opening for TRPM8 in the form of Eq. 2.41. Analogously, this mechanism is based on magnetic force doing work ($W$) towards channel gating in the presence of a magnet. A schematic representation of the mechanical effect is shown in Figure 2.10

Force is exerted on the channel by neighboring ferritins interacting with each other due to their induced magnetic moments in a magnetic field. In this section, we will confine ourselves to the case where the orientation of the field is parallel or perpendicular to the membrane, giving the maximum interaction. The force also depends

very steeply on the distance between the ferritins, as can be seen from the following equation for force between two dipoles of equal magnetic moment, $\mu$ seperated by distance, d. In the attractive configuration, force is given by:

$$F = \frac{3\mu_0}{2\pi}\frac{\mu^2}{d^4} \tag{2.49}$$

where $\mu_0$ is the magnetic permeability constant, $\mu$ is the magnetization of ferritin in an applied field of strength $B$. $d$ is the distance between centers of the two ferritins. $\mu$ is 345 $\mu_B$ as seen in Section 2.2. The channel and ferritin have almost equal diameters (of $\approx$ 12 nm). Therefore, it is reasonable to assume that if there are two ferritins per channel, they would be almost touching each other. So, we could set $d$ to be the distance between the centers of the two ferritins equal to 12 nm. The work done towards opening of the channel by this force is given by:

$$W = F.x \tag{2.50}$$

where $x$ is the distance by which the ferritin pulls the channel to open it. Based on cryo-electron microscopy structure of TRPV2, a related protein, we estimate a channel pore size increase of 3 nm when it opens [68], so we can approximate x to be 3 nm. This gives us a work term of 0.001 J mol$^{-1}$.

The increase in the open probability of channel in the presence of the magnet at a given temperature is given as:

$$\Delta P_o = \frac{1}{1+e^{\frac{\Delta H_{gating} - T\Delta S_{gating} - W}{RT}}} - \frac{1}{1+e^{\frac{\Delta H_{gating} - T\Delta S_{gating}}{RT}}} \tag{2.51}$$

The amount of additional $Ca^{2+}$ ions entering each channel per unit time ($n$) due to the difference in channel open probability is given by

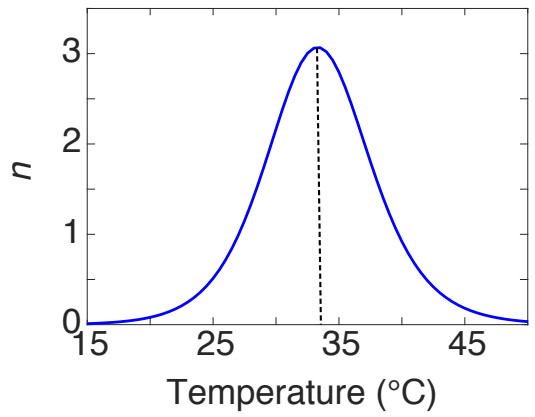


Figure 2.11 : Temperature dependent effect of work done by ferritin ($W$) on the number of additional $Ca^{2+}$ entering per channel per second ($n$). Dashed line indicates the temperature $T_{50}$ where effect of the work done is maximum.

$$n = \frac{1}{2e}\Delta P_o g_{Ca^{2+}}(E_{Ca^{2+}} - V_m) \tag{2.52}$$

Using values for $g_{Ca^{2+}}$, $E_{Ca^{2+}}$ and $V_m$ equal to 60 pS, 129 mV and -45 mV as mentioned in Section 2.4, we obtain $n$ equal to 1 $Ca^{2+}$ ion every 2.5 seconds at 298 K. The maximum value of $P_o$ in Eq 2.51 is obtained for the case $\Delta H_{gating} - T\Delta S_{gating} = 0$, or in other words, at $T = T_{50} = \frac{\Delta H_{gating}}{\Delta S_{gating}}$:

$$\Delta P_o|_{T_{50}} = \frac{1}{1 + e^{\frac{-W}{RT}}} - \frac{1}{2} \tag{2.53}$$

And it decreases as we go farther from $T_{50}$. For temperatures beyond the operation range of a channel, the effect of $W$ is negligible as shown in Fig. 2.11. At $T_{50}$, this mechanism leads to additional charge of 3 $Ca^{2+}$ ions entering per second. A single TRPV4 channel open for 1 ms allows 10,000 $Ca^{2+}$ ions to pass through it. In comparison to this, the result of $< 1$ $Ca^{2+}$ ions per second seems very less, but from the following calculation, it can be seen that this change in $Ca^{2+}$ is detectable by Fluo-4: We can again use the dissociation constant, $K_d$ for Fluo-4 of 335 nM to determine

if this calcium influx is detectable. $K_d$ is a measure of the ion concentrations that an ion specific dye can reliably measure. Typically, these concentrations are between $0.1 - 10 \times K_d$. This means, Fluo-4 can measure a concentration change of 22,200 ions per cell at the lower end. In this calculation, I have assumed a cell to be a sphere of radius 15 $\mu m$. With 1000 channels per HEK and one $Ca^{2+}$ ion entering per 2.5 s, we would need the magnet to be on for 55 s before seeing a detectable response. This is a slow response, but it is consistent with the slow calcium rise over time as shown by Wheeler et al. This will also be the trend shown in experiments performed by us, as we will see in the next chapter.

However, as we will also see in the next chapter, a slow rise in calcium is seen only in the presence of a repeated magnetic stimulus and not in the case of a constant applied magnetic field suggesting that the process of magnetization (and not steady magnetic fields) gives rise to the calcium signal, which is expected for the magnetocaloric effect.

# Chapter 3

# Experimental Verification of Magnetocaloric Mechanism

This chapter talks about the experiments performed to test the hypothesis that Magneto2.0's magnetic sensitivity is indeed thermally mediated. TRPV4 has seperate activation pathways for temperature and mechanical responses. By independently inhibiting each one of the two sensitivities, we can understand their involvement in the magnetic sensitivity of *Magneto2.0*. The two different pathways (Mech and Therm) are shown in Figure 3.1(a). Additionally, I will also discuss experimental results of magnetic stimulation of *MagM8*.

## 3.1 Pathways for temperature and mechanical sensitivity of TRPV4

TRPV4 is activated by osmotic cell swelling, heat, phorbol ester compunds and 5',6'-epoxyeicosatrienoic acid [2]. The channel's response to mechanical shock in the form of osmotic cell swelling was shown to involve an indirect pathway mediated by Phospholipase $A_2$ ($PLA_2$) enzyme-dependent release of Arachidonic acid. It has been shown that 4-bromophenacyl bromide (pBPB), a $PLA_2$ inhibitor, prevented TRPV4 activation by extracellular hypotonicity, while leaving the temperature sensitivity of the channel unaffected. pBPB was used in our experiments to reduce the mechanical sensitivity of TRPV4. This condition, referred to as (-)Mech, showed reduced

sensitivity to hypo-osmotic shock but unaffected temperature sensitivity as measured by fluorescence imaging using calcium-sensitive dye, Fluo-4 in transfected HEK cells (Figure 3.1 (b) (-)Mech). However, there is also a direct pathway for mechanical activation of TRPV4 by mechanical strain in the cytoskeleton backbone of focal adhesion [69] that we have not explored in our experiments yet.

Vriens et al. also showed that mutating a tyrosine residue (Tyr-555) in the N-terminal part of the third transmembrane domain of TRPV4 to an alanine (Y555A mutant) strongly reduces its thermal sensitivity. This mutant did not have any effect on the channel's ability to respond to osmotic shock. So we created a version of *Magneto2.0* with the Y555A mutation. This variant, referred to as (-)Therm, showed normal response to hypo-osmotic shock, but reduced temperature sensitivity (Figure 3.1 (c) (-)Therm).

## 3.2 Magnetic sensitivity of *Magneto2.0* is thermally-mediated

For each of *Magneto2.0*, (-)Therm and (-)Mech, magnetic field of approximately 275mT was applied using a neodynium rare earth permanent magnet attached to a computer-controlled translation stage at a frequency of 0.08 Hz for 270 seconds. This stimulus waveform was primarily designed to test the magnetocaloric theroy. The rationale for using such a magnetic stimulus is: 1. Heat is only produced when field increases and not once it reaches maximum value. For repeated activation of the channels, we would need multiple magnet stimuli. 2. The repeated stimulus cannot be too fast, otherwise the magnetocaloric heating will quickly offset cooling due to demagnetization. I discuss why magnetocaloric effect might not play a significant role in high-frequency alternating field stimulation in Section 4.3.

Channel response to the field was measured using the calcium-sensitive dye, Fluo-

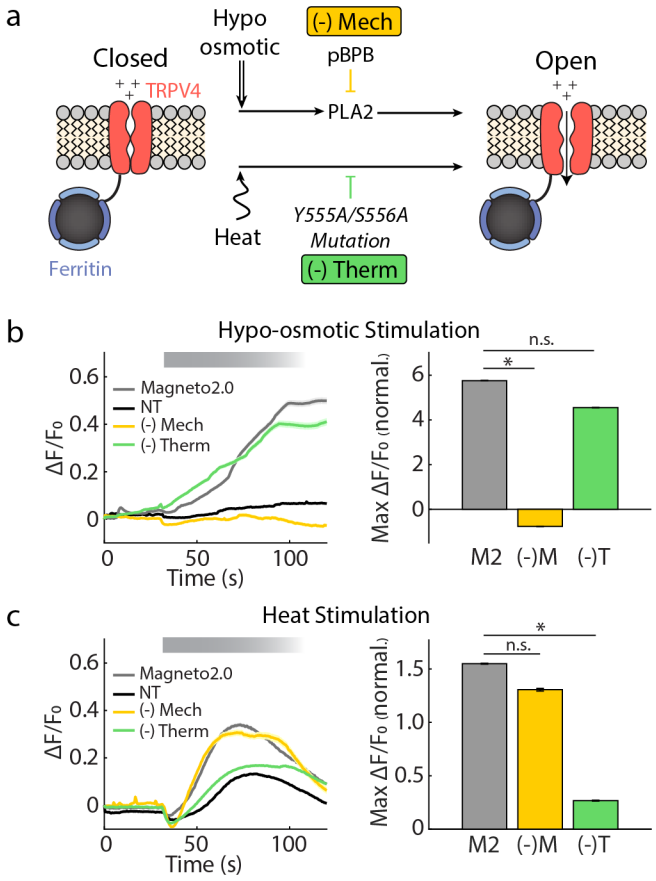


Figure 3.1 : Inhibition of distinct activation pathways in *Magneto2.0*: (a) Schematic representation of the two independent pathways by which TRPV4 responds to temperature and mechanical stimuli. pBPB inhibits the PLA2 dependent response of TRPV4 to mechanical stimus [2]. This condition is termed (-)Mech. The mutation Y555A/S556A inhibits the temperature response of TRPV4 [2]. This condition is refered to as (-)Therm. (b) Calcium imaging with Fluo-4 shows that (-)Mech (and not (-)Therm) has reduced sensitivity to hyoposmotic stimulation compared to WT *Magneto2.0* (c) Calcium imaging shows that (-)Therm has a significantly reduced response to thermal stimulation (40°C) compared to (-)Mech and WT *Magneto2.0*. Bold lines on the plots to the left represent mean values and shaded regions represent ± s.e.m. Bar plot shows the ratio of maximum $\Delta F/F_0$ for (-)Mech and (-)Therm conditions compared to non-transfected cells.

4. We found from our experiments that the (-)Mech variant of *Magneto2.0* responded to magnetic stimulation while the (-)Therm variant did not, suggesting that magnetic sensitivity is indeed a thermal response as predicted by our hypothesis. In WT *Magneto2.0* and (-)Mech, we observed a slow increase in intracellular calcium when we apply the magnetic field stimulus (Figure 3.2 (a) and (b)). We note that this slow increase in calcium is similar to the data reported by Wheeler et al. in transfected HEK cells (Figure 1.2). No such increase in calcium was observed in (-)Therm expressing cells (Figure 3.2 (c)), indicating that the magnetic response relies on the thermal activation pathway of TRPV4.

But the same results can also be explained by the second mechanism proposed in Section 2.6. With the stimulus waveform described above, the cells experience maximum field of 275mT for $\approx$ 70s , which is enough time to let 28,000 calcium ions at 1 ion per channel every 2.5 seconds. This will give a detectable change in Fluo-4 signal over time. Within this framework, we can explain the results obtained from the Mech(-) and Therm(-) experiments as follows:

1. (-)Therm: The Y555A mutant does not respond to temperature changes in the physiological range. It is likely that its operational range and $T_{50}$ are far from experimental temperature ranges, and as seen in Fig. 2.11, the work done by ferritin will have negligible effect on the channel in that case. Hence we don't see a response in the Y555A mutant to the magnet.

2. (-)Mech: pBPB inhibits an indirect pathway for mechanical response by inhibiting PLA2, an enzyme that detects mechanical stress. But the ferritin force acting on the channel is a direct pathway similar to the one reported in [69] towards channel activation, which is still uninhibited. Hence, this framework would still explain why the Mech(-) shows a response to magnet.

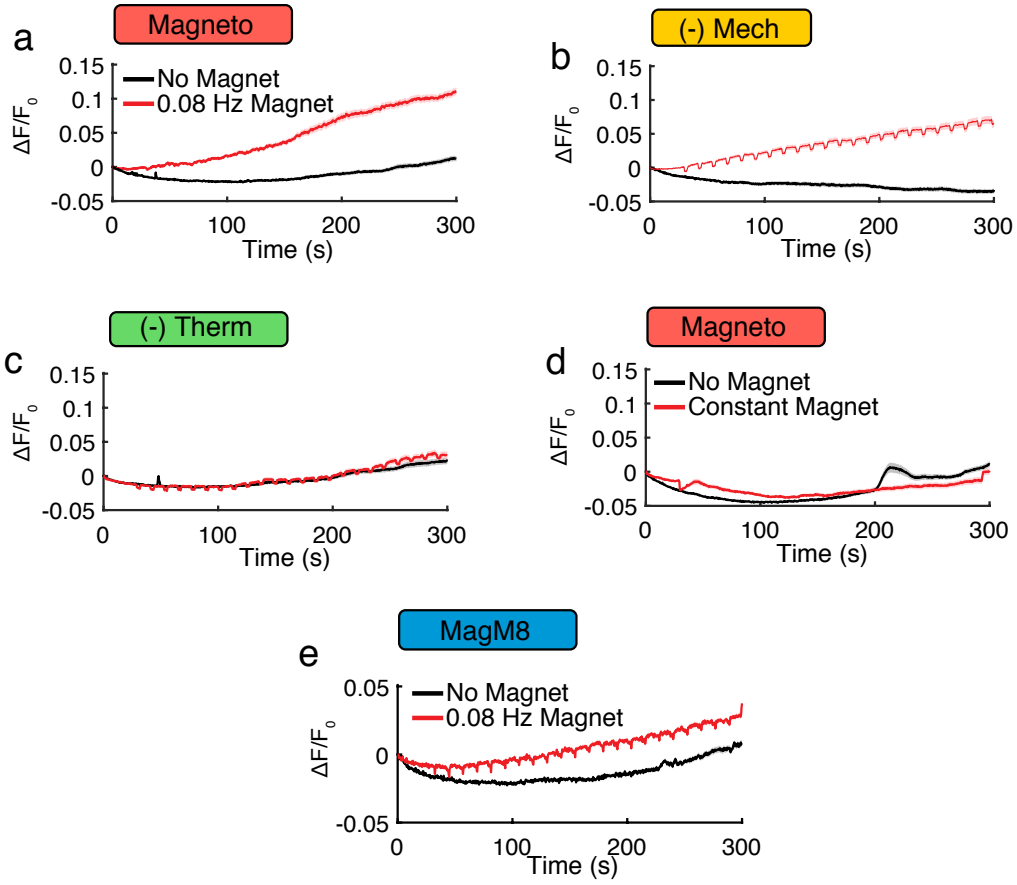


Figure 3.2 : Average value of $\Delta F/F_0$ over time shows that *Magneto2.0* (a) and (-)Mech (b) both show responses to magnetic stimulation of 0.08 Hz, while (-)Therm (c) does not, verifying the thermal activation mechanism. Shaded regions represent s.e.m. Mean $\Delta F/F_0$ values are averaged using a 20 s sliding window. Magnetic response is also not seen for *Magneto2.0* stimulated with a constant magnetic field of 275 mT (d), indicating that it is the process of magnetization and not the steady field that results in a response. (e) Magnetic response of *MagM8* to 0.08 Hz field.

To test the second mechanism, we performed experiments where a constant magnetic stimulus of 275 mT was applied for 270 s. However, no significant increase in calcium was seen as shown in Fig. 3.2 (d). This suggests that the process of magnetization, such as in the case of magnetocaloric effect gives rise to the calcium signal and not the steady magnetic field.

## 3.3 Magnetic response of *MagM8*

The magnetocaloric effect that we verified on *Magneto2.0* also predicts that the demagnetization of an associated magnetic nanoparticle should be able to gate a cold-activated ion channel. In order to test that hypothesis which would further support the magnetocaloric theory, we fused the cold-activated TRPM8 protein to ferritin. We mutated the S4-S5 linker region (K856A) in order to shift the temperature response-curve to higher temperatures, and allow the channel to be active at room temperature, as explained in Section 2.5.2. The resulting protein is named **MagM8**. The magnetic stimulation of *MagM8* was performed using the protocol already used for *Magneto2.0* (0.08 Hz for 270 seconds), and over the course of the recording, the stimulated transfected cells displayed a significant increase in intracellular calcium compared to the non-stimulated cells (Fig. 3.2(e)). Taken together, these data support the activation of *MagM8* by ferritin demagnetization.

## 3.4 Methods

**Cell culture and molecular biology** HEK293 cells were obtained from ATCC and were cultured in DMEM supplemented with 10% FBS and 1% pen-strep. Plasmids, pcDNA3.0-*Magneto2.0*-p2A-mCherry and pEGFP-TRPM8 were obtained from Addgene. Sequences were assembled using NEBuilder HiFi DNA Assembly, and mu-

tations were performed with the Q5 Site-Directed Mutagenesis Kit. Cells were transfected 4 days prior to recording, using Lipofectamine 2000. Cells were replated on sterile coverslips 2 days before recording. Recordings were made on cells with a confluency of 60-70%.

**Calcium Imaging** Cells were first incubated with 2 M Fluo-4 AM in culture media for 30 minutes, and rinsed in DMEM only for 10 minutes. The coverslip with the cells is then transferred to the recording chamber, covered with iECB (imaging Extra Cellular Buffer in mM: NaCl 119, KCl 5, Hepes 10, CaCl2 2, MgCl2 1; pH 7.2; 320mOsm). The cells are equilibrated at room temperature for 5 minutes before start of recording and then imaged on a Nikon Eclipse inverted microscope with a 20X objective (Nikon S Fluor, N.A.= 0.75; W.D.= 1 mm). For fluorescence excitation, an LED with a center wavelength of 470 nm was used for detecting Fluo-4 present in all cells and 560 nm to detect mCherry on transfected cells. For Fluo-4, LED output intensity was set to 160 mW, and filtered to 3% transmittance with ND filters. Images were collected with a Zyla sCMOS Camera (Andor) through a GFP Filter Cube Set (Nikon) and analyzed with Matlab.

**Magnetic stimulation** The magnetic stimulation was delivered by a 1" x 1" cylindrical neodymium rare earth permanent magnet on a computer-controlled translation stage. Black felt was used to cover the magnet as well as sample to avoid artifacts due to reflection of light from the magnet. Prior to magnetic stimulation, baseline fluorescnece data was collected for 30 seconds. After the initial 30 seconds, the magnet was brought within approximately 8 mm of the coverslip at a frequency of 0.08 Hz. At that distance, the magnetic field is predicted to be 275 mT based on manufacturer's specifications, and measured in excess of 200 mT with a Gauss meter. The periodic magnetic stimulation was applied for 270 s and the imaging and magnet

movements were synchronized using Axopatch. For each coverslip, a recording was first performed in the absence of magnetic stimulation (No Stim), the microscope was then moved to a different field of view (FOV) for magnetic stimulation (0.08 Hz Stim). This approach ensured that for each experiment, the cells were exposed to the same illumination conditions and exposed only once to the magnetic stimulation protocol. After magnetic stimulation, the coverslip was discarded. The experiments were performed at 23-25°C and recordings occurred within 30 minutes of the cell being removed from the incubator.

**Mechanical and Thermal Stimulation** Mechanical and thermal responses were measured via calcium imaging of cells under constant fluid flow in a microfluidic chamber. For each coverslip, calcium activity was monitored during the perfusion of 320 mOsm iECB at 23 °C for 30 s. 240 mOsm iECB (mechanical stimulation) or heated 320 mOsm iECB (thermal stimulation) were then perfused for 60 s, followed by a return to 320 mOsm iECB at 23 °C for 30 s. For thermal stimulation iECB was heated with an in-line heater to yield a temperature of 40 °C in the recording chamber (measured via thermocouple).

**Image processing and analysis** Calcium data was analyzed using custom algorithms developed in MATLAB. First, transfected cells were identified based on mCherry expression, and regions of interest (ROIs) corresponding to individual transfected cells were automatically selected via our segmentation algorithm. We then calculated the percent change in Fluo-4 fluorescence ($\Delta F/F_0$) for each ROI based on the average fluorescence value divided by the average fluorescence value of the first captured image, $F_0$.

# Chapter 4

# Probing Nanoscale Heat Transfer Using Silicon Photonic Thermometry

In Chapter 2, we have seen evidence for local nanoscale heating effects that are not expected from bulk thermal properties. This local heating is essential not only for magnetic neuromodulation, but also for remote and localized triggering of drug release [70], [71], [72], and hyperthermia for killing cancer cells without affecting healthy cells in the vicinity [73], [74]. Several studies have shown evidence that local heating in the close vicinity of the nanoparticles can trigger cellular responses [14], [16], [32] or release of drugs [33], even in the absence of significant changes in the temperature of the targeted area. For instance, Creixell et al. showed that local heating of nanoparticles attached to cancer cells triggered apoptosis in the absence of global heating [32]. Huang et al. activated temperature sensitive ion channel TRPV1 by local heating of nanoparticles attached to the cell4. They monitored the temperature around the nanoparticle using emission intensity from DyLight549 and the bulk temperature using yellow fluorescent protein present in the solution. While the nanoparticle surface temperature increased in the presence of magnetic field, the bulk solution remained at constant temperature [14].To explain the anomalous temperature gradients at the surface of nanoparticles, a water shell model was proposed where the thermal conductance of the water in the close vicinity of nanoparticle is lowered by 10-13 orders of magnitude. In this chapter, I describe the results of our novel method of measuring temperature near the surface of iron oxide nanoparticles using silicon photonic

thermometry. Using this method, we show that the temperature at the vicinity of nanoparticles is indeed higher than expected from classical laws. We also determine the value of $g^*$ using the kinetics of temperature change near the surface.

## 4.1 Silicon Photonic Thermometry

To more directly determine the temperature near the surface of magnetic nanoparticles using a technique that is not affected by magnetic field effects, we use silicon photonic thermometry. Because most optical materials including silicon have negligible magneto-optic cofficients and is not heated by alternating magnetic fields, an optical thermosensor is immune to artifacts due to high frequency alternating magnetic fields. In fact, fiber optic thermometers are already widely used to measure temperature of nanoparticle suspensions subjected to magnetic fields because they are not affected by electromagnetic interference [16]. However, fiber optic thermometers lack the spatial resolution to investigate the temperature near the surface of nanoparticles. Here we use a temperature sensor based on a silicon microring resonator to measure local temperature changes produced near nanoparticles during radio-frequency (RF) magnetic field heating. The principle behind our temperature sensor is that small changes in the temperature of the microring resonator, which acts as an optical resonant cavity, will alter the refractive index and thus shift the resonant wavelength (Fig 4.1). By measuring this resonant wavelength, we can thus infer the temperature of the resonant cavity. These microring resonator devices are excellent optical thermosensors giving high sensitivity due to the large thermo-optic coefficient of Silicon ($1.6 \times 10^{-4}\ ^{\circ}C^{-1}$) [75], as well as fast temporal response on the order of a few $\mu$s [75]. To probe nanoscale heat transfer, nanoparticles are attached to the surface of a ring resonator and water is placed over them. The chemical functionalization ensures

that the attached nanoparticles are within a few nm of the photonic thermosensor, which allows for measurement of temperature close to the surface of the nanoparticle by the resonator. A fiber optic thermometer is used to simultaneously measure the temperature of a drop of water placed over the silicon surface. Using this all-optical set up, we find that temperature at the surface of nanoparticles is indeed greater than that in the water. Furthermore, we use the temperature profiles obtained from the thermosensors and estimate the value of $g^*$ to be indeed close to $10^{-13}$.

A microring resonator device consists of a ring that is laterally coupled to a waveguide. Light is coupled in and out of the device via a grating coupler attached to either side of the waveguide. Resonance occurs when the wavelength is an integral multiple of the path length of the ring:

$$m.\frac{\lambda}{n_{eff}} = L \tag{4.1}$$

where, $\lambda$ is the free-space wavelength at resonance condition, $m$ is an integer, $n_{eff}$ is the effective refractive index of waveguide mode and $L$ is the path length of the ring. On resonance, the transmission through the waveguide is minimized as light gets trapped in the ring due to constructive interference [76]. When the temperature changes, the effective refractive index of silicon changes due to the high thermo-optic coefficient of Silicon ($1.86 \times 10^{-4}$ °C$^{-1}$) [75]. This leads to a shift in the resonance wavelength of the ring resonator, which can be precisely determined. When nanoparticles are heated in a magnetic field, the temperature change at their surface can be determined using the optical read out in the form of resonance wavelength shift (Fig 4.1).

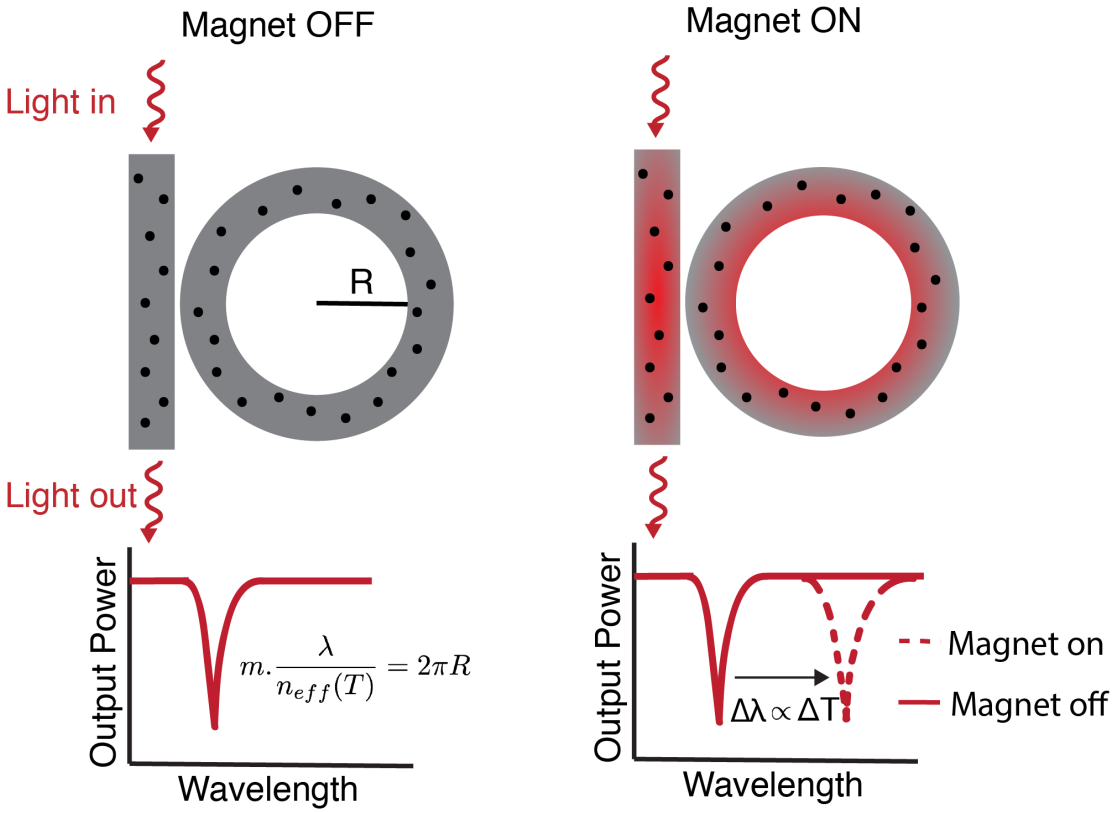


Figure 4.1 : Temperature sensing using silicon ring resonator device. (Left) Light from a tunable laser is coupled into the waveguide and the transmission spectrum (output power) is collected. A dip in the transmission spectrum is seen at resonance condition when the path length of the ring ($2\pi R$) is an integral multiple ($m$) of the wavelength ($\lambda/n_{eff}$). Increasing the temperature of the ring changes the temperature dependent refractive index ($n_{eff}$) and therefore shifts the resonance wavelength, and this shift can be used as an optical read-out of temperature change. In this experiment, we attach magnetic nanoparticles to the ring resonator and the temperature change near the surface of the nanoparticles subjected to a magnetic field can be measured using the resonance shift from the device.

## 4.2 Device Fabrication and Characterization

We fabricated the silicon microring resonator devices using standard MEMS fabrication techniques on a 100-mm SOI wafer, having a top silicon layer thickness of 250 nm (Ultrasil Corporation). This top layer constitutes the structural layer for the ring resonators. First, we patterned the photonic circuitry using an electron beam lithography system (JBX-5500, JEOL Inc.) in XR1541-006 negative electron-beam resist (Dow Corning Corp.). The pattern is then transferred into the Si layer by using reactive ion etching (ICP-RIE, Oxford Instruments). The residual e-beam resist is stripped by a quick hydrofluoric acid (HF) dip. Figure 1b shows a schematic representation of a photonic device consisting of microring, waveguide and grating coupler. Light is coupled in and out of the waveguide through the grating coupler. Scanning electron micrographs (Figure 4.2 (b) and (c)) show the fabricated silicon ring of radius 20 $\mu$m and the grating coupler. About 10-20 of these rings with their waveguides and grating couplers are present on each device chip of dimensions $\approx 1$ cm $\times$ 1 cm.

We use a right angle $\mu$-prism with aluminum coatings for optical coupling and assembly packaging, which improves the mechanical durability compared to vertical fiber attachment. The cross section of the prism is 180 $\times$ 180 $\mu$m$^2$. First, the bare polished optical fiber is attached to a -prism at an angle of 5 degrees by using UV curable epoxy (Norland Optical Adhesive 85), which represents the coupling angle of the grating couplers. Then the fiber-prism is aligned to the input grating coupler to achieve effective coupling through the reflection of the prism, which is followed by securing the optical fiber to the device by applying additional UV epoxy. To measure the resonance wavelengths, we use a single-mode tunable laser (Ando AQ4321D) that spans a wavelength range of 1520-1620 nm. The transmission light is collected by

a photodetector (Multi-Function Optical Meter 1835-C, Newport) and plotted as a function of wavelength. To determine this resonance wavelength, we fit a Lorentzian curve to the transmission spectrum. Figure 4.2 (d) shows two resonant wavelengths near 1552 nm and 1557 nm. The FWHM of the transmission curve is evaluated to be as low as 0.035 nm, giving a high Q-factor ($= \frac{\lambda}{FWHM}$) of 45,000, ideal for sensing temperature changes with high resolution. The temperature dependence of resonant wavelength of the fabricated device was evaluated by mounting the device on a Peltier thermo-electric heater (Adafruit) whose temperature is set by adjusting the voltage applied to it. The temperature is changed from 25  37 degrees C and the corresponding resonant wavelengths are measured and plotted in Figure 4.2 (e). The slope of the linear fit to this data shows a temperature sensitivity of 61.54 pm/°C. This allows us to sense temperature changes as low as 0.5 °C.

## 4.3 Attaching nanoparticles to device

For our experiment we used magnetite nanoparticles (Ocean Nanotech) with an average diameter of 13.5 nm as determined by TEM (Figure 4.3 (a) and (b)). We attached these particles to the surface of the silicon photonic chip in two steps (as seen in Figure 4.3 (c)): In the first step, we aminated the surface by aminosilanization using (3-Aminopropyl) triethoxysilane (APTES). In the second step, we used EDC-NHS crosslinking chemistry to attach carboxyl coated iron oxide nanoparticles via a covalent bond that is formed to the amine groups on the surface of the photonic device.

We performed aminosilanization using a previously reported procedure for aminating glass substrates29. Specifically, we cleaned the surface of the silicon in methanol solution for 5 minutes and then incubated it in a reaction mixture consisting of 100

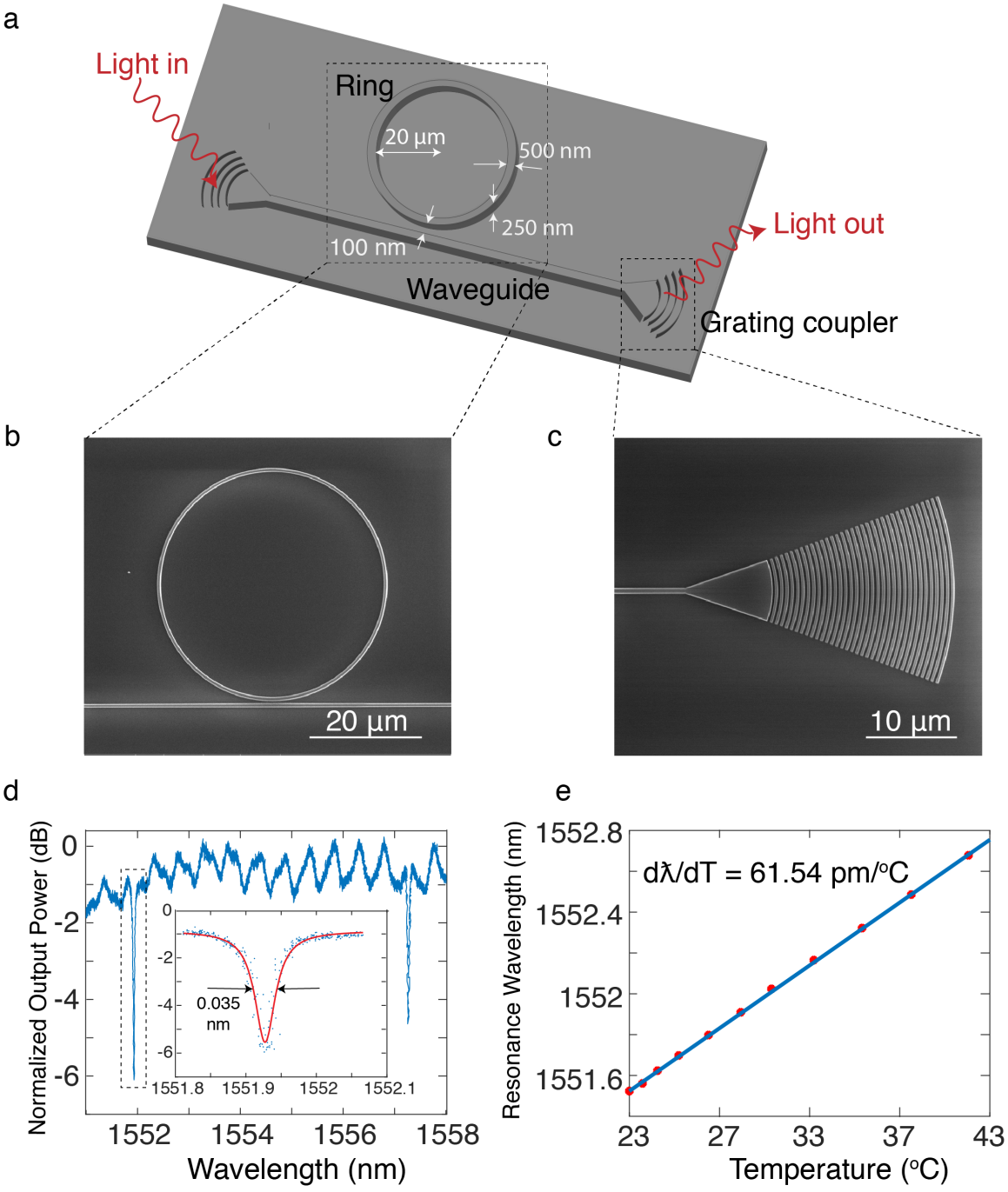


Figure 4.2 : (a) The silicon photonic temperature sensor consists of a ring resonator, a waveguide and two grating couplers. The light is coupled in and out of the device via a prism aligned with the grating coupler. The ring resonator is 20 $\mu$m in radius and is at a 700 nm gap from the waveguide. Figure is not to scale. SEM image of the (b) ring and waveguide, and (c) grating coupler. (d) Optical spectral response of the silicon resonator: Two resonant wavelengths are seen as dips in the transmission near 1552 (Inset) and 1557 nm. Lorentzian fit to the resonance near 1552 nm shows an FWHM of 0.035 nm resulting in a high value of Q-factor ($= \frac{\lambda}{FWHM} = 45{,}000$). (e) The rings resonance wavelength increases 61.54 pm per °C rise in temperature.

ml methanol, 8 ml acetic acid and 3 ml APTES (Sigma Aldrich) at room temperature with gentle mixing for 25 minutes. Sonicate for 1 minute at a point halfway into the incubation. Rinse again in methanol solution with shaking for 5 minutes and blow dry.

We then attached carboxyl coated iron oxide nanoparticles (Ocean Nanotech) to the surface amine groups using the conjugation kit provided by the same company. Briefly, we added a solution consisting of 2 mg/ml EDC and 1 mg/ml NHS in activation (low pH) buffer to a 1 mg/ml solution of nanoparticles in a 1:2 ratio and mixed thoroughly. After 20 minutes of incubation with shaking, we dropped the activated nanoparticles solution dropped onto the surface of the device and left to incubate overnight while ensuring the solution doesnt dry. The device is then cleaned using DI water and blow-dried.

This protocol gives uniform, covalent, monodisperse attachment of nanoparticles to the surface of the device as seen from SEM and AFM images (Figure 4.3 (d) and (e)). Note that the nanoparticles attach to the top of the entire device chip and not selectively to the ring and waveguide.

## 4.4 Nanoparticle heating in AMF

To measure the heat transfer between nanoparticles and bulk water (and in turn the thermal conductance between them), we placed a 100 $\mu$l drop of water on top of the silicon chip consisting of the microring and waveguide (of total size $\approx 1$ cm$^2$) with the attached nanoparticles. This configuration is then placed inside a styrofoam enclosure that fits inside 50 mm diameter coils of an RF magnetic field generator (Magnetherm AC system, Nanotherics Corp.), which is used to generate high frequency alternating magnetic fields (as shown in Figure 4.4 (a)). We measured the temperature of the

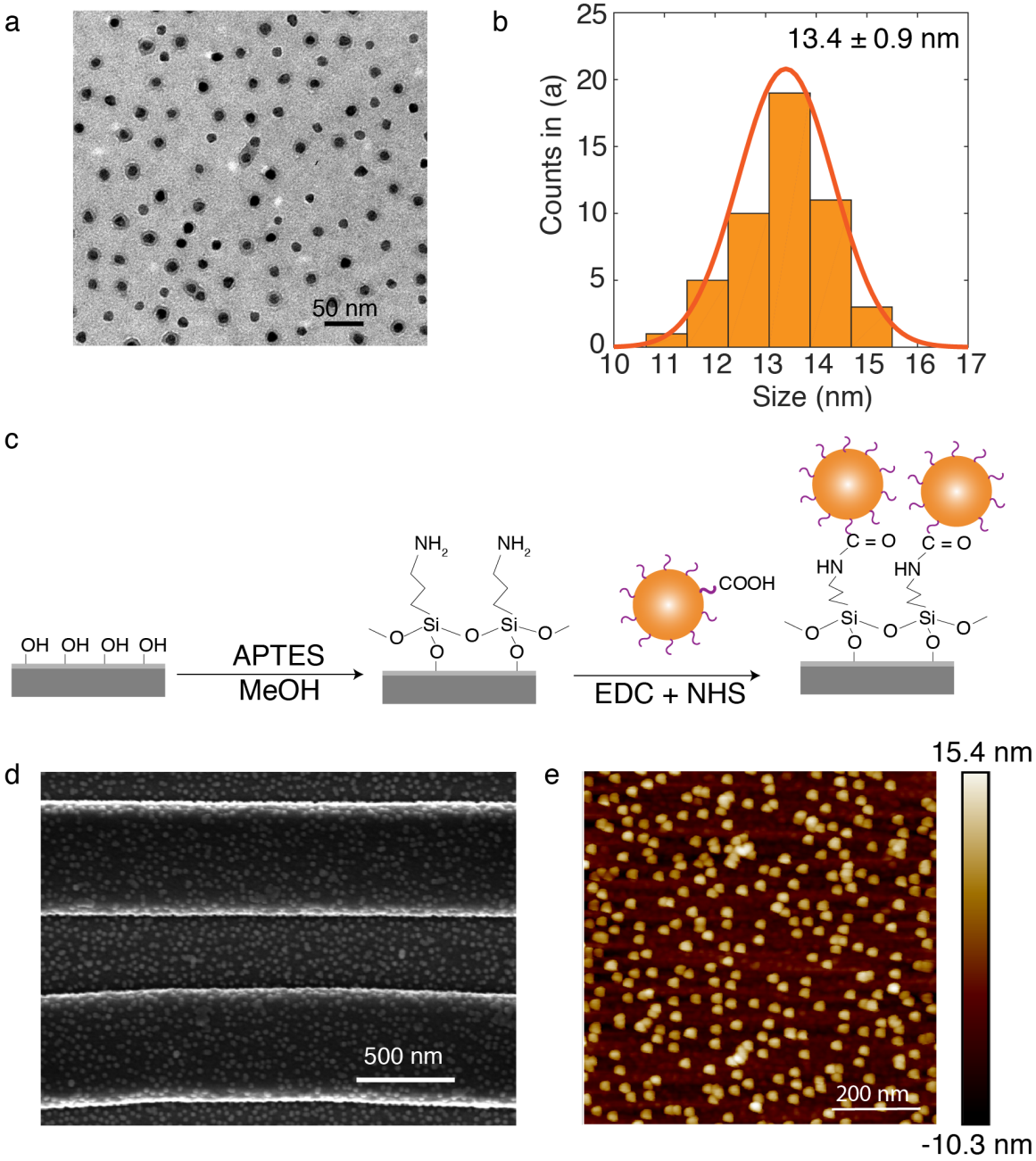


Figure 4.3 : (a) TEM analysis of nanoparticle sample. (b) The core size distribution was obtained from the measurement of 50 cores from TEM image in (a). Size distribution was fitted with a normal function (solid line) and shows a mean size of 13.4 nm. (c) Chemistry of nanoparticle attachment to the device. The oxidized surface of the silicon photonic device is first aminosilanized using APTES to expose amine groups. Carboxyl coated nanoparticles are then attached using the standard EDC-NHS reaction. (d) High resolution SEM images show uniform monodisperse attachment of nanoparticles to the entire device substrate including the ring and the waveguide. (e) AFM images of nanoparticles attached to device substrate. Scale bar on the right represents height.

silicon using the shift in resonance wavelength of the microring as the input wavelength is swept between 1560  1563 nm with a sweep time of 2 seconds and a step time of  0.3 seconds, thereby giving one temperature measurement every $\approx$ 2.3 seconds. We recorded the temperature of water using a fiber optic thermometer (LumaSense Technologies) inserted into the water and sampled at a frequency of 2 Hz. A 6.2 nF capacitor and 3000 W power source generates a magnetic field of 25 mT at 1000 kHz frequency. The experimental configuration which consists of the silicon photonic device chip, nanoparticles and water in the styrofoam encasing is subjected to this magnetic field 600 seconds after the start of recording for a total of 2400 seconds. As a control, we performed the same experiment using a photonic device chip with 100 $\mu$l water on top but with no nanoparticles attached. Temperature change caused in this configuration is due to resistive heating of the coils that results from the electric current needed to generate the magnetic field.

Representative traces of the temperature profile of the device and water from both the with-particles and without-particles cases are shown in Figure 4.4 (b) and (c). The effect of the coil heating results in a 2 °C rise in temperature of both the device and the water as seen in the without-particles case. The temperature change of the device and water in the with-particles case is significantly greater ($>$ 8 °C) than in the control case indicating that the majority of the temperature change is the result of heat generated via relaxation losses in the magnetic nanoparticles. Replicates of the 'with-particles' experiment are shown in Figure 4.5. The temperature change observed in the with-particles is significantly larger than without particles suggesting that the overserved temperature increase is due to both the nanoparticles as well as coil heating (with the nanoparticles accounting for the majority of the temperature increase). We repeated the without-particles experiment and found less than 9%

difference in steady state values (Figure 4.6), suggesting that the effect of the coil on the change in temperature was relatively constant for each experiment. Based on these data we chose to remove the coil heating component by subtracting the average of our four without-particle controls from each with-particles experiment (Figure 4.7).

When the magnet is turned on, the temperature of the silicon with nanoparticles attached rises faster than that of water. Most interestingly, the temperature change of the silicon is significantly greater than that of water, which indicates a significant thermal gradient. At saturation, this difference is over 2 °C, clearly indicating that the silicon is being heated directly by the nanoparticles rather than by the heated water. More importantly, because the nanoparticles are the primary heat source, the silicon temperature can be higher than the water only if the nanoparticle temperature is also significantly higher than the water. Thus, it is clear that there is a thermal gradient of at least 2 °C between the nanoparticles and water bath, which is contrary to expectations from classical laws as seen in Eq. 2.7. We also note that with the time resolved measurement of the silicon temperature we can estimate the thermal conductance at the interface of nanoparticles and water and in turn, the value of $g^*$. The value of $g^*$ is obtained using a model for heat transfer between the nanoparticles and the bulk water through the water shell. The parameters of this model are optimized to match the experimentally observed temperature rising curve. Since the temperature profile shown in Figure 4.4 (b) (with-particles case) is due to both the nanoparticles as well as coil heating, we subtract the temperature profile measured due to the coil heating (the without-particles condition) to isolate the effect of the nanoparticles. We expect that this subtraction effectively removes the contribution of the coil heating because the shape and magnitude of the temperature rise profile obtained from the control (without-particles) condition is consistent across all replicates

of the measurement (Figure 4.6). To account for slight differences in the sampling time and rate for our experiments we fit the rising temperature curves to a double exponential for both the with particles experiment and without particles control. We then subtracted the fitted control curve from the fitted experiment curve to remove the effect of the coil heating before optimizing for the values in our equivalent circuit model. The corrected data following the subtraction of the control experiments is shown in Figure 4.8 (b) and (c) as well as in Figure 4.7.

To estimate the heat transfer between nanoparticles (N), silicon (S), water (W) and bath (B), we model the system using an equivalent circuit for heat transport shown in Figure 4.8 (a), in which current, voltage, capacitance, and electrical conductance represent thermal power, temperature, heat capacity, and thermal conductance respectively [77]. In this circuit, the values of the thermal conductances between nanoparticle and bulk water ($G_{NW}$) through the water shell and between nanoparticles and silicon ($G_{NS}$) are unknown. By evaluating $G_{NW}$, we estimate the value of $g^*$. The rest of the values for heat capacities ($C_N$, $C_S$, $C_W$), macroscopic thermal conductances ($G_{SW}$, $G_{WB}$) and power ($I$) value can be estimated based on known characteristics of the system. The heat capacities ($C_N$, $C_S$, $C_W$) are calculated by multiplying known values of the specific heat capacities of magnetite, silicon and water by their corresponding masses. Note that we estimate the total mass of all the nanoparticles by counting the total number of particles attached to the surface of the silicon as observed in SEM images (Figure 4.3 (d)) and known volume of each particle. The macroscopic thermal conductances ($G_{SW}$, $G_{WB}$) are evaluated from the thermal decay rates of silicon and water. These values are evaluated in Section 4.4.1 and tabulated in Table 2 in Figure 4.9. The value of the power generated ($I$) by the nanoparticles is determined using the theoretically calculated value of Specific Loss

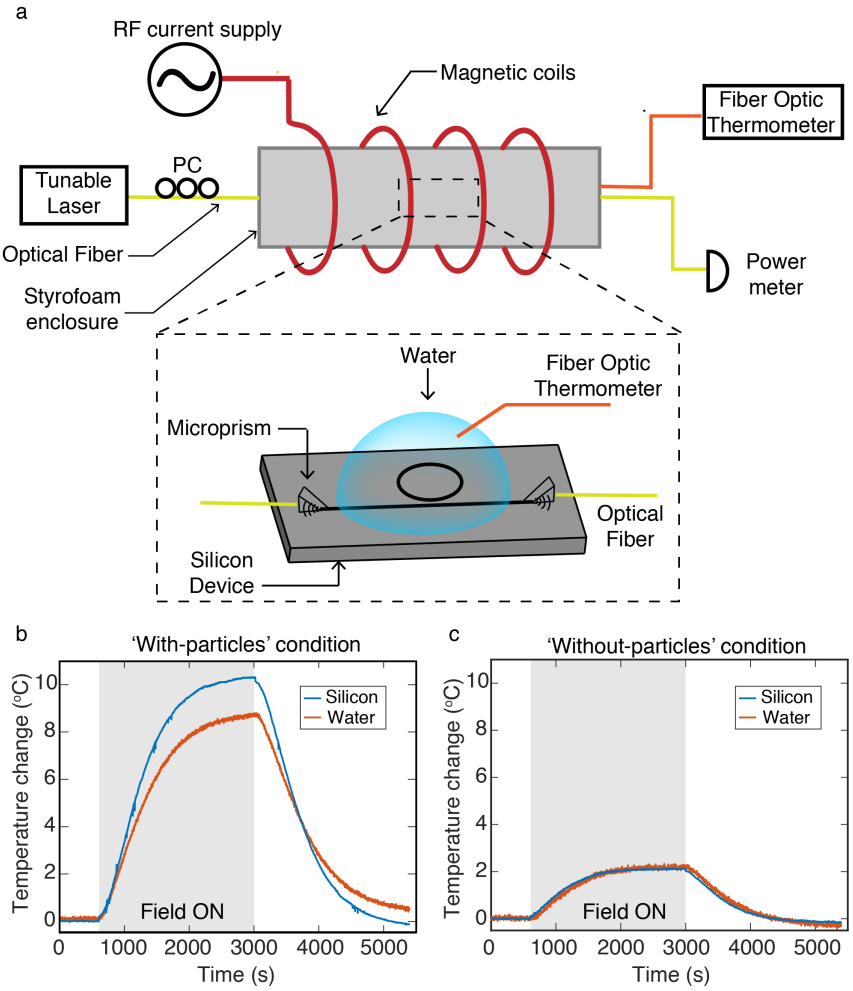


Figure 4.4 : ((a) The experimental set up consist of the ring resonator device approximately 1 cm $\times$ 1 cm in size (with or without nanoparticles attached) and 100 $\mu$l water placed inside an insulating styrofoam enclosure placed within the coils of a high frequency magnetic field generator. Fiber optic cables (shown in yellow) carry infrared light from a tunable laser through a polarization controller (PC) into the enclosure to couple to the microring resonator. Similarly another set of optical cables carry the out-coupled light from the device to a power meter placed outside the enclosure to collect the transmission spectra. Effective light coupling between the optical fiber and the waveguide is ensured by attaching the fiber to microprism, which in turn is aligned to the grating coupler. A fiber-optic thermometer (shown in orange) is used to measure the temperature of the water. (b) Temperature profile of the silicon with nanoparticles attached and water obtained from the resonance wavelength shift read-out and the fiber optic thermometer respectively. A magnetic field of 25 mT at 1000 kHz is applied for 2400 s after 600 s from start of recording. (c) Temperature profile measured in the same conditions from silicon that has no attached nanoparticles; and water. The increase in temperature seen in (c) is due to coil heating. The temperature increase in (b) is significantly different from that in (c) indicating that the source of heating is predominantly nanoparticles.

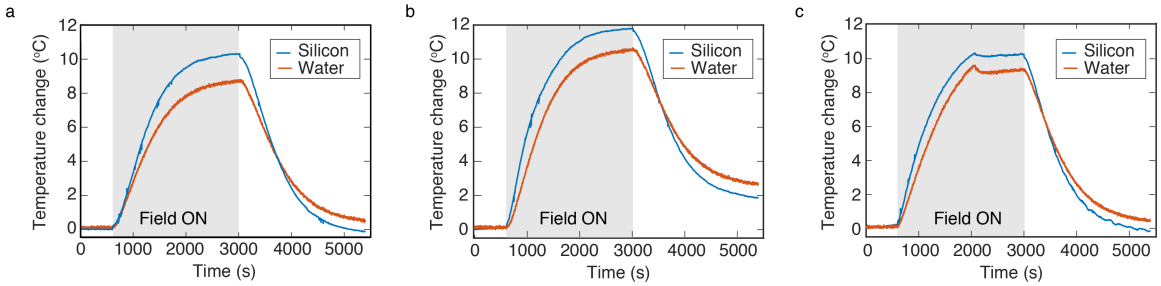


Figure 4.5 : Replicates of temperature measurements from silicon and water with nanoparticles attached under the application of magnetic field show similar temperature profiles. The curves in (a) are the same as those in Figure 4.4 (b). All three experiments measure higher temperature for silicon compared to that of the water, indicating a steep temperature gradient ($> 1$ °C) between the nanoparticles and the solution around it, contrary to expectations from classical heat transfer laws.

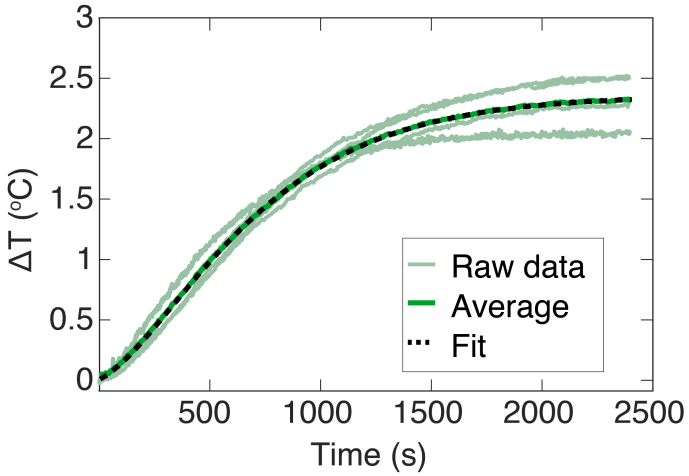


Figure 4.6 : Repeated measurements of temperature of the silicon device measured in the presence of an alternating magnetic field (with no nanoparticles attached) show similar temperature rise profile resulting from coil heating, with a less than 9% difference in steady state values. The average of all the curves (shown in dark green) are fit to a double exponential curve (black dotted curve). The fitted curve is then subtracted from all of the temperature measurements from silicon under the with-particles condition.

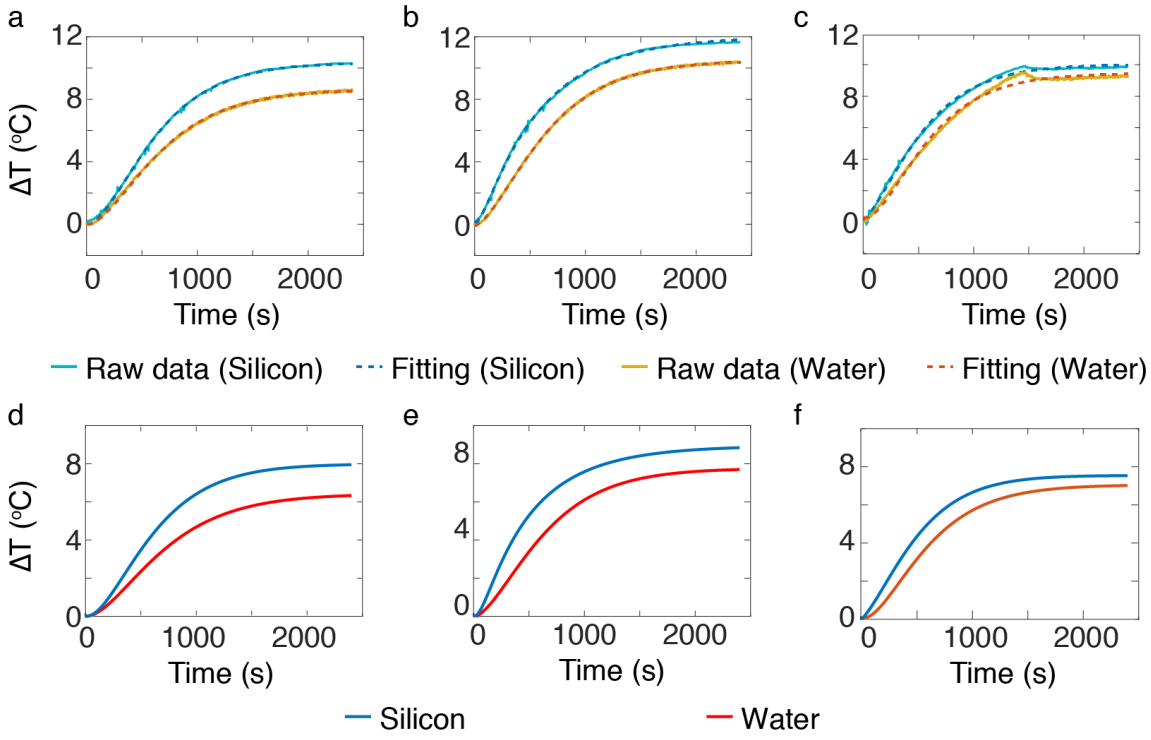


Figure 4.7 : (a-c) The rising part of the experimentally measured temperature profiles in Figure 4.5 (a-c) are fitted to double exponential curves. (d-f) From the fitted curves in (a-c) for silicon and water, we subtract the average temperature profiles measured due to the coil heating (Figure 4.6) to isolate the effect of the nanoparticles. These corrected curves are used when fitting the values for our heat transfer model shown in Figure 4.8(a).

Power (SLP) due to relaxation losses in magnetite nanoparticles (SI Section 3). The values of $G_{NW}$ and $G_{NS}$ are then estimated by fitting the transient response of the equivalent circuit to the experimentally measured temperatures of both the silicon and water ($T_S$ and $T_W$).

The equivalent circuit in Fig 4.8 (a) can be described by the following system of ordinary differential equations (ODEs) with $G_{NS}$ and $G_{NW}$ as unknown parameters (coefficients):

$$\frac{dT_N}{dt} = \frac{I - G_{NW}(T_N - T_W) - G_{NS}(T_N - T_S}{C_N} \tag{4.2}$$

$$\frac{dT_S}{dt} = \frac{G_{NS}(T_N - T_S) - G_{SW}(T_S - T_W)}{C_S} \tag{4.3}$$

$$\frac{dT_W}{dt} = \frac{G_{NW}(T_N - T_W) + G_{NS}(T_S - T_W) - G_{WB}(T_W - T_B)}{C_W} \tag{4.4}$$

We used MATLAB to simultaneously solve the system of differential equations as well as optimize for the unknown parameters by minimizing the error between the solution of the ODE system and the actual experimental data. To perform this analysis, we first use an ODE solver to solve for the system of ODEs using an initial set of parameter values. We then evaluated an objective function, defined as the squared error between the solutions generated by the ODE solver. We used the particle swarm optimization algorithm to minimize the objective function. The particle swarm algorithm searches a defined parameter space for an optimal solution by moving a set of potential solutions (called particles or agents) around in the search space. The agents are initially defined randomly in the search space. The objective function is evaluated at each of these locations and the best location (corresponding

to lowest function value) is determined. The agents positions are updated based on its local best-known location. Note that for this analysis, the bounds on the values of parameters $C_N$, $C_S$, $C_W$ are set to be within 20% and the bounds for $G_{SW}$ and $G_{WB}$ within 50% of their calculated values (Table 2 in Figure 4.9). The calculated value of power ($I$) is 2  3 times lower than that required to account for the temperature rise observed in our measurements. This discrepancy is likely due to underestimation of the number of particles on the surface of the silicon. However, this error in calculation of the number of particles on the surface changes the value of $g^*$ by less than a factor of or 3, which does not significantly affect our order of magnitude estimate for $g^*$.

We set the parameter space for $G_{NS}$ and $G_{NW}$ to span the range of $g^*$ values from $10^{-16}$ to 1, with 1 corresponding to the case where nanoscale thermal conductance is equal to classical macroscale value. To do this, we first calculate the classically expected value of $G_{NW}$ ($G_{expected}$ in Eq. 2.9) based on the expected value of the thermal conductance of each water shell calculated from classical laws and the known value of thermal conductivity of bulk water and the number of nanoparticles on the surface of the device estimated from the SEM images (See Section 4.4.2). The parameter space for $G_{NW}$ ($G_{actual}$ in Eq. 2.9) is then obtained by multiplying the expected value by the selected range of $g^*$ values. In order to avoid landing into local optima, it is often necessary to restrict the bounds of the search space. Therefore, we evaluated the solution for the values of $G_{NW}$ and $G_{NS}$ by dividing the overall search space into 4 intervals that each span 4 orders of magnitude. Together these intervals cover a range of g* values from $10^{-16}$ to 1. The best fit to the experimental data is obtained in the window corresponding to $10^{-16}$ - $10^{-12}$, at $g^* = 4 \times 10^{-13}$ (See Figure 4.8(c)). Note that the solution reproduces the characteristics of the experimental data including the double exponential form of the rising temperature. The optimal

solutions in the other parameter windows have a much greater error value and do not follow the functional form of the rising temperature (Figure 4.8(c)). Rather these solutions show a fast-rising temperature that resembles a single exponential function. Note also that when $g^*$ approaches 1, the model shows no temperature difference between the silicon microring and water as predicted by classical thermal transport laws, and not observed in our data. The exact values of all fitted parameters are tabulated in Table 3 and 4 in Section 4.4.2.

### 4.4.1 Calculating the values of elements in Equivalent Circuit Model

The total heat capacities of silicon and water elements of the equivalent circuit are calculated based on the specific heat capacities and masses of the silicon and water respectively as: Total Heat Capacities=Mass $\times$ Specific Heat Capacity. The masses of the silicon and water are 0.154 g and 0.1 g (100 $\mu$l) and their specific heats are 0.7 J $g^{-1}$ $K^{-1}$ and 4.18 J $g^{-1}$ $K^{-1}$. We therefore get total heat capacities of 0.1078 J $K^{-1}$ and 0.418 J $K^{-1}$ respectively for $C_S$ and $C_W$.

The number of particles on the device (and in turn, the heat produced by them and their heat capacity) is estimated based on counting the number of particles in a given area in SEM images (Figure 4.3 (d)) and the total area of the device. This amounts to about $5 \times 10^{10}$ particles on the device. Given the molar heat capacity of magnetite (= 150 J $mol^{-1}$ $K^{-1}$), molecular weight (233 g/mol) and density (5.17 g/cc) we can estimate $C_N$ for $5 \times 10^{10}$ particles of size 13.5 nm particle to be: $C_N$ = (Molar Heat Capacity)/(Molecular Weight) $\times$ Density $\times$ Volume of particle $\times$ No.of particles = $8.6 \times 10^{-8}$ J/K.

The macroscopic thermal conductances between silicon and water and water and bath are estimated using the rate at which they dissipate heat: Thermal Conduc-

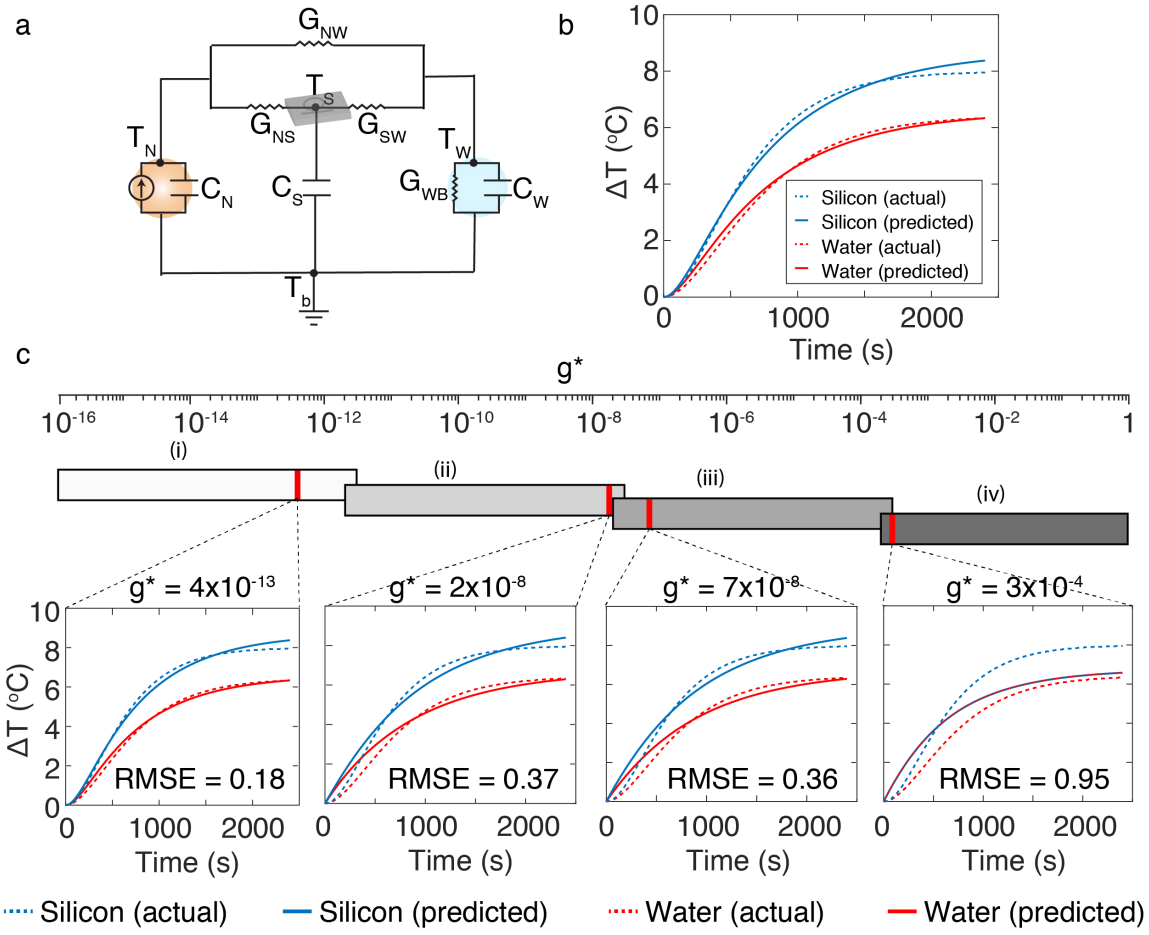


Figure 4.8 : (a) Equivalent circuit model used to estimate heat transfer between the nanoparticles (N), silicon (S) and water (W). $T_N$, $T_D$, $T_W$, $T_B$ represent the temperature of the nanoparticles, silicon, water and bath, respectively. $C_N$, $C_D$ and $C_W$ represent the heat capacities of the nanoparticles, silicon and water respectively. $G_{NW}$, $G_{ND}$, $G_{DW}$ and $G_{WB}$ represent the thermal conductances between the nanoparticles and water, nanoparticles and silicon, silicon and water, and water and bath respectively. (b) The best fit to our data occurs when $g^* = 10^{-13}$. For this value, the temperature dynamics of the model (solid lines) agrees closely with the experimental temperature measurements of both the silicon and water (dashed lines). (c) The optimal value of $g^*$ is obtained by searching the $g^*$ space from $10^{-16}$ to 1 using sliding windows ranging 4 orders of magnitude each. The optimal solutions are shown for each window, and the corresponding g* value is indicated in red. The solution that best fits the experimental curves (dashed lines) is obtained at $g^* = 10^{-13}$ (Window (i), same as in (b)) as can be seen both from the low value of root mean squared error as well as from conformation to the shape of the curves. The optimal solutions in the other windows ((ii), (iii) and (iv)) show large deviations (errors) from the experimentally observed curves. As $g^*$ approaches 1 (as in Window (iii)), the model gives similar temperature profiles for both silicon and water contrary to what is seen experimentally.

tance=Heat dissipation rate × Total Heat Capacity. To find the heat dissipation rate, the device with 100 $\mu$l water on the top is placed in an oven and heated. Temperature of the device and water are measured using a thermocouple and fiber optic thermometer respectively as soon as the configuration is removed from the oven. An exponential decay curve is fit to the data, from which we obtained the rate constant of heat dissipation from the device to water and from water to bath to be 0.003 $s^{-1}$. Therefore, $G_{SW}$= 0.003 × 0.1078=0.0003 W/K and $G_{WB}$= 0.003 × 0.418=0.0012 W/K

The theoretical value of the power generated per gram of nanoparticles (Specific loss power) via relaxation losses in a magnetic is determined using [78] :

$$SLP = \frac{P}{\rho\phi} \tag{4.5}$$

where $\rho$ is the density of magnetite and $\phi$ is the nanoparticle volume fraction. $P$ is given as [79]

$$P = \pi\mu_0\chi_0 H^2 f \frac{2\pi f\tau}{1+(2\pi f\tau)^2} \tag{4.6}$$

where $\mu_0$ is the magnetic permeability, H is the magnitude of applied field, f is the frequency of the field, $\chi_0$ is the nanoparticle susceptibility and $\tau$ is the effective relaxation time of the particle. $\tau$ is given by:

$$\frac{1}{\tau} = \frac{1}{\tau_B} + \frac{1}{\tau_N} \tag{4.7}$$

$\tau_B$ is the Brownian relaxation time given as:

$$\tau_B = \frac{(3\eta V_H)}{kT} \tag{4.8}$$

where $\eta$ is the viscosity coefficient of the nanoparticle solution medium and VH is the hydrodynamic volume of the nanoparticle.

$\tau_N$ is the Nel relaxation time given as

$$\tau_N = \tau_0 exp(\frac{KV}{kT}) \tag{4.9}$$

where $\tau_0$ is the attempt time (typically $10^{-9}$ s), $K$ is the anisotropy constant and $V$ is the core volume of the nanoparticle.

The susceptibility is in turn a function of magnetic field. To obtain a conservative estimate for lower bound of P, a Langevin Equation is used to describe $\chi_0$ as follows:

$$\chi_0 = \chi_i \frac{3}{\xi}(coth\xi - \frac{1}{\xi}) \tag{4.10}$$

where $\chi_i$ is the initial susceptibility given by

$$\chi_i = \frac{(\mu_0 \phi M_d^2 V)}{3kT} \tag{4.11}$$

and

$$\xi = \frac{(\mu_0 M_d H V)}{kT} \tag{4.12}$$

The values of the variables used in the calculation are as follows:

$\mu_0$ = magnetic permeability = $4\pi \times 10^{-7}$ T m $A^{-1}$

$f$ = frequency of applied field = 1000 kHz

$H$ = magnitude of magnetic field = 20 kA $m^{-1}$

$\phi$ = Nanoparticle volume fraction = 0.13%

$\rho$ = Density of magnetite ($5.17 \times 10^3$ kg $m^{-3}$)

$M_d$ = domain magnetization of nanoparticles ($6.36 \times 10^5$ $Am^{-1}$)

$V$ = nanoparticle volume = (4/3) $\pi$ $r^3$ = (4/3) $\pi$ $(6.75 \times 10^{-9})^3 = 1.3 \times 10^{-24}$ $m^3$ ($r$ = core size/2 where core size = 13.5 nm)

$V_h$ = hydrodynamic volume of nanoparticle = $2 \times 10^{-24}$ $m^3$ (2 nm diameter increase to core size)

$K$ = magnetic anisotropy of magnetite = 13 kJ $m^{-3}$

$\eta$ = Viscosity of water = 894 $\mu$Pa s

$k$ = Boltzman constant = $1.38 \times 10^{-23}$ J $K^{-1}$

$T$ = Temperature = 298 K

This calculation gives SLP = 4000 W/g.

For the $5 \times 10^{10}$ particles present on the device, the power generated ($I$) can be calculated using:

$I$ = SLP (in W/g)$\times\rho$ (in g/cc) $\times$ $V$ (in cc) $\times$ $5 \times 10^{10}$

giving $I$ = 0.0015 W.

The values of the elements of the Equivalent circuit in Fig 5 (a) are listed in Table 2 in Fig 4.9.

**Table 2**: Calculated values of known parameters in the equivalent circuit model of the experimental measurement set-up and the upper and lower bound values of those parameters used in optimization.

| Parameter | Calculated Value | Lower bound | Upper bound |
|---|---|---|---|
| $C_W$ | 0.418 J $K^{-1}$ | 0.3 J $K^{-1}$ (~ -25%) | 0.5 J $K^{-1}$ (~ +20%) |
| $C_S$ | 0.1078 J $K^{-1}$ | 0.086 J $K^{-1}$ (~ -20%) | 0.13 J $K^{-1}$ (~ +20%) |
| $C_N$ | 2.4 x $10^{-7}$ J $K^{-1}$ | 1.8 x $10^{-7}$ J $K^{-1}$ (-25%) | 3 x $10^{-7}$ J $K^{-1}$ (+25%) |
| $G_{SW}$ | 3.2 x $10^{-4}$ W $K^{-1}$ | 1.5 x $10^{-4}$ W $K^{-1}$ (~ -50%) | 5 x $10^{-4}$ W $K^{-1}$ (~ +50%)* |
| $G_{WB}$ | 12 x $10^{-4}$ W $K^{-1}$ | 6 x $10^{-4}$ W $K^{-1}$ (-50%) | 18 x $10^{-4}$ W $K^{-1}$ (+50%) |
| $I$ | 0.0015 W | 0.003 W (2 x) | 0.0055 W (3.5 x) |

*With the exception of the analyses for the temperature profiles in Figure 4.7 (e-f) where the upper bound is 0.001 W $K^{-1}$.

Figure 4.9 : Calculated values of known elements in the equivalent circuit model of the experimental measurement set-up in Figure 4.8(a) and the upper and lower bound values of those parameters used in optimization.

### 4.4.2 Parameter fitting

The optimal values of the thermal conductance between nanoparticles and the surrounding water solution ($G_{NW}$) obtained from optimization algorithm for all the curves in Figure 4.7 are tabulated in Table 3. The corresponding value of $g^*$ is determined by dividing the optimized value of $G_{NW}$ from experiments by the expected value from classical laws ($G_{expected}$ in Eq. 2.9 or $G_{shell}$ in Eq. 2.11) which, for the 5 $\times$ $10^{10}$ particles on the silicon surface, is calculated to be 4000 W K$^{-1}$.

$$g^* = \frac{G_{NW}}{G_{expected}} \tag{4.13}$$

where $G_{expected}$ = 4000 W K$^{-1}$

The optimized values of the other coefficients of the model ($G_{NS}$, $C_N$, $C_W$, $C_S$, $G_{SW}$, $G_{WB}$ and $I$ in the equivalent circuit model) for each data set obtained from the optimization algorithm are shown in Table 4 in Figure 4.10 and the fits are shown in Figure 4.11. The values of the heat capacities and the macroscopic thermal conductances ($C_N$, $C_W$, $C_S$, $G_{SW}$, $G_{WB}$) are within their set bounds shown in Table 2. The value of $I$ deviates by a factor of 2  3.5 from the theoretically expected value, likely due to underestimation of the number of particles on the surface of the silicon. This discrepancy in calculation of the number of particles on the surface changes the value of $g^*$ only by 2 - 3.5 times.

## 4.5 Discussion and Suggested Future Experiments

In this chapter, we have demonstrated a novel method for measuring nanoscale thermal transport in the vicinity of magnetically heated iron oxide nanoparticles using silicon nanophotonic temperature sensor. This approach uses a silicon ring resonator

**Table 3:** Optimal values of $G_{NW}$ and in turn the value of $g^*$ obtained from optimizing the parameters of the equivalent circuit model

| Dataset | Figure 4.8(b) and 4.7(a) | Figure 4.7(b) | Figure 4.7(c) |
|---|---|---|---|
| $G_{NW}$ | 1.5 x $10^{-9}$ W $K^{-1}$ | 2.7 x $10^{-9}$ W $K^{-1}$ | 2.9 x $10^{-9}$ W $K^{-1}$ |
| $g^*$ | 4 x $10^{-13}$ | 6.7 x $10^{-13}$ | 7.2 x $10^{-13}$ |

**Table 4:** Optimized values of the heat capacities and thermal conductances and power in the equivalent circuit model.

| Dataset | Figure 4.8(b) and 4.7(a) | Figure 4.7(b) | Figure 4.7(c) |
|---|---|---|---|
| $G_{NS}$ | 5.6 x $10^{-10}$ W $K^{-1}$ | 1.3 x $10^{-9}$ W $K^{-1}$ | 6.5 x $10^{-10}$ W $K^{-1}$ |
| $C_W$ | 0.3 J $K^{-1}$ | 0.3 J $K^{-1}$ | 0.3 J $K^{-1}$ |
| $C_S$ | 0.86 J $K^{-1}$ | 0.086 J $K^{-1}$ | 0.86 J $K^{-1}$ |
| $C_N$ | 2.9 x $10^{-7}$ J $K^{-1}$ | 3 x $10^{-7}$ J $K^{-1}$ | 3 x $10^{-7}$ J $K^{-1}$ |
| $G_{SW}$ | 0.0005 W $K^{-1}$ | 0.001 W $K^{-1}$ | 0.001 W $K^{-1}$ |
| $G_{WB}$ | 0.0006 W $K^{-1}$ | 0.0007 W $K^{-1}$ | 0.0007 W $K^{-1}$ |
| $I$ | 0.004 W | 0.0052 W | 0.0053 W |

Figure 4.10 : Table 3: Optimal values of $G_{NW}$ and in turn the value of $g^*$ and Table 4: Optimized values of the heat capacities ($C_N$, $C_W$, $C_S$) and thermal conductances ($G_{NS}$, $G_{SW}$, $G_{WB}$) and power ($I$) obtained from optimizing the parameters of the equivalent circuit model in Figure 4.8(a).

that is not affected by the magnetic field and therefore improves the accuracy of the local temperature measurement during magnetic heating. Because the nanoparticles are directly attached to the ring resonator, this method enables measurement of the temperature near the surface of the particles. Importantly, we observe a significant temperature difference between the nanoparticle surface temperature and the temperature of the aqueous solution which implies a significant thermal gradient between the nanoparticles and the surrounding water. This temperature difference is in stark contrast to classical laws that predict negligible temperature gradient at the nanoparticle-water interface due to rapid heat dissipation. Additionally, time-resolved thermometry using the silicon microring device revealed temperature dynamics during the application of the AC magnetic field. When we optimized our model to match

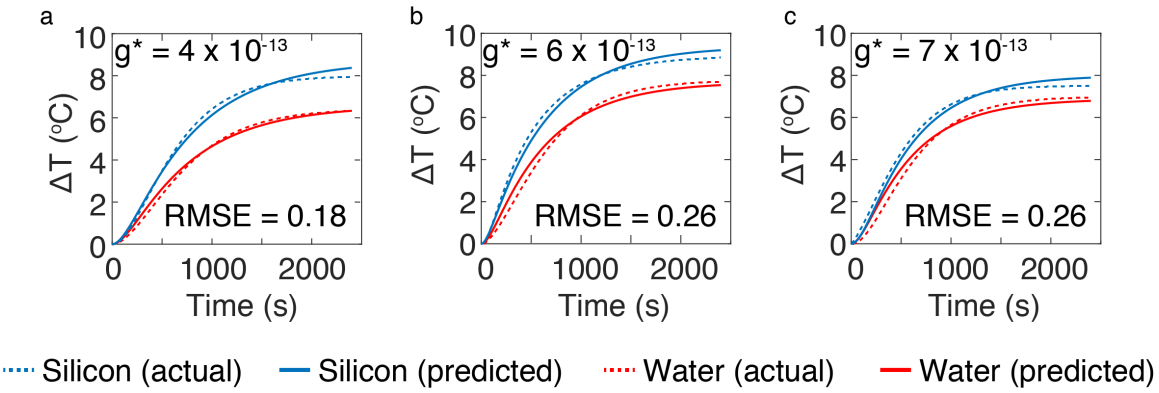


Figure 4.11 : (a-c) The best fits to the data in Figure 4.7(d-f) occurs when $g^* \approx 10^{-13}$. For this value of $g^*$, the temperature dynamics of the model (solid lines) agrees closely with the experimental temperature measurements of both the silicon and water (dashed lines).

the dynamics, we found that the best fit to the experimental data occurred with a thermal conductance at the nanoparticle-water interface that is reduced lowered by a factor of $10^{-13}$. These results support the previous chemical- and fluorescence-based measurements of temperature at the surface of magnetic nanoparticles, which reported significant thermal gradients and $g^*$ values between $10^{-11}$ and $10^{-13}$ [30], [29], [31], [14], [27], [28].

However, further experiments are necessary to validate these results. It has to be noted in particular that the non-zero heat capacity and the resulting thermal mass of the fiber optic thermometer could cause a lag in its temperature reading, which could be falsely perceived as a lag in the temperature of water. Moreover, because the fiber-optic thermometer has a different heat sink compared to the rest of the system in the equivalent circuit in Figure 4.8(a), its temperature equilibrates at a lower value compared to the rest of the system at steady state. This lower temperature could be falsely perceived as a large temperature gradient between the nanoparticles and water due to frustrated thermal conductance at the surface of the

nanoparticle. In order to ensure that our results are not mere artifacts due to the measurement system, a few more control experiments need to be performed. One such experiment would measure the change in temperature of a solution of suspended nanoparticles placed on top of the silicon using both the optical read-out from the silicon microring resonator as well as from a fiber-optic thermometer placed in the solution. In the absence of any artifacts, such an experiment should give similar temperature measurements from both the silicon and the fiber-optic thermometer. Additionally, we could compare the temperature measurements from the nanoparticles in suspension with the nanoparticles attached to the silicon surface by using the same concentration of particles in both cases. If the suspension measurements do not show a notable temperature difference between the measurements from silicon and water, it provides evidence that the temperature measured in the case of nanoparticles attached is indeed from the vicnity of the particles. To avoid any artifacts, we could use a second silicon microring resonator device in place of the fiber-optic thermometer to measure the temperature of water. In this case, only one silicon substrate would have nanoparticles attached to it and the other substrate is in contact only with the water on top of the first silicon substrate. Finally, the effect of the magnetic field on the fiber optic thermometer and the silicon microring resonator have to be independently tested. Furthermore, artifacts due to coil heating could be reduced by using a bigger coil and a thicker insulating enclosure. The same artifact that could potentially result from the thermal mass of the fiber optic thermometer could also be present in the direct real-time temperatures conducted by [27], [28] resulting in a much lower temperature reading from the solution than from the fluorescent particles attached to the nanoparticles. Therefore, it is important to investigate the causes and effects of any fiber optic thermometer artifacts before drawing conclusions about

nanoscale heating phenomena based on these measurements.

While the phenomenological water-shell model is useful for modeling the thermodynamics of the system, more work is needed to identify the physical origin of this frustrated thermal transport. This frustrated thermal transport at the particles surface may in fact not be a property of the surrounding water, but rather other unidentified corrections to classical thermal transport at surface of these nanoparticles. Overall, improved understanding the thermal transport at the surface of these magnetic nanoparticles, informed by measurements of local temperature, would provide opportunities to engineer even more effective magnetothermal applications and therapies.

# Chapter 5

# Evaluating Nanoscale Thermal Conductance from Kinetics of Temperature Change in Nanoparticle Solution

## 5.1 Model for nanoparticle heating in solution

In this chapter, I discuss the effect of lowered thermal conductance on the kinetics of nanoparticle solution heating. For this investigation, I model the heat transfer in the nanoparticle solution system using a simple equivalent circuit shown in Figure 5.1 consisting of 3 elements: nanoparticles (N), water (W) and bath (B). In this circuit, current, voltage, capacitance, and electrical conductance represent thermal power, temperature, heat capacity, and thermal conductance respectively. The heat capacities of the nanoparticles and water can be easily determined using the known values of specific heat capacities and masses of magnetite nanoparticles and water respectively. Similarly the macroscopic thermal conductance between water and bath can easily be determined by measuring the rate at which a similar volume of heated water dissipates and then multiplying it with the heat capacity. These values are tabulated in Table 5 in Figure 5.2 for a 0.5 mg/ml solution of 14 nm magnetite nanoparticles.

The following set of Ordinary Differential Equations (ODEs) represent the dynamic system described by the equivalent circuit model in Fig 5.1:

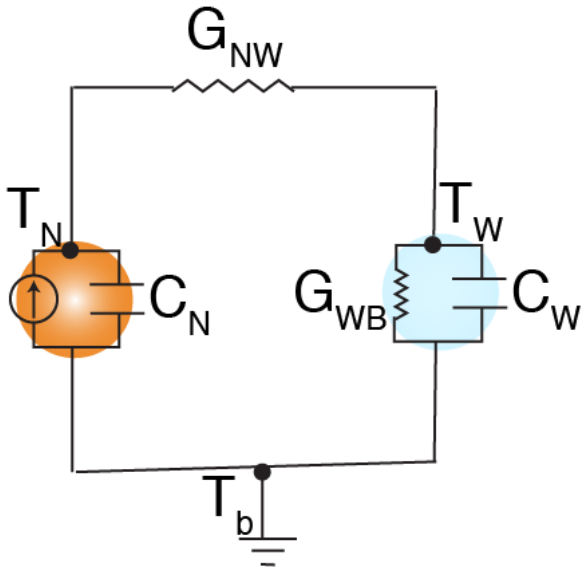


Figure 5.1 : Equivalent circuit model for the heat transfer in the nanoparticle solution system consisting of 3 elements: nanoparticles (N), water (W) and bath (B). In this circuit, current, voltage, capacitance, and electrical conductance represent thermal power, temperature, heat capacity, and thermal conductance respectively.

**Table 5:** Calculated values of the known parameters in the equivalent circuit model of nanoparticles in solution

| **Parameter** | **Value** |
|---|---|
| **$C_N$** | 3.2 x $10^{-4}$ J/K |
| **$C_W$** | 4.18 J/K |
| **$G_{NW}$ (for g* = 1)** | 8.5 x $10^{6}$ W/K |
| **$G_{WB}$** | 0.009 W/K |

Figure 5.2 : Calculated values of $C_N$, $C_W$, $G_{NW}$ and $G_{WB}$ for a 0.5 mg/ml solution of nanoparticles.

$$\frac{dT_N}{dt} = \frac{I - G_{NW}(T_N - T_W)}{C_N} \tag{5.1}$$

$$\frac{dT_W}{dt} = \frac{G_{NW}(T_N - T_W) - G_{WB}(T_W - T_B)}{C_W} \tag{5.2}$$

Note that when $g^* = 1$, $T_N \approx T_W$ and $\frac{G_{NW}}{C_N} \ll \frac{G_{WB}}{C_W}$. This means that the rate of heat transfer between nanoparticles and water ($\tau_N = \frac{G_{NW}}{C_N}$) is much faster than the rate of transfer from the water to the surroundings ($\tau_W = \frac{G_{WB}}{C_W}$). Therefore, the kinetics of water temperature is solely governed by $\tau_W$. Equation 5.1 then becomes:

$$\frac{dT_W}{dt} = \frac{I - G_{WB}(T_W - T_B)}{C_W} \tag{5.3}$$

which can be easily solved to give,

$$\Delta T_W = \frac{I}{G_{WB}}(1 - exp(-\frac{G_{WB}}{C_W}t)) \tag{5.4}$$

Therefore, the temperature profile of the water is expected to look like a mono-exponential rise. In fact, for all values of $g^*$ such that $\tau_N \ll \tau_W$, the temperature profile is governed by the single rate constant of water. If we define R as the ratio between the two rate constants, then, we expect a mono-exponential rise as long as:

$$R = \frac{\tau_N}{\tau_W} = \frac{\frac{G_{NW}}{C_N}}{\frac{G_{WB}}{C_W}} = \frac{\frac{g^* G_{expected}}{C_N}}{\frac{G_{WB}}{C_W}} \ll 1 \tag{5.5}$$

When $g^*$ value is such that R $\approx$ 1, the solution to the ODEs defined in Eq 5.1 and 5.1 is governed by both the rate constants, which are now comparable to one another. For the values of Gs and Cs used in this study (Table 5 in Figure 5.2),

this condition occurs for $g^* \approx 10^{-13}$. The solution in this case, as shown in Figure 5.3, has a characteristic delay at the start, indicating a double-exponential shape. Alternately, the second derivative of the temperature profile for cases where $R > 1$ (which corresponds to $g^* < 10^{-12}$ in the current study) is always strictly negative, indicating a concave down curve representative of a single exponential profile. For $g^*$ values close to $10^{-13}$, the second derivative is biphasic (having both positive and negative values) with positive values indicating a concave up profile at the start - representative of the characteristic delay in a double exponential curve. The time at which the value of the second derivative goes from positive to negative (i.e., equals zero) is called the inflection point. As $g^*$ value decreases, the time at which inflection occurs increases, due to the slower rate at which nanoparticle dissipates to the water. The temperature profiles and their second derivatives for a range of g* values are shown in Fig 5.3.

## 5.2 Predictions from the model for nanoparticle solution heating

In order to test this hypothesis, we measure the temperature profile from different solutions having different values of R. Since the value of $g^*$ is fixed and is an intrinsic property of the nanoparticle-water interface, we can change the value of R by changing the value of $C_W$ keeping the number of nanoparticles in the solution (and therefore the value of $C_N$) fixed. For our study, this fixed amount of nanoparticles is 0.5 mg. Changing the volume of water in which the fixed number of nanoparticles is dissolved changes the value of $C_W$. The different volumes of solution also have different value of $G_{WB}$, which can be easily found by measuring the heat dissipation rate from that

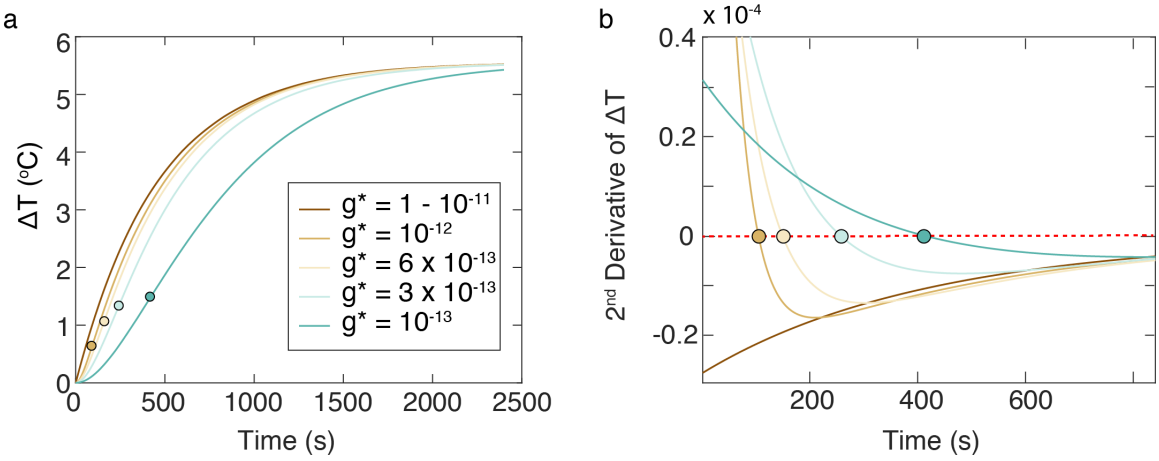


Figure 5.3 : (a) When $g^*$ is $< 10^{-12}$, the water temperature profile is governed solely by $G_{WB}$ and $C_W$, giving a single-exponential rise. As $g^*$ approaches $10^{-13}$, the kinetics of water temperature is governed by both $G_{WB}/C_W$ as well as $G_{NW}/C_N$ giving rise to a characteristic delay in temperature rise at the start of magnetic heating. (b) The second derivative of the temperature profile for $g^* < 10^{-12}$ is always strictly negative, indicating a concave down curve representative of a single exponential profile. For $g^*$ values close to $10^{-13}$, the second derivative is biphasic (having both positive and negative values) with positive values indicating a concave up profile at the start - representative of the characteristic delay in a double exponential curve. As $g^*$ value decreases, the time at which inflection occurs increases, due to the slower rate at which nanoparticle dissipates to the water. Circles show inflection points.

volume of heated water and multiplying by its heat capacity. Assuming a fixed value of power dissipated ($I = 100$ W/g), the temperature profiles for the different volumes of nanoparticle solution as modeled using Eq 5.1 and 5.1 for $g^* = 1$ and $g^* = 10^{-13}$ are shown in Figure 5.4. If $g^*$ =1, the value of $R$ is always much greater than 1 for any value of $C_W$ and therefore, the temperature profile is always expected to look mono-exponential with a negative derivative and therefore has no inflection points. If $g^* \approx 10^{-13}$, then increasing value of $C_W$ bring $R$ closer to 1 and changes the shape of the temperature curve from mono-exponential to double-exponential. Equivalently, the second derivative goes from being strictly negative to biphasic. Additionally, the delay at the start of the curve (or equivalently, the time at which inflection occurs) increases as $C_W$ increases. This concept is illustrated in Figure 5.4.

## 5.3 Future experiments

These predictions can be verified experimentally by measuring the temperature profiles under the application of magnetic field of four different volumes of solution (say,50 $\mu$l, 250 $\mu$l, 500 $\mu$l and 1000 $\mu$l), each containing fixed amount (say, 0.5 mg) of iron oxide nanoparticles. To measure the nanoparticle heating, a microtube consisting of the solution would be placed in an insulating styrofoam enclosure similar to the one shown in Figure 4.4. A fiber optic thermometer is inserted in the tube to measure the temperature. The styrofoam enclosure with the tube and thermometer are placed within the coils of an RF mangetic field generator. After ensuring that the measurements are not affected by the coil heating (by using larger coils and thick insulation), temperature is measured from the solution in the presence of alternating magnetic field. If the shape of the profile changes with changing $C_W$, then it provides evidence for a lowered thermal conductance at the interface of nanoparticle and water.

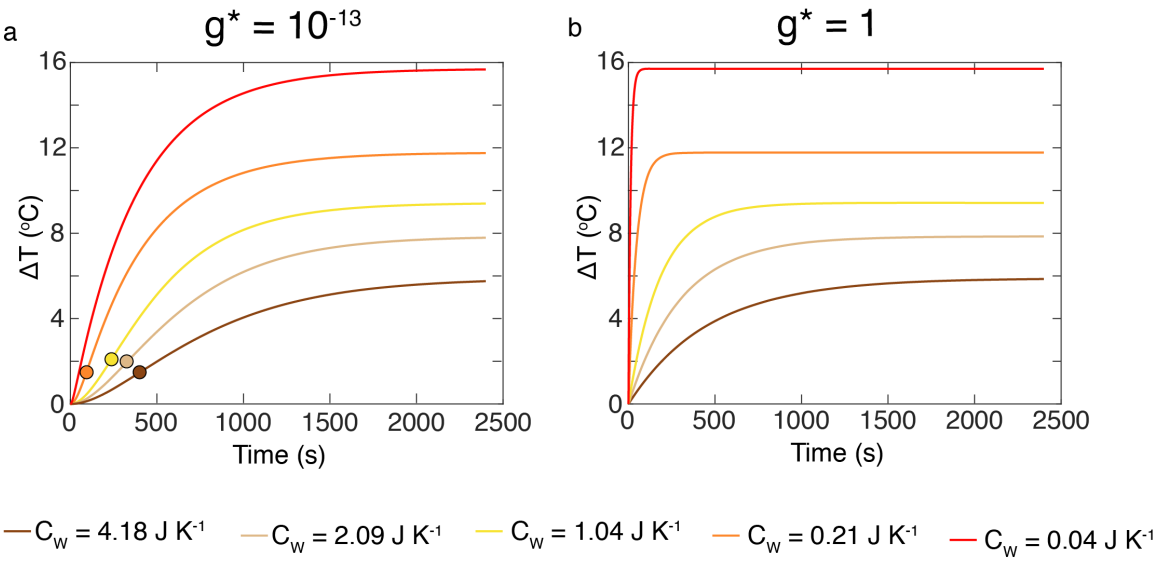


Figure 5.4 : Comparing the effect of changing $C_W$ (i.e., the volume of water) on the shape of temperature curve for the case of (a) $g^* = 10^{-13}$ and (b) $g^* = 1$ in a solution containing fixed amount of nanoparticles. When $g^* = 10^{-13}$, the water temperature profile changes shape with changing $C_W$ as the corresponding value of $R$ varies close to 1. The second derivative goes from biphasic, with inflection points (shown by circles) occuring at a faster times as $C_W$ decreases until the derivative becomes negative. (b) At $g^* = 1$, the value of $R$ is always much greater than 1 for any value of $C_W$ and therefore, the temperature profile is always expected to look mono-exponential with a strictly negative derivative for all values of $C_W$ (no inflection points).

# Chapter 6

# Discussion and Future Work

## 6.1 Designing better magnetogenetic tools based on the Magnetocaloric mechanism

I have proposed a thermally-mediated mechanism for explaining the magnetic sensitivity of magnetogenetic protein consisting of TRPV4-ferritin protein chimera called *Magneto2.0* based on Magnetocaloric heating of ferritin. Using this new rationale, we designed and built a new magnetogenetic protein, *MagM8* by fusing cold-gated channel TRPM8 and ferritin. I further investigated the role of anomalously high values of nanoscale thermal conductance in gating magnetogenetic ion channels. Using a novel approach based on silicon photonic thermometry, we measure nanoscale temperature gradients and thermal conductances to be 13 orders of magnitude greater than the values expected from classical heat transfer laws.

It is evident from the experimental results that the responses of *Magneto2.0* and *MagM8* to magnetic fields are (1) not strong and (2) not fast (compared to optogenetics that has millisecond temporal resolution [12]). Our mechanism suggests that increased number of magnetizations will improve the response from the channels. However, for a given total stimulation time ($\approx$ 300 s in our experiments), the final value of channel response - characterized by the number of additional channel openings ($m$) - does not depend on the frequency of applied field for frequencies greater than the heat dissipation rate from the ferritin. Because of the slow heat dissipation

rate predicted by g* ($\approx 0.1$ s$^{-1}$), stimulation at a higher frequency would result in magnetocaloric cooling upon demagnetization before the ferritin has released all of the generated heat. So the $m$ per cycle is lower. Even though a high frequency would result in a lower increase in $m$ per cycle, it also means more cycles of magnetization for a given total stimulation time. The two effects complement each other to maintain a constant value of $m$ for frequencies greater than the heat dissipation rate. Figure 6.1 shows the total $m$ at the end of 300 s of magnetic stimulation as a function of the frequency of applied field. This calculation assumes $g^* = 2 \times 10^{-12}$ (corresponding to a heat dissipation rate of 0.1 s$^{-1}$) and $c^* = 10^{-5}$ just as in Figure 2.7 in Section 2.5. The value of $m$ remains constant for frequencies $\geq 0.1$ Hz. In our experiments (Section 3.2) we use 0.08 Hz and therefore, increasing the frequency of stimulation will not result in higher response. The value of $g^* = 10^{-12}$ is obtained from the heat dissipation time of $\approx 10$ s as measured by Munshi et al. from heated nanoparticles attached to the surface of cells [16]. While this is our best estimate for the value of $g^*$ for nanoparticles at the cell membrane, it is likely that the value of $g^*$ is greater than $10^{-12}$ (i.e., faster heat dissipation) in which case, increasing frequency will increase $m$. However, without knowing the exact value of $g^*$, it is difficult to predict whether increasing frequency would result in greater response.

Our understanding of the mechanism helps in making these proteins more sensitive and robust. To achieve this, the first and the most obvious requirements are for the magnetic particle to have a higher susceptibility and to use higher magnetic fields. Apart from these, our understanding of the mechanism leads to the following ways in which a better magnetogenetic tool could be designed:

1. It is important to use a temperature-sensitive channel. For example, ferritin attached to a purely mechanosensitive channel, such as Piezo1 will not have any

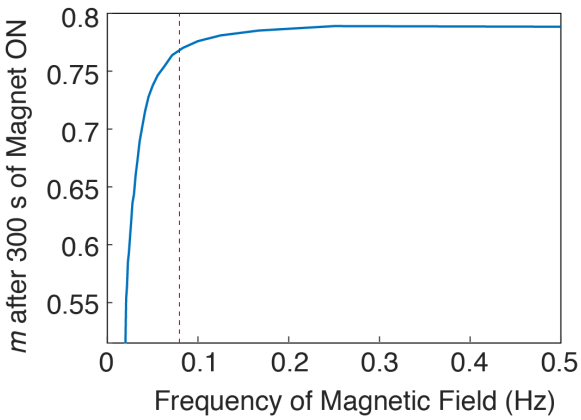


Figure 6.1 : Frequency dependence of channel response (characterized by the number of additional channel openings, $m$ due to Magnetocaloric effect: Because of the slow heat dissipation rate predicted by g* ($\approx 0.1$ s$^{-1}$), stimulation at a higher frequency would result in magnetocaloric cooling upon demagnetization before the ferritin has released all of the generated heat. So the $m$ per cycle is lower. Even though a high frequency would result in a lower increase in $m$ per cycle, it also means more cycles of magnetization for a given total stimulation time. The two effects complement each other to maintain a constant value of $m$ for frequencies greater than the heat dissipation rate.

appreciable effect on channel gating.

2. A magnetocaloric mechanism implies that it is the process of magnetization (and not a steady field) that leads to generation of heat to gate the channel. Therefore, a repeated stimulus gives better responses.

3. The mechanism suggests using channels that have a steeper temperature dependence. In terms of the thermodynamic parameters discussed in Section 2.4, this would mean choosing a channel with higher values of $\Delta H_{gating}$ and $\Delta S_{gating}$.

4. The mechanism suggests that, to maximize the effect of the heat towards channel gating, it is important to have ferritin close to a temperature sensitive domain.

## 6.2 Nanoscale thermal conductance and heat absorption

Our calculations and experimental results support the magnetocaloric hypothesis for magnetic activation of TRPV4-ferritin and TRPM8-ferritin fusion proteins, but more work is needed to confirm this activation mechanism. In particular, our model relies on decreased thermal conductance ($g^*$) and local heat absorption ($c^*$) due to the nanoscale separation distance between the ferritin nanoparticle and channel protein. We measured a thermal conductance 13 orders of magnitude less than expected from classical laws in the vicinity of synthetic nanoparticles. These experiments need to be further backed up with rigorous control experiments as suggested in Sections 4.5 and 5.3. Besides the experimental evidence supporting a thermal resistance correction factor of eleven to thirteen orders of magnitude, large correction factors are not unprecedented for nanoscale distances. For example, the Raman signal from molecules within a few nanometers of a metal surface can be increased by 7-14 orders of magnitude [80]. Thus, nanoscale separation distances can significantly modify physical processes. While the experimental evidence supports anomalous nanoscale heat transfer phenomena near synthetic magnetic nanoparticles, similar experiments with ferritin along with improved theoretical understanding of heat transport at the nanoscale are still important goals to achieve. However, the biggest challenge to performing similar nanoscale thermal measurements from ferritin is the low heating efficiency of ferritin.

## 6.3 Magnetocaloric effect in high frequency magnetic fields

The magnetocaloric hypothesis predicts that magnetic particles heat during magnetization and cool during demagnetization. In the case of a slowly varying field, a nonlinear response of the cell and/or channel is required to produce a net physiologi-

cal change over time. For example, during cycles of magnetization, the calcium influx produced by heating TRPV4 must be larger than the net calcium efflux produced during cycles of demagnetization that cool TRPV4. We expect that three mechanisms might contribute to such asymmetric responses: i) secondary messengers and/or calcium itself can trigger the release of calcium from intracellular calcium stores [81], [82], [83], [84] ii) the local depolarization can trigger voltage-gated ion channels in neurons, and to a lesser extent, in non-excitatory cells [85] , iii) TRPV4 activity can be amplified by positive feedback, through phosphorylation of key residues and calcium-dependent membrane recruitment of TRPV4 (or in this case *Magneto2.0*) [86], [87], [88]. Any of these mechanisms could give rise to a net calcium influx over time, instead of the oscillating levels that might result if the calcium levels precisely followed the cycles of magnetocaloric heating and cooling. Similarly, in the case of *MagM8*, the calcium influx produced by cooling TRPM8 during demagnetization must be larger than the net calcium efflux produced during cycles of magnetization that heat TRPM8. In the case of rapidly switching fields (e.g. hundreds of kHz), the field switches much faster than these nonlinear effects. In that case, the channel response is determined by the average channel temperature per cycle which decays based on the thermal relaxation rate. This relaxation rate depends on the value of $g^*$. Thus, we expect the application of RF magnetic field would raise the temperature surrounding the nanoparticle for a brief period of time before it decays back to the bath temperature. Therefore, RF magnetic field would cause magnetocaloric heating that would dissipate within seconds (Figure 6.2). Note that our predictions suggest that the magnitude of response is independent of the duration of the RF magnetic stimulus. The data in Stanley et al. (discussed in Section 1.2) shows that the physiological response increases for longer stimulus periods suggesting the magnetocaloric

effect may not explain these results. The giant thermal resistance values ($1/g^*$) required for our theory (and supported by our experiments as well as several studies in the literature [14], [27], [28], [16], [29], [30], [31]) may also have implications for high-frequency magnetic stimulation of ferritin-TRP assemblies [18]. Although the specific absorption rate of ferritin in alternating magnetic field may be too small to produce significant temperature changes in a volume of fluid, the lowered thermal conductance may produce local temperature changes sufficient to gate nearby thermoreceptors, which is consistent with recent reports of ferritin-TRP fusion proteins that respond to high-frequency AMFs ([18]).

## 6.4 Optimization and future work

Even though magnetic stimulation of *Magneto2.0* and *MagM8* produces a weak population response which can be measured by the averaging calcium level increases over long periods of time, the response observed in our experiments appears to be more similar to neuromodulation where the application of a magnetic field would bias neural activity but not necessarily produce specifically timed action potentials on demand. This effect is qualitatively different from optogenetic stimulation that produces precisely-timed action potentials in each cell expressing the transgene. However, considering magnetic fields do not scatter like optical stimuli, this neuromodulation may prove particularly useful to uniformly modulate diffuse cell populations throughout the brain. As a result, magnetogenetics might prove to be most useful as a minimally invasive method to shift the excitability of select neuronal populations distributed throughout the brain.

Even then, more sensitive magnetogenetic channels will improve our ability to understand the activation mechanism by enabling more quantitative experiments. For

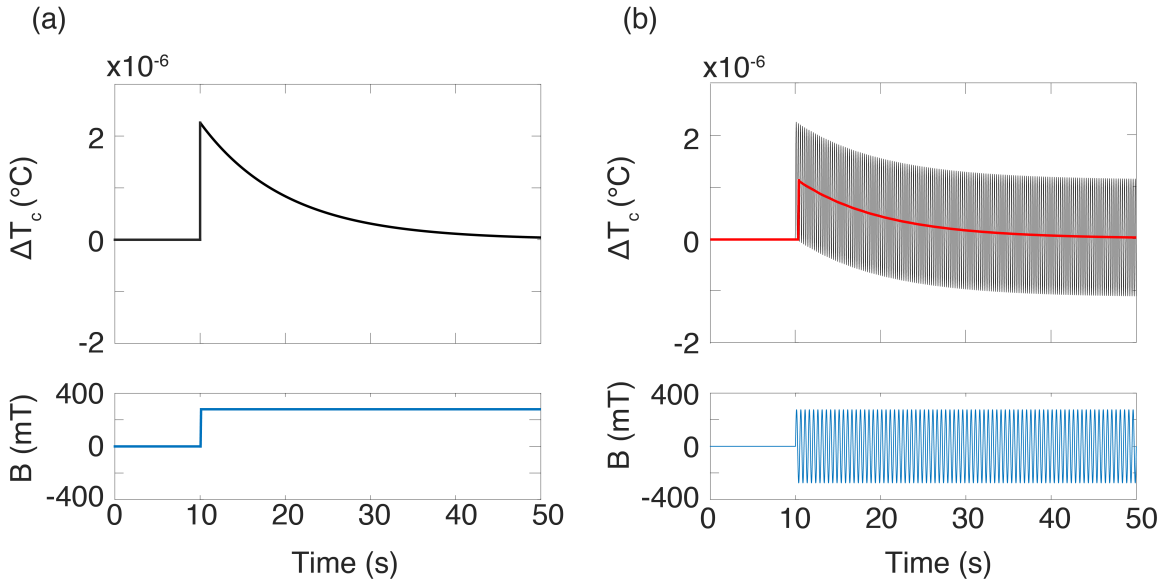


Figure 6.2 : (a) Change in channel temperature ($\Delta T_c$) (top) due to magnetocaloric heating from a single magnetic stimulus (bottom). The temperature is raised by $\frac{Q_f}{C}$ and decays back to initial temperature at a rate determined by $g^*$ (Eq S11 and Table 1). (b) Change in channel temperature (top) due to magnetocaloric effect in an RF magnetic field (bottom) modeled using Eq S7. The channel heats during magnetization and cools during demagnetization. The average temperature per cycle (red curve) decays at the same rate determined by $g^*$. Note also that the average rise in temperature is half of that in the case of a single magnetization. For clarity, we plot simulation with a 2 Hz magnetic field. We calculate that RF fields will generate a nearly identical temperature profile.

example, single channel electrophysiology would provide a more detailed description of channel activity, but is prohibitively laborious if only a small percentage of channels are activated by the magnetic stimuli. Additionally, stronger calcium or voltage responses would allow researchers to study quantitative differences between stimulation protocols that would help uncover the underlying activation mechanism. In addition, better biophysical understanding of the thermal gating mechanisms of TRP channels will further improve our estimates of gating by the magnetocaloric effect. Another factor to consider in our model is the heat transfer through the lipid bilayer.

Ferritin is weakly magnetic and improving its magnetic susceptibility is one of the most important steps towards improving magnetic sensitivity of Magneto-like proteins. This involves genetic engineering of ferritin to enhance its iron loading. Matsumoto et al. [89] used high throughput screening to select variants of ferritin having enhanced iron loading. A similar approach to genetically engineer a channel with enhanced magnetic sensitivity is a goal for long-term future.

A different system to test the magnetocaloric theory is the temperature-dependent looping and unlooping of a DNA hairpin structure. The kinetics of this reaction is similar to the two-state system model for channel that was discussed in Section 2.4. A DNA hairpin structure (also known as a molecular beacon) fluctuates between open and closed state with charateristic rates $\alpha$, $\beta$. If a fluorophore is attached to one end and a quencher on the other end, then in the open state, the beacon fluoresces. In the closed state, the fluophore and quencher come together and form a covalent link and hence fluorescence is quenched. These DNA binding-unbinding events are studied widely using Fluorescence Resonance Energy Transfer (FRET) [90] and Fluorescence Correlation Spectroscopy (FCS) [91]. This system also offers a more direct way of studying the effect of the heat down at the level of the molecule, which is very difficult in the case of a channel. Firstly, to observe channel kinetics, it needs to be expressed in a cell. Secondly, calcium imaging is not very quantitative and hence an accurate measure of the response is not possible to make. An alternative to this is to use patch clamp electrophysiology, which is time consuming, especially if we want to study single channel kinetics. DNA, on the other hand, can be studied in a solution using conventional fluorescence techniques.

The most exciting outcome of the magnetocaloric hypothesis is a rational approach to improve the magnetic response of magnetogenetic proteins. For example,

we predict that improving the heat transfer efficiency or the thermal sensitivity of *Magneto2.0* will improve the magnetic sensitivity. Thus, the magnetocaloric hypothesis provides both a potential explanation for the recently reported magnetogenetic proteins and an approach for developing new, more sensitive constructs that respond to low frequency magnetic stimuli.

# Bibliography

[1] M. A. Wheeler, C. J. Smith, M. Ottolini, B. S. Barker, A. M. Purohit, R. M. Grippo, R. P. Gaykema, A. J. Spano, M. P. Beenhakker, S. Kucenas, M. K. Patel, C. D. Deppmann, and A. D. Güler, "Genetically targeted magnetic control of the nervous system.," *Nature neuroscience*, vol. 19, pp. 756–61, may 2016.

[2] J. Vriens, H. Watanabe, A. Janssens, G. Droogmans, T. Voets, and B. Nilius, "Cell swelling, heat, and chemical agonists use distinct pathways for the activation of the cation channel TRPV4.," *Proceedings of the National Academy of Sciences of the United States of America*, vol. 101, no. 1, pp. 396–401, 2004.

[3] G. Marmont, "Studies on the axon membrane. I. A new method," *Journal of Cellular and Comparative Physiology*, vol. 34, pp. 351–382, dec 1949.

[4] A. L. Hodgkin and A. F. Huxley, "A quantitative description of membrane current and its application to conduction and excitation in nerve," *Bulletin of Mathematical Biology*, vol. 52, no. 1-2, pp. 25–71, 1990.

[5] E. Neher and B. Sakmann, "Single-channel currents recorded from membrane of denervated frog muscle fibres.," *Nature*, vol. 260, no. 5554, pp. 799–802, 1976.

[6] M. E. J. Obien, K. Deligkaris, T. Bullmann, D. J. Bakkum, and U. Frey, "Revealing neuronal function through microelectrode array recordings," *Frontiers in Neuroscience*, vol. 9, no. JAN, p. 423, 2015.

[7] S. Miocinovic, S. Somayajula, S. Chitnis, and J. L. Vitek, "History, applications, and mechanisms of deep brain stimulation.," *JAMA neurology*, vol. 70, no. 2, pp. 163–71, 2013.

[8] W. Grill, "Signal considerations for chronically implanted electrodes for brain interfacing," *Indwelling Neural Implants: Strategies for Contending . . .*, pp. 42–61, 2008.

[9] R. H. W. Funk, T. Monsees, and N. Ozzkucur, "Electromagnetic effects - From cell biology to medicine," *Progress in Histochemistry and Cytochemistry*, vol. 43, no. 4, pp. 177–264, 2009.

[10] V. Walsh and A. Cowey, "Transcranial magnetic stimulation and cognitive neuroscience," *Nature Reviews Neuroscience*, vol. 1, no. 1, pp. 73–9, 2000.

[11] G. Nagel, T. Szellas, W. Huhn, S. Kateriya, N. Adeishvili, P. Berthold, D. Ollig, P. Hegemann, and E. Bamberg, "Channelrhodopsin-2, a directly light-gated cation-selective membrane channel.," *Proceedings of the National Academy of Sciences of the United States of America*, vol. 100, no. 24, pp. 13940–5, 2003.

[12] E. S. Boyden, F. Zhang, E. Bamberg, G. Nagel, and K. Deisseroth, "Millisecond-timescale, genetically targeted optical control of neural activity.," *Nature neuroscience*, vol. 8, no. 9, pp. 1263–8, 2005.

[13] X. Han, B. Y. Chow, H. Zhou, N. C. Klapoetke, A. Chuong, R. Rajimehr, A. Yang, M. V. Baratta, J. Winkle, R. Desimone, and E. S. Boyden, "A high-light sensitivity optical neural silencer: development and application to optogenetic control of non-human primate cortex.," *Frontiers in systems neuroscience*, vol. 5, no. April, p. 18, 2011.

[14] H. Huang, S. Delikanli, H. Zeng, D. M. Ferkey, and A. Pralle, "Remote control of ion channels and neurons through magnetic-field heating of nanoparticles.," *Nature nanotechnology*, vol. 5, no. 8, pp. 602–606, 2010.

[15] R. Chen, G. Romero, M. G. Christiansen, A. Mohr, and P. Anikeeva, "Wireless magnetothermal deep brain stimulation.," *Science (New York, N.Y.)*, vol. 347, pp. 1477–80, mar 2015.

[16] R. Munshi, S. M. Qadri, Q. Zhang, I. Castellanos Rubio, P. del Pino, and A. Pralle, "Magneto-thermal genetic deep brain stimulation of motor behaviors in awake, freely moving mice," *eLife*, vol. 6, aug 2017.

[17] S. A. Stanley, J. E. Gagner, S. Damanpour, M. Yoshida, J. S. Dordick, and J. M. Friedman, "Radio-wave heating of iron oxide nanoparticles can regulate plasma glucose in mice.," *Science (New York, N.Y.)*, vol. 336, pp. 604–8, may 2012.

[18] S. a. Stanley, J. Sauer, R. S. Kane, J. S. Dordick, and J. M. Friedman, "Remote regulation of glucose homeostasis in mice using genetically encoded nanoparticles," *Nature Medicine*, vol. 21, no. 1, pp. 92–98, 2014.

[19] E. Fantechi, C. Innocenti, M. Zanardelli, M. Fittipaldi, E. Falvo, M. Carbo, V. Shullani, L. Di Cesare Mannelli, C. Ghelardini, A. M. Ferretti, A. Ponti, C. Sangregorio, and P. Ceci, "A smart platform for hyperthermia application in cancer treatment: cobalt-doped ferrite nanoparticles mineralized in human ferritin cages.," *ACS nano*, vol. 8, pp. 4705–19, may 2014.

[20] E. C. Theil, "Ferritin: structure, gene regulation, and cellular function in animals, plants, and microorganisms.," *Annual review of biochemistry*, vol. 56, no. 1, pp. 289–315, 1987.

[21] M. Meister, "Physical limits to magnetogenetics," *eLife*, vol. 5, no. AUGUST, pp. 1–14, 2016.

[22] J. H. Lee, J. W. Kim, M. Levy, A. Kao, S. H. Noh, D. Bozovic, and J. Cheon, "Magnetic nanoparticles for ultrafast mechanical control of inner ear hair cells," *ACS Nano*, vol. 8, no. 7, pp. 6590–6598, 2014.

[23] S. Hughes, S. McBain, J. Dobson, and A. J. El Haj, "Selective activation of mechanosensitive ion channels using magnetic particles.," *Journal of the Royal Society, Interface / the Royal Society*, vol. 5, no. 25, pp. 855–863, 2008.

[24] G. Duret, S. Polali, E. D. Anderson, A. M. Bell, C. N. Tzouanas, B. W. Avants, and J. T. Robinson, "Magnetic Entropy as a Proposed Gating Mechanism for Magnetogenetic Ion Channels," *Biophysj*, vol. 116, no. 3, pp. 454–468, 2019.

[25] V. Franco, J. Blázquez, B. Ingale, and a. Conde, "The Magnetocaloric Effect and Magnetic Refrigeration Near Room Temperature: Materials and Models," *Annual Review of Materials Research*, vol. 42, no. 1, pp. 305–342, 2012.

[26] P. Keblinski, D. G. Cahill, A. Bodapati, C. R. Sullivan, and T. A. Taton, "Limits of localized heating by electromagnetically excited nanoparticles," *Journal of Applied Physics*, vol. 100, no. 5, 2006.

[27] R. Piñol, C. D. S. Brites, R. Bustamante, A. Martínez, N. J. O. Silva, J. L. Murillo, R. Cases, J. Carrey, C. Estepa, C. Sosa, F. Palacio, L. D. Carlos, and A. Millán, "Joining time-resolved thermometry and magnetic-induced heating in a single nanoparticle unveils intriguing thermal properties.," *ACS nano*, vol. 9, pp. 3134–42, mar 2015.

[28] J. Dong and J. I. Zink, "Taking the temperature of the interiors of magnetically heated nanoparticles.," *ACS nano*, vol. 8, pp. 5199–207, may 2014.

[29] A. Riedinger, P. Guardia, A. Curcio, M. A. Garcia, R. Cingolani, L. Manna, and T. Pellegrino, "Subnanometer local temperature probing and remotely controlled drug release based on azo-functionalized iron oxide nanoparticles.," *Nano letters*, vol. 13, pp. 2399–406, jun 2013.

[30] J. T. Dias, M. Moros, P. Del Pino, S. Rivera, V. Grazú, and J. M. De La Fuente, "DNA as a molecular local thermal probe for the analysis of magnetic hyperthermia," *Angewandte Chemie - International Edition*, vol. 52, no. 44, pp. 11526–11529, 2013.

[31] L. Polo-Corrales and C. Rinaldi, "Monitoring iron oxide nanoparticle surface temperature in an alternating magnetic field using thermoresponsive fluorescent polymers," *Journal of Applied Physics*, vol. 111, no. 7, 2012.

[32] M. Creixell, A. C. Bohórquez, M. Torres-Lugo, and C. Rinaldi, "EGFR-targeted magnetic nanoparticle heaters kill cancer cells without a perceptible temperature rise," *ACS Nano*, vol. 5, no. 9, pp. 7124–7129, 2011.

[33] G. Romero, M. G. Christiansen, L. Stocche Barbosa, F. Garcia, and P. Anikeeva, "Localized Excitation of Neural Activity via Rapid Magnetothermal Drug Release," *Advanced Functional Materials*, vol. 26, no. 35, pp. 6471–6478, 2016.

[34] S. H. Kilcoyne and R. Cywinski, "Ferritin: a model superparamagnet," *Journal of Magnetism and Magnetic Materials*, vol. 140-144, no. PART 2, pp. 1466–1467, 1995.

[35] S. a. Makhlouf, F. T. Parker, and a. E. Berkowitz, "Magnetic hysteresis anomalies in ferritin," *Physical Review B*, vol. 55, no. 22, pp. R14717–R14720, 1997.

[36] G. C. Papaefthymiou, "The Mössbauer and magnetic properties of ferritin cores," *Biochimica et Biophysica Acta - General Subjects*, vol. 1800, no. 8, pp. 886–897, 2010.

[37] Q. a. Pankhurst, J. Connolly, S. K. Jones, and J. Dobson, "Applications of magnetic nanoparticles in biomedicine," *Journal of Physics D: Applied Physics*, vol. 36, no. 13, pp. R167–R181, 2003.

[38] F. Brem, G. Stamm, and A. M. Hirt, "Modeling the magnetic behavior of horse spleen ferritin with a two-phase core structure," *Journal of Applied Physics*, vol. 99, no. 12, 2006.

[39] A. Lervik, F. Bresme, S. Kjelstrup, D. Bedeaux, and J. Miguel Rubi, "Heat transfer in proteinwater interfaces," *Physical Chemistry Chemical Physics*, vol. 12, no. 7, p. 1610, 2010.

[40] S. H. Banyard, D. K. Stammers, and P. M. Harrison, "Electron density map of apoferritin at 2.8-Å resolution," *Nature*, vol. 271, pp. 282–284, 1978.

[41] H. Shigematsu, T. Sokabe, R. Danev, M. Tominaga, and K. Nagayama, "A 3.5-nm structure of rat TRPV4 cation channel revealed by zernike phase-contrast cryoelectron microscopy," *Journal of Biological Chemistry*, vol. 285, no. 15, pp. 11210–11218, 2010.

[42] M. Chase, *NIST-JANAF Thermochemical Tables 2 Volume-Set (Journal of Physical and Chemical Reference Data Monographs).* American Institute of Physics, fourth edi ed., 1998.

[43] J. Gomez, V. J. Hilser, D. Xie, and E. Freire, "The heat capacity of proteins," *Proteins: Structure, Function, and Bioinformatics*, vol. 22, no. 4, pp. 404–412, 1995.

[44] Y. Rabin, "Is intracellular hyperthermia superior to extracellular hyperthermia in the thermal sense?," *International journal of hyperthermia : the official journal of European Society for Hyperthermic Oncology, North American Hyperthermia Group*, vol. 18, no. 3, pp. 194–202, 2002.

[45] G. Chen, "Nonlocal and Nonequilibrium Heat Conduction in the Vicinity of Nanoparticles," *Journal of Heat Transfer*, vol. 118, no. 3, p. 539, 1996.

[46] A. E. Deatsch and B. A. Evans, "Heating efficiency in magnetic nanoparticle hyperthermia," *Journal of Magnetism and Magnetic Materials*, vol. 354, no. March, pp. 163–172, 2014.

[47] S. Dutz and R. Hergt, "Magnetic particle hyperthermiaa promising tumour therapy?," *Nanotechnology*, vol. 25, no. 45, p. 452001, 2014.

[48] M. Capelli, P. Reineck, D. W. Lau, A. Orth, J. Jeske, M. W. Doherty, T. Ohshima, A. D. Greentree, and B. C. Gibson, "Magnetic field-induced enhancement of the nitrogen-vacancy fluorescence quantum yield," *Nanoscale*, vol. 9, no. 27, pp. 9299–9304, 2017.

[49] K. Okabe, N. Inada, C. Gota, Y. Harada, T. Funatsu, and S. Uchiyama, "Intracellular temperature mapping with a fluorescent polymeric thermometer and fluorescence lifetime imaging microscopy.," *Nature communications*, vol. 3, p. 705, feb 2012.

[50] J. Teng, S. H. Loukin, A. Anishkin, and C. Kung, "L596-W733 bond between the start of the S4-S5 linker and the TRP box stabilizes the closed state of TRPV4 channel.," *Proceedings of the National Academy of Sciences of the United States of America*, vol. 112, pp. 3386–91, mar 2015.

[51] Z. Deng, N. Paknejad, G. Maksaev, M. Sala-Rabanal, C. G. Nichols, R. K. Hite, and P. Yuan, "Cryo-EM and X-ray structures of TRPV4 reveal insight into ion permeation and gating mechanisms," *Nature Structural and Molecular Biology*, vol. 25, pp. 252–260, 2018.

[52] T. Voets, G. Droogmans, U. Wissenbach, A. Janssens, V. Flockerzi, and B. Nilius, "The principle of temperature-dependent gating in cold- and heat-sensitive TRP channels.," *Nature*, vol. 430, no. 7001, pp. 748–754, 2004.

[53] J. R. Naranjo and B. Mellström, "Ca2+-dependent transcriptional control of Ca2+ homeostasis," *Journal of Biological Chemistry*, vol. 287, no. 38, pp. 31674–31680, 2012.

[54] M. Shamir, Y. Bar-On, R. Phillips, and R. Milo, "SnapShot: Timescales in Cell Biology," *Cell*, vol. 164, no. 6, pp. 1302–1302.e1, 2016.

[55] T. Wang, H. Xu, J. Oberwinkler, Y. Gu, R. C. Hardie, and C. Montell, "Light activation, adaptation, and cell survival functions of the Na +/Ca2+ exchanger CalX," *Neuron*, vol. 45, no. 3, pp. 367–378, 2005.

[56] H. Watanabe, J. Vriens, S. H. Suh, C. D. Benham, G. Droogmans, and B. Nilius, "Heat-evoked activation of TRPV4 channels in a HEK293 cell expression system and in native mouse aorta endothelial cells," *Journal of Biological Chemistry*, vol. 277, no. 49, pp. 47044–47051, 2002.

[57] T. Voets, G. Owsianik, A. Janssens, K. Talavera, and B. Nilius, "TRPM8 voltage sensor mutants reveal a mechanism for integrating thermal and chemical stimuli," *Nature Chemical Biology*, vol. 3, pp. 174–182, mar 2007.

[58] B. V. Zemelman, N. Nesnas, G. A. Lee, and G. Miesenbock, "Photochemical gating of heterologous ion channels: Remote control over genetically designated populations of neurons," *Proceedings of the National Academy of Sciences*, vol. 100, no. 3, pp. 1352–1357, 2003.

[59] B. Hille, *Ion Channels of Excitable Membranes*. Sinauer Associates, third edit ed., 2001.

[60] B. E. McKay and R. W. Turner, "Physiological and morphological development of the rat cerebellar Purkinje cell," *The Journal of Physiology*, vol. 567, pp. 829–850, sep 2005.

[61] A. Szücs, F. Berton, P. P. Sanna, and W. Francesconi, "Excitability of jcBNST Neurons Is Reduced in Alcohol-Dependent Animals during Protracted Alcohol Withdrawal," *PLoS ONE*, vol. 7, p. e42313, aug 2012.

[62] N. Z. Gungor, R. Yamamoto, and D. Pare, "Optogenetic study of the projections from the bed nucleus of the stria terminalis to the central amygdala," *Journal of Neurophysiology*, vol. 114, pp. 2903–11, nov 2015.

[63] D. Brocker and W. Grill, "Principles of electrical stimulation of neural tissue," *Handbook of Clinical Neurology*, vol. 116, pp. 3–18, 2013.

[64] I. D. Johnson and M. T. Spence, *Molecular Probes Handbook: A Guide to Fluorescent Probes and Labeling Technologies*. Life Technologies Corporation, 2010.

[65] R. Fliegert, G. Glassmeier, F. Schmid, K. Cornils, S. Genisyuerek, A. Harneit, J. R. Schwarz, and A. H. Guse, "Modulation of Ca2+ entry and plasma membrane potential by human TRPM4b," *FEBS Journal*, vol. 274, no. 3, pp. 704–713, 2007.

[66] T. Voets, J. Prenen, J. Vriens, H. Watanabe, A. Janssens, U. Wissenbach, M. Bödding, G. Droogmans, and B. Nilius, "Molecular determinants of permeation through the cation channel TRPV4," *Journal of Biological Chemistry*, vol. 277, no. 37, pp. 33704–33710, 2002.

[67] Y. Mishin, "Thermodynamic theory of equilibrium fluctuations," *Annals of Physics*, vol. 363, pp. 48–97, 2015.

[68] L. Zubcevic, M. A. Herzik, B. C. Chung, Z. Liu, G. C. Lander, and S.-Y. Lee, "Cryo-electron microscopy structure of the TRPV2 ion channel," *Nature Structural & Molecular Biology*, vol. 23, no. 2, pp. 1–9, 2016.

[69] B. D. Matthews, C. K. Thodeti, J. D. Tytell, A. Mammoto, D. R. Overby, and D. E. Ingber, "Ultra-rapid activation of TRPV4 ion channels by mechanical forces applied to cell surface beta1 integrins," *Integr Biol (Camb)*, vol. 2, no. 9, pp. 435–442, 2010.

[70] C. S. S. R. Kumar and F. Mohammad, "Magnetic nanomaterials for hyperthermia-based therapy and controlled drug delivery," *Advanced Drug Delivery Reviews*, vol. 63, no. 9, pp. 789–808, 2011.

[71] K. Hayashi, K. Ono, H. Suzuki, M. Sawada, and M. Moriya, "Drug Release from Magnetic Nanoparticle / Organic Hybrid Based on Hyperthermic Effect," vol. 2, no. 7, pp. 1903–1911, 2010.

[72] E. Amstad, J. Kohlbrecher, M. Elisabeth, T. Schweizer, M. Textor, and E. Reimhult, "Triggered Release from Liposomes through Magnetic Actuation of Iron Oxide Nanoparticle Containing Membranes," *Nano Letters*, vol. 11, pp. 1664–1670, 2011.

[73] T. Kobayashi, "Cancer hyperthermia using magnetic nanoparticles," *Biotechnology Journal*, vol. 6, no. 11, pp. 1342–1347, 2011.

[74] M. Johannsen, U. Gneveckow, B. Thiesen, K. Taymoorian, C. Hee, N. Waldo, R. Scholz, A. Jordan, S. A. Loening, and P. Wust, "Thermotherapy of Prostate Cancer Using Magnetic Nanoparticles : Feasibility , Imaging , and Three-Dimensional Temperature Distribution," *European Urology*, vol. 52, pp. 1653–1662, 2007.

[75] G.-D. Kim, H.-S. Lee, C.-H. Park, S.-S. Lee, B. T. Lim, H. K. Bae, and W.-G. Lee, "Silicon photonic temperature sensor employing a ring resonator manufactured using a standard CMOS process.," *Optics express*, vol. 18, no. 21, pp. 22215–22221, 2010.

[76] W. Bogaerts, P. D. Heyn, T. V. Vaerenbergh, K. D. Vos, and S. Kumar, "Silicon microring resonators," *Laser & Photonics Reviews*, vol. 6, no. 1, pp. 47–73, 2012.

[77] W. T. B. D. Sousa, A. Polasek, R. Dias, C. F. T. Matt, and R. D. A. Jr, "Thermal electrical analogy for simulations of superconducting fault current limiters," *Cryogenics*, vol. 62, pp. 97–109, 2014.

[78] J. H. Lee, J. T. Jang, J. S. Choi, S. H. Moon, S. H. Noh, J. W. Kim, J. G. Kim, I. S. Kim, K. I. Park, and J. Cheon, "Exchange-coupled magnetic nanoparticles

for efficient heat induction," *Nature Nanotechnology*, vol. 6, no. 7, pp. 418–422, 2011.

[79] R. E. Rosensweig, "Heating magnetic fluid with alternating magnetic field," *Journal of Magnetism and Magnetic Materials*, vol. 252, no. 0, pp. 370–374, 2002.

[80] E. C. Le Ru, E. J. Blackie, M. Meyer, and P. G. Etchegoin, "Surface Enhanced Raman Scattering Enhancement Factors: A Comprehensive Study," *The Journal of Physical Chemistry C*, vol. 111, no. 37, pp. 13794–13803, 2007.

[81] A. P. Thomas, G. S. Bird, G. Hajnóczky, L. D. Robb-Gaspers, and J. W. Putney Jr, "Spatial and temporal aspects of cellular calcium signaling," *Faseb J*, vol. 10, no. 13, pp. 1505–1517, 1996.

[82] J. W. J. Putney, "Chapter 23. Calcium," in *Basic Neurochemistry, 6th edition*, 1999.

[83] J. M. Vicencio, C. Ibarra, M. Estrada, M. Chiong, D. Soto, V. Parra, G. Diaz-Araya, E. Jaimovich, and S. Lavandero, "Testosterone induces an intracellular calcium increase by a nongenomic mechanism in cultured rat cardiac myocytes.," *Endocrinology*, vol. 147, pp. 1386–95, mar 2006.

[84] K. M. Dunn, D. C. Hill-Eubanks, W. B. Liedtke, and M. T. Nelson, "TRPV4 channels stimulate Ca2+-induced Ca2+ release in astrocytic endfeet and amplify neurovascular coupling responses.," *Proceedings of the National Academy of Sciences of the United States of America*, vol. 110, pp. 6157–62, apr 2013.

[85] Y. A. Nikolaev, P. J. Dosen, D. R. Laver, D. F. van Helden, and O. P. Hamill, "Single mechanically-gated cation channel currents can trigger action potentials

in neocortical and hippocampal pyramidal neurons.," *Brain research*, vol. 1608, pp. 1–13, may 2015.

[86] H. Watanabe, J. Vriens, A. Janssens, R. Wondergem, G. Droogmans, and B. Nilius, "Modulation of TRPV4 gating by intra- and extracellular Ca2+," *Cell Calcium*, vol. 33, no. 5-6, pp. 489–495, 2003.

[87] Y. Fu, A. Subramanya, D. Rozansky, and D. M. Cohen, "WNK kinases influence TRPV4 channel function and localization," *American Journal of Physiology-Renal Physiology*, vol. 290, pp. F1305–F1314, jun 2006.

[88] S. Baratchi, J. G. Almazi, W. Darby, F. J. Tovar-Lopez, A. Mitchell, and P. McIntyre, "Shear stress mediates exocytosis of functional TRPV4 channels in endothelial cells," *Cellular and Molecular Life Sciences*, vol. 73, pp. 649–666, feb 2016.

[89] Y. Matsumoto, R. Chen, P. Anikeeva, and A. Jasanoff, "Engineering intracellular biomineralization and biosensing by a magnetic protein," *Nat Commun*, vol. 6, p. 8721, 2015.

[90] R. Tsukanov, T. E. Tomov, R. Masoud, H. Drory, N. Plavner, M. Liber, and E. Nir, "Detailed study of DNA hairpin dynamics using single-molecule fluorescence assisted by DNA origami," *Journal of Physical Chemistry B*, vol. 117, no. 40, pp. 11932–11942, 2013.

[91] G. Bonnet, O. Krichevsky, and A. Libchaber, "Kinetics of conformational fluctuations in DNA hairpin-loops," *PNAS*, vol. 95, no. July, pp. 8602–8606, 1998.